ANALYZING AND IMPROVING INITIAL DATA FOR BINARY BLACK HOLES

BY

JASON D. GRIGSBY

A Dissertation Submitted to the Graduate Faculty of

WAKE FOREST UNIVERSITY GRADUATE SCHOOL OF ARTS AND SCIENCES

in Partial Fulfillment of the Requirements

for the Degree of

DOCTOR OF PHILOSOPHY

Physics

August 2009

Winston-Salem, North Carolina

Approved By:

Greg Cook, Ph.D., Advisor _____

Examining Committee:

Jennifer Erway, Ph.D., Chairman _____

Paul Anderson, Ph.D. _____

Jed Macosko, Ph.D. _____

Eric Carlson, Ph.D. _____

This work is dedicated to

my parents, Linda and Robert,

and to my wife, Melanie,

for all the support they've given me.

Acknowledgments

My efforts for the last six years alone would have landed me no-where if it were not for the efforts and assistance of so many — my family, friends, fellow graduates students, the faculty at the department of physics and, in particular, my advisor, Gregory B. Cook. I am also indebted to the other members of my research advisory committee, Paul Anderson, Jed Macosko, Eric Calrson and Jennifer Erway. I should also mention Matthew Caudill and Harald P. Pfeiffer with whom I've worked. Harald P. Pfeiffer has been particularly helpful in my recent work. I would also like to thank Fred Salsbury for taking notice of me in the first place.

I am grateful for the support of Wake Forest University's Department of Physics. The spectral solver Eric was developed by Harald P. Pfeiffer and Gregory B. Cook. SpEC was develoepd by Mark A. Scheel, Harald P. Pfeiffer and Lawrence E. Kidder. The vast majority of the numerical data created for this work was created on the Wake Forest University Distributed Environment for Academic Computing cluster.

Contents

List of Figures

List of Tables

ABSTRACT

Grigsby, Jason D.

ANALYZING AND IMPROVING INITIAL DATA FOR BINARY BLACK HOLES

Dissertation under the direction of

Greg Cook, Ph.D., Associate Professor of Physics

Binary black holes are one of the most likely sources of gravitational radiation to be detected by projects such as LIGO and LISA. This radiation causes the binary to lose energy and angular momentum with the black holes adiabatically spiraling together. The strongest radiation is emitted at merger, where the strong fields and lack of symmetry require the use of fully numerical methods for solving Einstein's equations. Numerical simulations of binary black holes require the specification of initial data to be used with evolution equations. The physics of a binary black hole system in numerical relativity will largely be determined by the initial data. This dissertation is concerned with the analysis and improvement of that initial data.

There will be two main parts to this dissertation. The first part will be concerned with how initial data is created. This starts with a presentation of the 3+1 decomposition which rewrites Einstein's field equations as a set of constraint and evolution equations. This will be followed with a discussion of the conformal thin-sandwich decomposition and excision methods which rewrite a portion of the 3+1 decomposition as a well-posed set of elliptic equations and boundary conditions that can be used to determine initial data. Then I will discuss the the physics of binary black holes, what physical measurements we can apply and how they are used to find astrophysically likely initial data for binary black holes. Lastly,

there will be a discussion of the implementation of these methods.

The second section will cover my own research into binary black hole initial data. I will describe tests of methods for finding binaries in quasicircular orbit, thought to be the most likely scenario for binary sources of gravitational waves. This is entwined with tests to better understand spin in binary black holes. I will then report on efforts to understand eccentricity in binary black hole initial data. Finally I will discuss efforts to improve methods for creating initial data by removing an assumption known to lead to errors — that of conformal flatness. This is replaced by an effort to numerically determine the conformal metric.

Chapter 1

Introduction

Einstein's General Theory of Relativity (GR) fundamentally changed the way we look at gravity. In GR, gravity is taken not as a force but rather the curvature of space and time itself. That curvature can bring two bodies together is relatively easy to demonstrate. Imagine two people starting at different points along the equator of the Earth. If they both walk north, initially their paths are parallel, but at the north pole, their paths will intersect. This is due to the curvature of the Earth. If you then consider time to be a dimension similar to the three spatial dimensions we are comfortable with, then particles travel along paths determined by the curvature of space-time. This was one half of Einstein's line of thought: that gravity as a force is supplanted by gravity as the curvature of space-time, and it is that curvature that drives the motion of particles. This has the now well observed effect of gravity changing the path of massless particles such as photons. That very effect has driven our understanding of gravitational lensing as a tool for seeing deeper into the universe. The other half of Einstein's line of thought was that the placement and movement of matter and energy determine the curvature of space.

The first concept, that curvature drives the motion of matter and energy, is represented by the equation of the geodesic:

$$\ddot{x}^{\beta} + \Gamma^{\beta}{}_{\sigma\alpha}\dot{x}^{\sigma}\dot{x}^{\alpha} = 0. \tag{1.1}$$

The second idea is represented by Einstein's field equations:

$$G_{\mu\nu} = 8\pi T_{\mu\nu}. \tag{1.2}$$

In Eq. (1.1), the dot represents not a time derivative, but rather a derivative with respect to some affine parameter. The $\Gamma^{\beta}{}_{\sigma\alpha}$'s are often called the connection or the Christofel symbol and are a set of derivatives taken on the metric describing the geometry of the space-time. The indices in Greek go from zero to three (as Greek indices will throughout this work) to span four dimensions. One dimension is time and the other three are spatial. In Eq. (1.2), the object on the left is commonly called the Einstein tensor, and represents a measure of the curvature of the space-time, while the object on the right is the stress energy tensor. Here and throughout this work I will use units where $G = c = 1$ and generally follow the conventions of MTW [57].

The pseudo-Riemannian geometry we are using in this work can be entirely described by the symmetric space-time metric tensor $g_{\mu\nu}$. The infinitesimal interval can be written as $ds^2 \equiv g_{\mu\nu}dx^\mu dx^\nu$. As can be seen in most any general relativity textbook (see [57] for a good presentation), if you take the metric as $g_{\mu\nu} = \eta_{\mu\nu} + h_{\mu\nu}$ where $\eta_{\mu\nu}$ is the Minkowski metric and $h_{\mu\nu}$ is taken to be small, one can recover, to linear order in $h_{\mu\nu}$, the wave equation in vacuum

$$\bar{h}_{\mu\nu;\alpha}{}^{\alpha} = 0. \tag{1.3}$$

In (1.3), each index after a semicolon means that a covariant derivative is taken with respect to the corresponding coordinate, repeated indices are summed over and the barred $h_{\mu\nu}$ means the trace has been "reversed", $\bar{h}_{\mu\nu} = h_{\mu\nu} - \frac{1}{2}\eta_{\mu\nu}h$. The nature of the summed indices might make this appear to be a Laplacian operator. Indeed, if this were a Riemannian geometry, the metric would have a signature all of the same sign $(+,+,+,+)$ and it would be a Laplacian. General Relativity, however, is done in a pseudo-Riemannian geometry with one part of the signature of the metric being opposite the others $(-,+,+,+)$. This means that when the summation occurs, the second time-derivative has a minus sign in front of

it. Thus Eq. (1.3) yields the D'Alembertian operator. This result implies the existence of gravitational waves or little ripples in the fabric of space-time.

Since Einstein first published his papers on general relativity, a number of analytical solutions have been derived in GR, and a number of predictions of the theory have been verified. The effect of gravity on massless particles, such as photons, has been seen, and is required to explain the gravitational-lensing effect. Global Positioning Systems would not be possible without a correction term obtained from GR. On the theoretical side, solutions which take advantage of symmetry, such as the Schwarzschild solution (a non-spinning spherically symmetric solution with a defining mass parameter M), and the Kerr solution (spinning axi-symmetric solution with the parameters M related to mass and a related to spin), have led us to the conclusion that the universe is populated with black holes. Black holes can come from stars whose gravity has overcome the pressures holding up their structure. This leads to a collapse and an apparent singularity surrounded by an event horizon, a barrier which causally disconnects one portion of space-time from another, such that light and information cannot escape from within the event horizon to spatial infinity. A collapsed star is just one possible source of a black hole. Other sources are primordial black holes, which originated at the start of the universe, or Planck scale black holes, which are created and instantly evaporate due to quantum effects. Pertubative methods, which include linearized gravity, but can also include higher order effects, have led to a better understanding of gravitational waves, and have led to better estimates of the dynamics of the sources of gravitational waves. These methods are particularly effective in the slow-moving, weak-field limit and binary systems in the extreme mass ratio regime. Despite all these advances, the detection, not to mention a full theoretical understanding, of gravitational waves themselves has yet to occur. The observational difficulty is primarily due to the fact that gravitation is far weaker than, for instance, the electromagnetic force. Their theoretical understanding has been hampered by the difficulty of solving the nonlinear Einstein field equations in all generality.

The problem of detection can only really be overcome by attempting to observe the gravitational waves of very strong sources, such as binary black holes on the order of tens of solar masses or greater, supernovae, binary neutron stars and other similarly powerful phenomena. Projects are in development to detect the waves and they include the Laser Interferometer Ground Observatory (LIGO) and the Laser Interferometric Space Antenna (LISA). As the names suggest, these devices use very large scale interferometers (LIGO having 4 kilometer arms and LISA having 5 million kilometer arms) to detect the small tidal distortions in space-time created by gravitational waves. LIGO is currently being updated with new equipment and methods in the hope that it will create an interferometer able to detect gravitational waves on an average of once a month, and projects analyzing the proposed LISA mission are currently under way at NASA and the ESA.

A likely candidate for gravitational wave detection by LIGO would be binary black-hole pairs in the stellar mass range. While analytical methods are adequate to estimate the behavior of these systems at larger separations, LIGO will only be able to detect the last few orbits of such a binary and the final coalescence into a single black hole. Although post-Newtonian pertubative methods have improved the analytical accuracy in this regime, the strong fields and high relative velocities close to merger inherently inhibit the accuracy of these approximations. This is one reason that numerical relativity (NR), the direct numerical simulation of Einstein's general theory of relativity, has been developed.

Numerical Relativity starts with what is known as a 3+1 (or ADM [2]) decomposition of Einstein's equations (1.2). This decomposition foliates space-time with slices of constant time. The decomposition then rewrites Einstein's equations as a set of constraint equations which the geometry of any given slice of constant time must conform to, and a set of evolution equations describing how to determine the geometry of the next slice from that of the current one. In essence, the ADM decomposition transforms the problem of solving Einstein's equations of general relativity into two parts, one of determining initial data (the initial geometry), and the other a problem of evolving that data forward in time. Largely,

the physics of an evolution will be determined by the initial data, and thus we need initial data that accurately model astrophysically likely scenarios. I have worked on analyzing the physics of, and improving our methods for calculating, binary black-hole initial data.

To present this work, it is useful to have a certain ammount of background provided. Chapter 2 will describe the ADM decomposition. The ADM decomposition identifies the constraint and evolution equations, but, for initial data, one still must determine what is constrained in the constraint equations. This is typically done with a type of conformal decomposition. The one I have used is the extended conformal thin-sandwich (ECTS) decomposition which is described in Chapter 3. The ECTS equations result in a set of elliptic differential equations for the constrained variables. Elliptic differential equations have the property that they can be combined with boundary conditions to create a well-posed boundary-value problem. Thus the boundary conditions I have used will be also presented in Chapter 3. The ECTS equations can provide a well-posed boundary-value problem but for the initial data to be useful, it must model astrophysically likely situations. Chapter 4 goes into detail on the physics of binary black holes and how we can model that physics in initial data. Many of the tools used for analysis of the two-body problem in other fields are simply not available in general relativity or initial data, and so Chapter 4 describess what analytical tools we have from the ground up. The implementation of all this is covered in Chapter 5 which presents Eric, a numerical code designed to solve sets of elliptic equations. Chapter 6 will go into some of my own research analyzing methods we use for finding binary black-hole initial data in circular orbits and with certain spins. Chapter 7 will describe my work to analyze the eccentricity of orbits of binary black holes and how this can be measured in initial data. Chapter 8 will cover my most recent work in improving our initial-data methods in such a way as to remove an assumption known to cause problems for evolutions — the assumption of conformal flatness. Some finishing remarks will then be made in Chapter 9.

Chapter 2

3+1 (ADM) Decomposition

As originally written, Einstein's equations provide a relation between a global space-time and the corresponding stress-energy tensor. Fully solving these ten coupled non-linear differential equations means simultaneously fully determining everything in the system throughout space-time. The difficulty of this task has led to relatively few analytical solutions, all of which make use of some non-general assumption and possibly some approximation method such as a series expansion. Already mentioned in the introduction are the asymptotically flat Schwarzschild and Kerr solutions along with post-Newtonian methods. In Cosmology, assumptions of homogeneity and isotropy are used to greatly simplify models of the universe. In all these solutions, either symmetry or weak relativistic effects have been assumed. It is likely the first detections of gravitational waves will come from very strong, fast moving systems lacking symmetry. In fact, strong symmetries tend to suppress the possibility of gravitational waves. To deal with the inherit difficulties for the systems in question, a dynamical perspective was taken in [2]. The 3+1, or ADM, decomposition presented therein reformulates Einstein's equations in terms of a set of constraint equations that the geometry must always satisfy and a set of evolution equations to find the future space-time given sufficient information about the geometry of some instant in time. Even on the most analytical level, this decomposition removes the need to fully define the space-time to spatial and temporal infinities. This method enables relativists to focus on a portion of space-time that is of interest.

In this chapter is a presentation of the derivation of the 3+1 equations based directly on the thorough discussions found in [76, 39, 26, 13]. Following the choices in [26], the metric $g_{\mu\nu}$ will be taken to have a signature of $(\epsilon, +, +, ...)$ where $\epsilon = -$ for a pseudo-Riemannian geometry and $\epsilon = +$ to represent a Riemannian geometry. While this might seem to make the equations harder to read, it makes the results easily applicable to any $\mathtt{N}+\mathtt{1}$ decomposition where $\mathtt{N}+\mathtt{1}$ is the total dimension of the space in question. This generality will be useful in a later chapter when considering boundary conditions.

To start, define a scalar function τ that covers the space. One needs an $\mathtt{N}+\mathtt{1}$ dimensional space V to be covered by a foliation $\{\Sigma\}$ of non-intersecting slices Σ. Surfaces of constant τ will be treated as the individual slices Σ. Because τ defines non-intersecting surfaces that fill the space, one can define, in all generality, a closed one-form $\underset{\sim}{\Omega} = \Omega_\mu \underset{\sim}{e^\mu}$, where $\underset{\sim}{e^\mu}$ represents a general basis of forms, and $\underset{\sim}{\Omega} \equiv \mathrm{d}\tau$ or equivalently $\Omega_\mu = \nabla_\mu \tau$. $\underset{\sim}{\Omega}$ being closed can be equivalently expressed as

$$\mathrm{d}\underset{\sim}{\Omega} = 0 \quad \text{or} \quad \nabla_{[\mu}\Omega_{\nu]} = 0. \tag{2.1}$$

From this closed one form, we can introduce a lapse function α defining a characteristic separation between slices:

$$\|\Omega\|^2 = g^{\mu\nu}\Omega_\mu\Omega_\nu = g^{\mu\nu}\nabla_\mu\tau\nabla_\nu\tau \equiv \epsilon\alpha^{-2}. \tag{2.2}$$

Now we can write a normalized one form:

$$\omega_\mu \equiv \alpha\Omega_\mu = \alpha\nabla_\mu\tau, \quad \|\omega\|^2 = \epsilon 1. \tag{2.3}$$

We can then define the vector normal to the surface based on the dual to the one-form:

$$n^\mu \equiv \epsilon g^{\mu\nu}\omega_\nu. \tag{2.4}$$

Here the ϵ has been included to insure n^μ points in a positive time-like direction. We can now find the spatial metric for a slice Σ of the foliation:

$$\gamma_{\mu\nu} \equiv g_{\mu\nu} - \epsilon n_\mu n_\nu = g_{\mu\nu} - \epsilon\omega_\mu\omega_\nu. \tag{2.5}$$

The inverse of the spatial metric is found by contracting twice with the inverse metric:

$$\gamma^{\mu\nu} = g^{\mu\alpha} g^{\nu\beta} \gamma_{\alpha\beta} = g^{\mu\nu} - \epsilon n^\mu n^\nu. \tag{2.6}$$

To find the portions of a tensor in a surface and normal to a surface, we need to find two projection operators, one for the surface and one for the normal. We find that

$$\perp^\mu_\nu \equiv \gamma^\mu_\nu = \delta^\mu_\nu - \epsilon n^\mu n_\nu \tag{2.7}$$

provides such a projection into Σ, as $\perp^\mu_\nu n_\mu = 0$. We also see that

$$N^\mu_\nu \equiv \epsilon n^\mu n_\nu \tag{2.8}$$

provides the projection onto the normal of Σ, as $N^\mu_\nu n_\mu = n_\nu$. The following relations are also clear:

$$\begin{gathered} \perp^\mu_\beta \perp^\beta_\nu = \perp^\mu_\nu \ ; \ \perp^\mu_\mu = \mathtt{N}, \quad \text{and} \\ N^\mu_\beta N^\beta_\nu = N^\mu_\nu \ ; \ N^\mu_\mu = 1. \end{gathered} \tag{2.9}$$

Note that $\mathtt{N}$ without indices here is taken from $\mathtt{N} + \mathtt{1}$ as opposed to the trace of the operator N^μ_ν. We can define the derivative compatible with the spatial-metric acting on a tensor:

$$D_\mu T_\nu = \perp^\alpha_\mu \perp^\beta_\nu \nabla_\alpha T_\beta \equiv \perp \nabla_\mu T_\nu. \tag{2.10}$$

While here the derivative is acting on a rank (0,1) tensor, it can be extended to any rank tensor by appropriately adding the projection operator for each index. Note that $\perp$ has been substituted as shorthand for representing one operator $\perp^\alpha_\mu$ for each free index. It can be shown that a covariant derivative with respect to the slice must act only on objects in that slice for Liebnitz's rule to hold. One can now show D_μ is truly compatible with the metric of the slice:

$$D_\alpha \gamma_{\mu\nu} = 0. \tag{2.11}$$

Our goal is to decompose Einstein's field equations using these tools, and so we need to look into definitions of curvature. With a surface embedded in a higher-dimensional

space, there is both an intrinsic Riemann curvature and an extrinsic curvature more akin to curvature as most people see it in their everyday lives. With a derivative covariant with the metric embedded in the slice, one can proceed to define the intrinsic curvature of a slice Σ the same as one would for any space. If W_σ is a one-form entirely in the spatial slice, then

$$[D_\mu, D_\nu]W_\sigma = W_\rho \, {}^{\mathtt{N}}R^\rho{}_{\sigma\nu\mu}. \tag{2.12}$$

Here, the $\mathtt{N}$ is to make clear that ${}^{\mathtt{N}}R$ is the Riemann tensor describing the intrinsic curvature of the of the $\mathtt{N}$-dimensional subspace only. Clearly, contracting the Riemann tensor of the $\mathtt{N}$-dimensional slice with the normal to that slice yields zero.

The $\mathtt{N}$-space intrinsic curvature can be found directly from information contained only in the metric for the spatial slice. Another tool is needed then to fully describe how a given slice Σ is embedded in the overall space-time $\{\Sigma\}$. We refer to this as the extrinsic curvature $K_{\mu\nu}$. This embedding is naturally dependent on some kind of gradient of the normal to the surface, or how the normal changes as you move along the surface. There can be two pieces of this, a symmetric strain $\Theta_{\mu\nu} \equiv\perp \nabla_{(\mu} n_{\nu)}$ and an antisymmetric twist $\omega_{\mu\nu} \equiv\perp \nabla_{[\mu} n_{\nu]}$. Remember that n^μ is surface-forming in its definition, thus the completely antisymmetric combination $n_{[\mu}\nabla_\nu n_{\sigma]} = 0$ and we find

$$\begin{aligned} 0 &= \perp n^\mu(n_{[\mu}\nabla_\nu n_{\sigma]}) = \frac{1}{3} \perp \left(\epsilon\nabla_{[\nu} n_{\sigma]} + n^\mu \left(n_\sigma \nabla_{[\mu} n_{\nu]} - n_\nu \nabla_{[\mu} n_{\sigma]}\right)\right) \\ &= \epsilon\frac{1}{3} \perp \nabla_{[\nu} n_{\sigma]} = \epsilon\frac{1}{3}\omega_{\nu\sigma} = 0. \end{aligned} \tag{2.13}$$

The second line of Eq. (2.13) comes about because the action of the perp operator $\perp$ on the normal n^μ returns zero. All that is left is the strain, and one includes a factor of ϵ by convention:

$$K_{\mu\nu} \equiv \epsilon\Theta_{\mu\nu} = \epsilon \perp \nabla_{(\mu} n_{\nu)}. \tag{2.14}$$

It is equivalent to say that the extrinsic curvature is the same as the part of the Lie derivative along the normal of the space-time metric parallel to the slice:

$$K_{\mu\nu} = \epsilon\frac{1}{2} \perp \mathcal{L}_{\mathbf{n}} g_{\mu\nu}. \tag{2.15}$$

It is worth noting that the metric induced on the slice $\gamma_{\mu\nu}$ and the extrinsic-curvature of that slice are enough to fully describe the geometry of the slice and its embedding in the hyper-dimensional volume. If such information were generally available for all slices Σ in the space-time $\{\Sigma\}$, that information would completely define the geometry of the volume.

In detail, there are two tasks left in arriving at the ADM decomposed equations. There is a set of conditions that should be met for any slice to fully fit into a foliation, commonly called the Gauss-Codazzi-Ricci (GCR) conditions. The GCR relations are found by taking all possible projections of the Riemann tensor both within and normal to the slice. After finishing the GCR conditions, we take advantage of the coordinate freedom in defining a time vector. Before deriving the GCR conditions, however, it is neccesary to see other ways to write the extrinsic curvature. Since it appears in Eq. (2.14), we'll start by taking the gradient of the normal to the hyper-surface:

$$\begin{aligned} \nabla_\mu n_\nu &= \delta^\alpha_\mu \delta^\beta_\nu \nabla_\alpha n_\beta = \left(\perp^\alpha_\mu + \epsilon n^\alpha n_\mu\right)\left(\perp^\beta_\nu + \epsilon n^\beta n_\nu\right)\nabla_\alpha n_\beta \\ &= \perp \nabla_\mu n_\nu + \epsilon n_\mu \perp a_\nu. \end{aligned} \tag{2.16}$$

Here $a_\mu \equiv n^\nu \nabla_\nu n_\mu$. Since we know the magnitude of the unit normal is constant,

$$0 = \nabla_\mu (n^\nu n_\nu) = 2 n^\nu \nabla_\mu n_\nu. \tag{2.17}$$

Contracting (2.17) again with the normal, we see that

$$0 = n^\mu \nabla_\mu (n^\nu n_\nu) = 2 n^\nu n^\mu \nabla_\mu n_\nu = 2 n^\nu a_\nu, \tag{2.18}$$

from which it is clear the acceleration of the normal is an entirely spatial object, thus making the second $\perp$ operator at the end of (2.16) irrelevant. It can now be seen that

$$K_{\mu\nu} = \epsilon \nabla_{(\mu} n_{\nu)} - n_{(\mu} a_{\nu)}. \tag{2.19}$$

A final form of the extrinsic curvature can be seen by taking the Lie derivative along the

normal of the spatial metric:

$$\begin{aligned}\mathcal{L}_{\mathbf{n}}\gamma_{\mu\nu} &= \mathcal{L}_{\mathbf{n}}(g_{\mu\nu} - \epsilon n_\mu n_\nu) \\ &= 2\left(\nabla_{(\mu}n_{\nu)} - \epsilon n_{(\mu}a_{\nu)}\right) \\ &= \epsilon 2K_{\mu\nu}.\end{aligned} \tag{2.20}$$

With these other forms of the extrinsic curvature in hand, we will now find the GCR relations in order to reconstruct Einstein's equations. We'll start with the second derivative of a vector. In particular, we'll take two spatial gradients of a vector. For this, we will find it useful to examine the gradient of the perp-operator:

$$\begin{aligned}\nabla_\sigma \perp^\mu_\nu &\equiv \nabla_\sigma\left(\delta^\mu_\nu - \epsilon n^\mu n_\nu\right) = -\epsilon\nabla_\sigma\left(n^\mu n_\nu\right) \\ &= -n_\nu K_\sigma{}^\mu - n_\nu n_\sigma a^\mu - n^\mu K_{\sigma\nu} - n^\mu n_\sigma a_\nu.\end{aligned} \tag{2.21}$$

Now look at the second spatial derivative of a vector

$$\begin{aligned}D_\mu D_\nu V_\rho &= \perp\nabla_\mu\left(\perp\nabla_\nu V_\rho\right) \\ &= \perp\nabla_\mu\nabla_\mu V_\rho + \perp\left(\nabla_\nu V_\sigma\right)\left(\nabla_\mu \perp^\sigma_\rho\right) + \perp\left(\nabla_\sigma V_\rho\right)\left(\nabla_\mu \perp^\sigma_\nu\right)\end{aligned} \tag{2.22}$$

and insert Eq.(2.21) into Eq.(2.22):

$$D_\mu D_\nu V_\rho = \perp\nabla_\mu\nabla_\nu V_\rho + \epsilon \perp K_{\mu\rho}K_\nu{}^\sigma V_\sigma + \epsilon \perp K_{\mu\nu}n^\sigma\nabla_\sigma V_\rho. \tag{2.23}$$

Now we can use this result with the definition of the Riemann tensor to find (removing the vector from the equation)

$$\perp {}^{\mathtt{N+1}}R_{\mu\nu\rho\sigma} = {}^{\mathtt{N}}R_{\mu\nu\rho\sigma} - \epsilon K_{\mu\rho}K_{\nu\sigma} + \epsilon K_{\mu\sigma}K_{\nu\rho}. \tag{2.24}$$

This fully projected Riemann tensor is known as Gauss's equation. We will next contract one index of the full $\mathtt{N}+\mathtt{1}$ dimensional Riemann curvature with the unit normal and use the perp operator on the result. It will be useful here to note that

$$\begin{aligned}\perp\nabla_\mu\nabla_\nu n_\rho &= \perp\nabla_\mu\left(\epsilon K_{\nu\rho} + \epsilon n_\nu a_\rho\right) \\ &= \epsilon D_\mu K_{\nu\rho} + \epsilon \perp\left(a_\rho\nabla_\mu n_\nu\right) = \epsilon D_\mu K_{\nu\rho} + a_\rho K_{\mu\nu}.\end{aligned} \tag{2.25}$$

We can then use the above to get

$$\perp {}^{\mathtt{N+1}}R_{\mu\nu\rho}{}^{\sigma}n_{\sigma} = \perp (\nabla_{\mu}\nabla_{\nu}n_{\rho} - \nabla_{\nu}\nabla_{\mu}n_{\rho}) = -\epsilon D_{\nu}K_{\mu\rho} + \epsilon D_{\mu}K_{\nu\rho}, \tag{2.26}$$

which is known as Codazzi's equation.

Note that Gauss's and Codazzi's equations use only the spatial metric, the extrinsic curvature and spatial derivatives. These are conditions that the spatial slice must conform to to fit within the foliation. These lead directly to the constraint equations which will be shown below. For now, we are interested in Ricci's equation which involves the Lie derivative along the normal of the extrinsic curvature, which can be shown to be

$$\begin{aligned} -\epsilon\mathcal{L}_{\mathbf{n}}K_{\mu\nu} &\equiv -\epsilon n^{\rho}\nabla_{\rho}K_{\mu\nu} - \epsilon K_{\mu\rho}\nabla_{\nu}n^{\rho} - \epsilon K_{\rho\nu}\nabla_{\mu}n^{\rho} \\ &= {}^{\mathtt{N+1}}R_{\mu\rho\nu}{}^{\sigma}n^{\rho}n_{\sigma} - K_{\mu\rho}K_{\nu}{}^{\rho} - K_{\mu\rho}n_{\nu}a^{\rho} \\ &\quad - \nabla_{\mu}a_{\nu} + \epsilon a_{\mu}a_{\nu} + \epsilon n_{\mu}n^{\rho}\nabla_{\rho}a_{\nu}. \end{aligned} \tag{2.27}$$

Using the $\perp$ operator, one can show

$$\perp {}^{\mathtt{N+1}}R_{\mu\rho\nu}{}^{\sigma}n^{\rho}n_{\sigma} = -\epsilon\mathcal{L}_{\mathbf{n}}K_{\mu\nu} + K_{\mu\rho}K_{\nu}{}^{\rho} - \epsilon a_{\mu}a_{\nu} + D_{\mu}a_{\nu}, \tag{2.28}$$

which is Ricci's equation.

It is notable that the Lie derivative in Ricci's equation as presented above is along the normal to the surface only. Now we are ready to define a time vector dictating how the coordinates move between slices. Next define the vector t^{μ} as the dual to the natural surface-forming one-form:

$$\Omega_{\mu}t^{\mu} = 1. \tag{2.29}$$

One solution is to take $t^{\mu} \equiv \alpha n^{\mu}$. This is not, however, a unique choice. We are free to add a shift to this vector so long as the shift is entirely in the spatial slice ($\Omega_{\mu}\beta^{\mu} = 0$)

$$t^{\mu} \equiv \alpha n^{\mu} + \beta^{\mu}. \tag{2.30}$$

This allows for a freedom in how the coordinates move from one slice to the next. It is useful then, in finding Ricci's equation, to show how the Lie derivative along the time vector acts

on the extrinsic curvature:

$$\mathcal{L}_{\mathbf{t}} K_{\mu\nu} = \mathcal{L}_{\alpha\mathbf{n}} K_{\mu\nu} + \mathcal{L}_{\beta} K_{\mu\nu} = \alpha \mathcal{L}_{\mathbf{n}} K_{\mu\nu} + \mathcal{L}_{\beta} K_{\mu\nu}. \tag{2.31}$$

Before inserting this into Ricci's equation, one should consider the acceleration a_μ. It can be related to the gradient of the lapse via

$$\begin{aligned} a_\mu &= n^\nu \nabla_\nu n_\mu = 2 n^\nu \nabla_{[\nu} n_{\mu]} = \epsilon 2 n^\nu \nabla_{[\nu}(\alpha \Omega_{\mu]}) = \epsilon n^\nu \left(\Omega_\mu \nabla_\nu \alpha - \Omega_\nu \nabla_\mu \alpha\right) \\ &= -\epsilon \alpha^{-1} (\perp \nabla_\mu \alpha) = -\epsilon D_\mu \ln \alpha. \end{aligned} \tag{2.32}$$

When we put (2.31) and (2.32) into Ricci's equation, we get the useful result

$$\perp {}^{\mathtt{N+1}}R_{\mu\rho\nu}{}^{\sigma} n^\rho n_\sigma = -\epsilon\alpha \mathcal{L}_{\mathbf{t}} K_{\mu\nu} + K_{\mu\rho} K_\nu{}^\rho - \epsilon \alpha^{-1} D_\mu D_\nu \alpha + \epsilon \alpha^{-1} \mathcal{L}_\beta K_{\mu\nu}. \tag{2.33}$$

We have put together the Gauss-Codazzi-Ricci equations with the express purpose of decomposing the full rank-4 $\mathtt{N}+\mathtt{1}$-dimensional Riemann tensor. Once that is done, we can contract the Riemann tensor to find the Ricci tensor and Ricci scalar needed for Einstein's equations. We'll finish by writing out the Riemann tensor in terms of its perpendicular and normal projections:

$$\begin{aligned} {}^{\mathtt{N+1}}R_{\mu\nu\rho\sigma} &= \perp {}^{\mathtt{N+1}}R_{\mu\nu\rho\sigma} - (\epsilon n_\mu \perp {}^{\mathtt{N+1}}R_{\rho\sigma\nu\delta} - \epsilon n_\nu \perp {}^{\mathtt{N+1}}R_{\rho\sigma\mu\delta} \\ &\quad + \epsilon n_\rho \perp {}^{\mathtt{N+1}}R_{\mu\nu\sigma\delta} - \epsilon n_\sigma \perp {}^{\mathtt{N+1}}R_{\mu\nu\rho\delta}) n^\delta \\ &\quad + (n_\mu n_\rho \perp {}^{\mathtt{N+1}}R_{\nu\delta\sigma\gamma} - n_\mu n_\sigma \perp {}^{\mathtt{N+1}}R_{\nu\delta\rho\gamma} \\ &\quad + n_\nu n_\sigma \perp {}^{\mathtt{N+1}}R_{\mu\delta\rho\gamma} - n_\nu n_\rho \perp {}^{\mathtt{N+1}}R_{\mu\delta\sigma\gamma}) n^\delta n^\gamma. \end{aligned} \tag{2.34}$$

By inserting the Gauss-Codazzi-Ricci equations, we get

$$\begin{aligned} {}^{\mathtt{N+1}}R_{\mu\nu\rho\sigma} &= {}^{\mathtt{N}}R_{\mu\nu\rho\sigma} - \epsilon K_{\mu\rho} K_{\nu\sigma} + \epsilon K_{\mu\sigma} K_{\nu\rho} \\ &\quad - 2 n_\mu D_{[\rho} K_{\sigma]\nu} - 2 n_\nu D_{[\sigma} K_{\rho]\mu} - 2 n_\rho D_{[\mu} K_{\nu]\sigma} - 2 n_\sigma D_{[\nu} K_{\mu]\rho} \\ &\quad + n_\mu n_\rho \left(-\epsilon\alpha^{-1} \mathcal{L}_{\mathbf{t}} K_{\nu\sigma} + K_{\nu\delta} K_\sigma{}^\delta - \epsilon \alpha^{-1} D_\nu D_\sigma \alpha + \epsilon \alpha^{-1} \mathcal{L}_\beta K_{\nu\sigma}\right) \\ &\quad - n_\nu n_\rho \left(-\epsilon\alpha^{-1} \mathcal{L}_{\mathbf{t}} K_{\mu\sigma} + K_{\mu\delta} K_\sigma{}^\delta - \epsilon \alpha^{-1} D_\mu D_\sigma \alpha + \epsilon \alpha^{-1} \mathcal{L}_\beta K_{\mu\sigma}\right) \\ &\quad + n_\nu n_\sigma \left(-\epsilon\alpha^{-1} \mathcal{L}_{\mathbf{t}} K_{\mu\rho} + K_{\mu\delta} K_\rho{}^\delta - \epsilon \alpha^{-1} D_\mu D_\rho \alpha + \epsilon \alpha^{-1} \mathcal{L}_\beta K_{\mu\rho}\right) \\ &\quad - n_\mu n_\sigma \left(-\epsilon\alpha^{-1} \mathcal{L}_{\mathbf{t}} K_{\nu\rho} + K_{\nu\delta} K_\rho{}^\delta - \epsilon \alpha^{-1} D_\nu D_\rho \alpha + \epsilon \alpha^{-1} \mathcal{L}_\beta K_{\nu\rho}\right). \end{aligned} \tag{2.35}$$

At this point, I will drop the N notation and simply set N = 3. We can find the Ricci tensor by contracting the first and third indices. This is made easier by the fact that the three-dimensional Riemann tensor is defined purely spatially:

$$\begin{aligned} {}^4R_{\mu\nu} &= {}^3R_{\mu\nu} - \epsilon K K_{\mu\nu} + \epsilon 2 K_{\mu\rho} K_\nu{}^\rho - \alpha^{-1}\mathcal{L}_{\mathbf{t}} K_{\mu\nu} - \alpha^{-1} D_\mu D_\nu \alpha \\ &\quad + \alpha^{-1}\mathcal{L}_\beta K_{\mu\nu} - n_\mu \left(D_\nu K - D_\rho K_\nu{}^\rho\right) - n_\nu \left(D_\mu K - D_\rho K_\mu{}^\rho\right) \\ &\quad + n_\mu n_\nu \left(-\epsilon\alpha^{-1}\mathcal{L}_{\mathbf{t}} K - K_\rho{}^\sigma K_\sigma{}^\rho - \epsilon\alpha^{-1} D^\rho D_\rho \alpha + \epsilon\alpha^{-1}\mathcal{L}_\beta K\right). \end{aligned} \tag{2.36}$$

Here, the trace of the extrinsic curvature is defined as $K \equiv g^{\mu\nu}K_{\mu\nu} = \gamma^{\mu\nu}K_{\mu\nu}$. Taking the trace of the Ricci tensor, we get the Ricci scalar:

$${}^4R = {}^3R - \epsilon K^2 - \epsilon K_\rho{}^\sigma K_\sigma{}^\rho - 2\alpha^{-1}\mathcal{L}_{\mathbf{t}} K - 2\alpha^{-1} D^\rho D_\rho \alpha + 2\alpha^{-1}\mathcal{L}_\beta K. \tag{2.37}$$

At last we are ready to look at Einstein's equations. In fully covariant form, the field equations relate the Einstein tensor $G_{\mu\nu}$ to the stress energy tensor $T_{\mu\nu}$:

$$G_{\mu\nu} \equiv R_{\mu\nu} - \frac{1}{2} g_{\mu\nu} R = 8\pi T_{\mu\nu}. \tag{2.38}$$

With expressions for the Ricci scalar and Ricci tensor, we can decompose the stress-energy tensor and examine Einstein's equations to find our constraint and evolution equations.

In the same spirit as defining the Ricci scalar and tensor in a 3+1 manner, let us define parts of the stress-energy tensor using various projections. If we define an energy density $\rho \equiv n^\mu n^\nu T_{\mu\nu}$, a current density $j_\mu \equiv \epsilon \perp T_{\mu\nu} n^\nu$ and a spatial stress tensor $S_{\mu\nu} \equiv \perp T_{\mu\nu}$, the total stress-energy tensor can be written as

$$T_{\mu\nu} = S_{\mu\nu} + 2n_{(\mu} j_{\nu)} + n_\mu n_\nu \rho. \tag{2.39}$$

Tracing Einstein's equations gives us ${}^4R = -8\pi T = -8\pi(S + \epsilon\rho)$. By replacing the Ricci scalar in Einstein's equations using this trace and using the above definition for the stress-energy tensor, we can arrive at the following useful form:

$${}^4R_{\mu\nu} = 8\pi \left(S_{\mu\nu} + 2n_{(\mu} j_{\nu)} - \frac{1}{2}\gamma_{\mu\nu}(S + \epsilon\rho) - \frac{1}{2}\epsilon n_\mu n_\nu (S - \epsilon\rho)\right). \tag{2.40}$$

From here, one can identify the constraint and evolutions equations by taking projections of the above equation. We find the Hamiltonian constraint by contracting Eq. (2.40) twice with the unit normal to the surface:

$$\begin{aligned} {}^4R_{\mu\nu}n^\mu n^\nu &= -\epsilon\alpha^{-1}\mathcal{L}_{\mathbf{t}}K - K_\mu{}^\nu K_\nu{}^\mu - \epsilon\alpha^{-1}D^\mu D_\mu\alpha + \epsilon\alpha^{-1}\mathcal{L}_\beta K \\ &= -\frac{\epsilon}{2}\left({}^3R - \epsilon K^2 + \epsilon K_\mu{}^\nu K_\nu{}^\mu + 8\pi T\right) = -\frac{\epsilon 8\pi}{2}\left(S - \epsilon\rho\right). \end{aligned} \tag{2.41}$$

Using the trace of the stress-energy tensor, this can be simplified to

$${}^3R - \epsilon K^2 + \epsilon K_\mu{}^\nu K_\nu{}^\mu = -\epsilon 16\pi\rho. \tag{2.42}$$

Eq. (2.42) is the Hamiltonian constraint.

In similar fashion, the momentum constraint can be found by contracting once with the unit normal and then using the perp operator on the result:

$$\perp\ {}^4R_{\mu\nu}n^\nu = -\epsilon(D_\mu K - D_\nu K_\mu{}^\nu) = \epsilon 8\pi j_\mu. \tag{2.43}$$

This is often rewritten as

$$D_\nu\left(K^{\mu\nu} - \gamma^{\mu\nu}K\right) = 8\pi j^\mu. \tag{2.44}$$

When considering the evolution equations, it should be understood that we already have one of them. The definition of the extrinsic curvature can be viewed as the evolution equations for the spatial metric and is written as

$$\mathcal{L}_{\mathbf{t}}\gamma_{\mu\nu} = \epsilon 2\alpha K_{\mu\nu} + \mathcal{L}_\beta\gamma_{\mu\nu}. \tag{2.45}$$

Finally, the evolution equation for the extrinsic curvature is found by using the perp operator on the Ricci tensor without any contractions:

$$\begin{aligned} \perp {}^4R_{\mu\nu} &= {}^3R_{\mu\nu} - \epsilon K K_{\mu\nu} + \epsilon 2K_{\mu\rho}K_\nu{}^\rho - \alpha^{-1}\mathcal{L}_{\mathbf{t}}K_{\mu\nu} \\ &\quad - \alpha^{-1}D_\mu D_\nu\alpha + \alpha^{-1}\mathcal{L}_\beta K_{\mu\nu} \\ &= 8\pi\left(S_{\mu\nu} - \frac{1}{2}\gamma_{\mu\nu}(S + \epsilon\rho)\right). \end{aligned} \tag{2.46}$$

As an evolution equation, it is often written by isolating the time derivative:

$$\begin{aligned}\mathcal{L}_{\mathbf{t}} K_{\mu\nu} &= \epsilon D_\mu D_\nu \alpha - \epsilon\alpha\, {}^{(3)}R_{\mu\nu} - 2\alpha K_{\mu\rho} K_\nu{}^\rho + \alpha K K_{\mu\nu} \\ &\quad + \mathcal{L}_\beta K_{\mu\nu} + \epsilon\alpha 8\pi \left(S_{\mu\nu} - \frac{1}{2}\gamma_{\mu\nu}(S + \epsilon\rho) \right). \end{aligned} \tag{2.47}$$

While Eqs. (2.42), (2.44), (2.45) and (2.47) make the full $3+1$ decomposition of Einstein's field equations, their usefulness for numerical relativity requires one to make a choice for the basis vectors to be used for calculation. It is important to start by examining the basis of forms and its dual, the basis of vectors:

$$\langle \underset{\sim}{e}^\mu, \bar{e}_\nu \rangle = \delta^\mu_\nu. \tag{2.48}$$

One can safely choose one basis vector to be in the direction of time:

$$\bar{t} = t^\mu \bar{e}_\mu = \bar{e}_0, \tag{2.49}$$

set the others to be spatial (Latin indices will represent 1-3), require

$$\langle \underset{\sim}{\Omega}, \bar{e}_i \rangle = 0, \tag{2.50}$$

and demand that they commute with the time-like basis:

$$[\bar{t}, \bar{e}_i] = \mathcal{L}_{\mathbf{t}} \bar{e}_i = 0. \tag{2.51}$$

We can then show that the spatial vectors remain spatial as they are dragged along time.

$$\begin{aligned}\mathcal{L}_{\mathbf{t}} \langle \underset{\sim}{\Omega}, \bar{e}_i \rangle &= \langle \mathcal{L}_{\mathbf{t}} \underset{\sim}{\Omega}, \bar{e}_i \rangle = (\mathcal{L}_{\mathbf{t}} \Omega_\nu) \langle \underset{\sim}{e}^\nu, \bar{e}_i \rangle \\ &= (t^\rho \nabla_\rho \Omega_\nu + \Omega_\rho \nabla_\nu t^\rho) \langle \underset{\sim}{e}^\nu, \bar{e}_i \rangle \\ &= \left(2t^\rho \nabla_{[\rho} \Omega_{\nu]} + t^\rho \nabla_\nu \Omega_\rho + \Omega_\rho \nabla_\nu t^\rho \right) \langle \underset{\sim}{e}^\nu, \bar{e}_i \rangle = 0 \end{aligned} \tag{2.52}$$

On the last line, the first term is zero by definition of Ω, and the second and third terms combine to zero by Eq. (2.29).

These choices provide an "adapted basis", allowing us to write Lie derivatives along time as partial derivatives with respect to time, and allowing us to rewrite the components

of spatial objects purely with spatial indices. For instance, (2.50) shows us that $n_i = 0$. That, and the definition of time we have taken, means that $n^\mu = [\ -\epsilon\alpha^{-1},\ \epsilon\alpha^{-1}\beta^i\ ]$ and $n_\mu = [\ \epsilon\alpha,\ 0,\ 0,\ 0\ ]$. Further, we can find $\gamma_{ij} = g_{ij}$ and

$$\gamma^{\mu\nu} = \begin{bmatrix} 0 & 0 \\ 0 & \gamma^{ij} \end{bmatrix}. \tag{2.53}$$

The result is the following line element, inverse metric, constraint equations and evolution equations where Latin indices run from one to three:

$$ds^2 = g_{\mu\nu}dx^\mu dx^\nu = \epsilon\alpha^2 dt^2 + \gamma_{ij}(dx^i + \beta^i dt)(dx^j + \beta^j dt), \tag{2.54}$$

$$g^{\mu\nu} = \begin{bmatrix} \epsilon\alpha^{-2} & -\epsilon\alpha^{-2}\beta^j \\ -\epsilon\alpha^{-2}\beta^i & \gamma^{ij} + \epsilon\alpha^{-2}\beta^i\beta^j \end{bmatrix}, \tag{2.55}$$

$$R - \epsilon K^2 + \epsilon K_{ij}K^{ij} = -\epsilon 16\pi\rho, \tag{2.56}$$

$$D_j(K^{ij} - \gamma^{ij}K) = -\epsilon 8\pi j^i, \tag{2.57}$$

$$\begin{aligned}\partial_t K_{ij} = \epsilon D_i D_j\alpha - \epsilon\alpha\left[R_{ij} + \epsilon 2K_{il}K_j{}^l - \epsilon K K_{ij} - 8\pi S_{ij} + \tfrac{1}{2}8\pi\gamma_{ij}(S + \epsilon\rho)\right] \\ +\beta^l D_l K_{ij} + K_{il}D_j\beta^l + K_{lj}D_i\beta^l,\end{aligned} \tag{2.58}$$

$$\partial_t\gamma_{ij} = -2\alpha K_{ij} + D_i\beta_j + D_j\beta_i. \tag{2.59}$$

Here I have removed any labels for spatial or space-time quantities as the entire set of equations is made of scalars, or purely spatial vectors and tensors. Whenever Latin indices are seen, the spatial metric γ_{ij} and its inverse γ^{ij} are used to lower and raise indices respectively.

Chapter 3

The Extended Conformal Thin-Sandwich Decomposition with Excision

The initial data of a configuration can be completely known by specifying values for the spatial metric $\tilde{\gamma}_{ij}$ and the extrinsic curvature K_{ij} that fulfills the constraint Eqs. (2.56) and (2.57). However, the constraints do not fix all the degrees of freedom in the initial data, and it is left to us to choose what is being constrained and what degrees of freedom we must specify. For the purpose of initial data within the context of numerical relativity, generally one turns to a class of conformal decompositions typified by the York-Lichnerowicz decomposition [52, 72, 73, 74] as a tool for isolating degrees of freedom. Over the years, many conformal decompositions have been developed (see [29] for an overview). Today, for the binary black-hole problem, there are two common conformal decompositions in use. The first is the puncture method [18], which makes use of an analytic solution to the momentum constraints and analytically removes singular parts of a conformal factor. This leaves only the task of solving for the non-singular part to numerical methods. The second is the extended conformal thin-sandwich decomposition (ECTS) [77] designed to make use of part of the evolution equations for the metric and extrinsic curvature to allow the numerical specification of more degrees of freedom in a more physically meaningful manner. Typically, for binary black holes, the ECTS equations are used with a technique called excision. Black

holes pose serious difficulties for numerical computation because they contain singularities in the domain which are difficult to represent numerically. While puncture methods remove the singularity by treating it analytically, excision avoids the singularity entirely by cutting the black hole out of the domain - an excision. Excising black holes leaves a new boundary in the domain for each black hole. These excision boundaries require boundary conditions, and for that I have used what are called quasiequilibrium boundary conditions. The goal of this chapter is to motivate and show the derivation of the ECTS approach and describe the quasiequilibrium excision boundary conditions. Together, these methods form the basis for most of the research presented in this dissertation. This work is largely taken from [26, 29, 33, 25]. Worth noting is the D_i notation for three dimensional derivatives has been dropped, as there are no longer any four-dimensional variables left in the equations being used. The ∇_i will denote a covariant spatial derivative. From here on, D_i will represent derivatives in two dimensions. This will be important for studying the boundary conditions.

Often in other branches of General Relativity, a conformal factor is found relating the space-time metric $g_{\mu\nu}$ to a conformal background space-time metric. Here we are interested in relating the purely spatial metric γ_{ij} to a conformal background metric:

$$\gamma_{ij} = \psi^4 \tilde{\gamma}_{ij}. \tag{3.1}$$

From here on, a tilde above a quantity refers to a conformal quantity which has its indices raised and lowered with the conformal metric defined above. Also, a derivative operator with a tilde will be compatible with the conformal spatial metric, $\tilde{\nabla}_i \tilde{\gamma}_{jk} = 0$. The conformal factor isolates one degree of freedom, leaving five degrees of freedom in the conformal metric. By demanding that the contraction of the conformal metric with its inverse results in a delta-function, it is easy to find the conformal relation for the inverse spatial metric:

$$\gamma^{ij} = \psi^{-4} \tilde{\gamma}^{ij}. \tag{3.2}$$

The key spatial geometric quantities of the connection and the curvature tensors and scalar can now be rewritten in terms of this conformal decomposition of the spatial metric.

One can rewrite the connection using its explicit form:

$$\begin{aligned}
\Gamma^{i}{}_{jk} &= \frac{1}{2}\gamma^{il}\left[\gamma_{jl,k}+\gamma_{kl,j}-\gamma_{jk,l}\right] \\
&= \frac{1}{2}\psi^{-4}\tilde{\gamma}^{il}\left[(\psi^4\gamma_{jl})_{,k}+(\psi^4\gamma_{kl})_{,j}-(\psi^4\gamma_{jk})_{,l}\right] \\
&= \tilde{\Gamma}^{i}{}_{jk}+2\psi^{-1}\left[\delta^{i}_{j}\tilde{\nabla}_k\ln\psi+\delta^{i}_{k}\tilde{\nabla}_j\ln\psi-\tilde{\gamma}_{jk}\tilde{\gamma}^{il}\tilde{\nabla}_l\ln\psi\right]. \qquad (3.3)
\end{aligned}$$

In the final result, $\tilde{\Gamma}^{i}{}_{jk}$ is the connection with respect to the conformal metric, and the second term can be defined as the difference in the connections related to the two spatial metrics: $\delta\Gamma^{i}{}_{jk}\equiv\Gamma^{i}{}_{jk}-\tilde{\Gamma}^{i}{}_{jk}$. It is important to note that while neither the connection for the physical metric nor the connection for the conformal metric are tensors, the difference between any two connections is a tensor. The next step is to examine the resulting Riemann curvature tensor. This is easiest to examine in terms of the difference between curvature tensors related to the two metrics:

$$\delta R_{ijk}{}^{l}\equiv R_{ijk}{}^{l}-\tilde{R}_{ijk}{}^{l}=\delta\Gamma^{l}{}_{ki,j}-\delta\Gamma^{l}{}_{kj,i}+\delta\Gamma^{m}_{ki}\delta\Gamma^{l}{}_{mj}-\delta\Gamma^{m}_{kj}\delta\Gamma^{l}{}_{mi}. \qquad (3.4)$$

Eq. 3.4 may seem like it is missing cross-terms that go like $\Gamma\delta\Gamma$. While those terms cancel with each other, the derivation is neither trivial, nor terribly insightful, and so the derivation has been omitted. The difference of the Ricci tensors is

$$\begin{aligned}
\delta R_{ij}=\delta R^{l}{}_{ilj} &= \delta\Gamma^{l}{}_{ij,l}-\delta\Gamma^{l}{}_{jl,i}+\delta\Gamma^{m}_{ji}\delta\Gamma^{l}{}_{lm}-\delta\Gamma^{m}_{li}\delta\Gamma^{l}{}_{jm} \\
&= -2\left[\tilde{\nabla}_i\tilde{\nabla}_j\ln\psi+\tilde{\gamma}_{ij}\tilde{\gamma}^{lm}\tilde{\nabla}_l\tilde{\nabla}_m\ln\psi\right] \\
&\quad +4\left[(\tilde{\nabla}_i\ln\psi)\tilde{\nabla}_j\ln\psi-\tilde{\gamma}_{ij}\tilde{\gamma}^{lm}(\tilde{\nabla}_l\ln\psi)\tilde{\nabla}_m\ln\psi\right]. \qquad (3.5)
\end{aligned}$$

Finally, the Ricci scalar is then found to be

$$\begin{aligned}
R=\gamma^{ij}R_{ij} &= \psi^{-4}\tilde{\gamma}^{ij}(\tilde{R}_{ij}+\delta R_{ij}) \\
&= \psi^{-4}\tilde{R}-8\psi^{-5}\tilde{\nabla}^2\psi. \qquad (3.6)
\end{aligned}$$

By inserting the Ricci scalar into the Hamiltonian constraint (2.56), one can see that as long as the conformal metric is positive definite, one can arrive at an elliptic operator acting

on ψ. Elliptic operators have the advantage of being numerically solvable when calculated over a domain with well-formed boundary conditions.

The fundamental difference in various conformal decompositions of the 3+1 equations is the treatment of the extrinsic curvature K_{ij}. Before continuing, it is worth reviewing the degrees of freedom in the extrinsic curvature. In the ADM decomposition, the two dynamical degrees of freedom both show up in the metric and the extrinsic curvature. That accounts for two degrees of freedom in the extrinsic curvature. Three degrees of freedom in the extrinsic curvature are constrained by the momentum constraint. As the extrinsic curvature is a symmetric rank-two three-dimensional tensor (in this case), it has a total of six degrees of freedom. The last degree of freedom has no other option than to be gauge. Most treatments of the extrinsic curvature start by removing the trace of the extrinsic curvature. This was made common by York [74, 75]. This is advantageous in that the trace of the extrinsic curvature can reasonably be treated as the gauge choice [37]. We thus write the trace-free portion of the extrinsic curvature as

$$A_{ij} \equiv K_{ij} - \frac{1}{3}\gamma_{ij}K. \tag{3.7}$$

Any symmetric trace-free tensor S^{ij} can be broken down into transverse and longitudinal parts:

$$S^{ij} = (LV)^{ij} + T^{ij}, \tag{3.8}$$

where T^{ij} is a symmetric, transverse traceless tensor ($\nabla_j T^{ij} = 0$ and $T^i_i = 0$), and

$$(LV)^{ij} \equiv \nabla^i V^j + \nabla^j V^i - \frac{2}{3}\gamma^{ij}\nabla_l V^l. \tag{3.9}$$

Separating out the symmetric, transverse traceless part of A_{ij} creates a vector (in this case V^i) that is constrained by the momentum constraint, and creates a tensor T^{ij} that is freely specifiable.

The conformal thin-sandwich decomposition is a generalization of this transverse-traceless decomposition in that it allows for a weighting of the transverse-traceless decomposition. That weighting is identified by specifying the extrinsic curvature using the

evolution equations for the spatial metric (2.59). Consider two slices of time t and t' which are related by $t' = t + \delta t$. The metrics on those slices can be related as $\gamma'_{ij} = \gamma_{ij} + (\partial_t \gamma_{ij})\delta t$. Since the conformal factor has been set to be constrained by the Hamiltonian constraint, we are not able to freely specify the evolution of the spatial geometry, but rather we can only specify the evolution of the conformal spatial geometry. To this end, we make the following definition on the trace free part of $\partial_t \gamma_{ij}$:

$$\begin{aligned} u_{ij} &\equiv \partial_t \gamma_{ij} - \frac{1}{3}\gamma_{ij}\gamma^{kl}\partial_t \gamma_{kl} = \partial_t \gamma_{ij} - \frac{1}{3}\gamma_{ij}\partial_t \ln \gamma = \gamma^{1/3}\partial_t(\gamma^{-1/3}\gamma_{ij}) \\ &= -2\alpha A_{ij} + (L\beta)_{ij}. \end{aligned} \tag{3.10}$$

Here γ is the determinant of γ_{ij}, and the last equality is found by removing the trace of Eq. (2.59). This can also be written as

$$u^{ij} = \gamma^{ik}\gamma^{jl}u_{kl} = -(\partial_t \gamma^{ij} - \frac{1}{3}\gamma^{ij}\gamma_{kl}\partial_t \gamma^{kl}) = -2\alpha A^{ij} + (L\beta)^{ij}. \tag{3.11}$$

Now, the conformal thin-sandwich decomposition, through the use of the dynamical equation for the spatial metric, takes the longitudinal part of the extrinsic curvature to be generated by the shift vector β^i, and the choice of the transverse traceless part becomes a choice of part of the time evolution of the spatial metric. Still, in order to isolate the portion of the time-evolution we can freely specify, we need to enact a conformal decomposition on u_{ij}, α and A_{ij}. For this, let's define

$$\tilde{u}_{ij} \equiv \partial_t \tilde{\gamma}_{ij} \tag{3.12}$$

with the demand that

$$\tilde{\gamma}^{ij}\tilde{u}_{ij} \equiv 0. \tag{3.13}$$

The last definition ensures all relevant quantities are scalars or tensors rather than scalar densities or tensor densities. The conformal weighting between u_{ij} and $\tilde{u}_{ij}$ can then be shown to be

$$u_{ij} = \psi^4 \tilde{u}_{ij}. \tag{3.14}$$

The following conformal weightings for the lapse and the traceless extrinsic curvature may seem arbitrary, however they simplify the resulting equations:

$$A_{ij} \equiv \psi^{-2}\tilde{A}_{ij}, \qquad A^{ij} = \psi^{-10}\tilde{A}^{ij}, \tag{3.15}$$

and

$$\alpha = \psi^6\tilde{\alpha}. \tag{3.16}$$

We also need to specify the conformal longitudinal operator

$$(\tilde{L}V)^{ij} \equiv 2\tilde{\nabla}^{(i}V^{j)} - \frac{2}{3}\tilde{\gamma}^{ij}\tilde{\nabla}_k V^k \tag{3.17}$$

and its conformal relation

$$(LV)^{ij} = \psi^4(\tilde{L}V)^{ij}. \tag{3.18}$$

This results in the following definitions for the conformal traceless extrinsic curvature:

$$\tilde{u}^{ij} = -2\tilde{\alpha}\tilde{A}^{ij} + (\tilde{L}\beta)^{ij}, \tag{3.19}$$

$$\tilde{u}_{ij} = -2\tilde{\alpha}\tilde{A}_{ij} + (\tilde{L}[\psi^{-4}\beta])_{ij}. \tag{3.20}$$

With these definitions, one can rewrite the momentum and Hamiltonian constraints in terms of the decomposed variable. The conformal thin-sandwich decomposition, in the absence of matter fields, can be summed up as

$$\gamma_{ij} = \psi^4\tilde{\gamma}_{ij}, \tag{3.21}$$

$$K^{ij} = \psi^{-10}\tilde{A}^{ij} + \frac{1}{3}\psi^{-4}\tilde{\gamma}^{ij}K, \tag{3.22}$$

$$\tilde{A}^{ij} = \frac{1}{2\tilde{\alpha}}\left((\tilde{L}\beta)^{ij} - \tilde{u}^{ij}\right), \tag{3.23}$$

$$\tilde{\Delta}_L\beta^i - (\tilde{L}\beta)^{ij}\tilde{\nabla}_j \ln\tilde{\alpha} - \frac{4}{3}\tilde{\alpha}\psi^6\tilde{\nabla}^i K = \tilde{\alpha}\tilde{\nabla}_j(\frac{1}{\tilde{\alpha}}\tilde{u}^{ij}), \tag{3.24}$$

$$\tilde{\nabla}^2\psi - \frac{1}{8}\psi\tilde{R} - \frac{1}{12}\psi^5K^2 + \frac{1}{8}\psi^{-7}\tilde{A}_{ij}\tilde{A}^{ij} = 0. \tag{3.25}$$

Here Eq. (3.24) is derived from the momentum constraint and Eq. (3.25) is derived from the Hamiltonian constraint. Also, the $\tilde{\Delta}_L$ operator is defined as

$$\tilde{\Delta}_L V^i \equiv \tilde{\nabla}_j(\tilde{L}V)^{ij} = \tilde{\nabla}^2V^i + \frac{1}{3}\tilde{\nabla}^i(\tilde{\nabla}_j V^j) + \tilde{R}^i_j V^j. \tag{3.26}$$

In this formulation, the freely specifiable data are the trace of the extrinsic curvature K, the conformal lapse function $\tilde{\alpha}$, the conformal metric $\tilde{\gamma}_{ij}$ and the time derivative of the conformal metric $\tilde{u}_{ij} \equiv \partial_t \tilde{\gamma}_{ij}$. Constrained by what turn out to be elliptic equations are the conformal factor ψ and the shift β^i.

The conformal thin-sandwich decomposition takes a dynamical view in decomposing the extrinsic curvature, thus aiding in the choice of the freely specifiable data $\tilde{u}_{ij} = \partial_t \tilde{\gamma}_{ij}$, which is a dynamical quantity. The ECTS decomposition uses another dynamical equation to replace $\tilde{\alpha}$ as a specified quantity with the partial time-derivative of trace of the extrinsic curvature $\partial_t K$, which is also a dynamical quantity. This is done by combining two relations. The first is the evolution equation for the extrinsic curvature (2.58), and the second is a relation for $\partial_t \gamma_{ij}$ that can be found in the conformal thin-sandwich decomposition.

This relation can be found by starting with a known equivalence:

$$\gamma^{ij} \partial_t \gamma_{ij} = \partial_t \ln \gamma = \partial_t \ln(\psi^{12} \tilde{\gamma}) = 12 \partial_t \ln \psi. \tag{3.27}$$

Eq. (3.27) makes use of the fact that $\partial_t \tilde{\gamma} = 0$, which can be found directly by examining the definition in Eq. (3.13). Next one contracts the 3+1 dynamical equation for the spatial metric:

$$\gamma^{ij} \partial_t \gamma_{ij} = 2(\nabla_k \beta^k - \alpha K). \tag{3.28}$$

Combining Eqs. (3.27) and (3.28) one gets

$$\begin{aligned} \partial_t \ln \psi &= \frac{1}{6} \left(\nabla_i \beta^i - \alpha K \right) \\ &= \frac{1}{6} \left(\tilde{\nabla}_i \beta^i + 6 \beta^i \tilde{\nabla}_i \ln \psi - \psi^6 \tilde{\alpha} K \right). \end{aligned} \tag{3.29}$$

Using the definition of u_{ij}, one can get the final result:

$$\begin{aligned} \partial_t \gamma_{ij} &= u_{ij} + \frac{2}{3} \gamma_{ij} (\nabla_k \beta^k - \alpha K) \\ &= \psi^4 \left[\tilde{u}_{ij} + \frac{2}{3} \tilde{\gamma}_{ij} (\tilde{\nabla}_k \beta^k + 6 \beta^k \tilde{\nabla}_k \ln \psi - \psi^6 \tilde{\alpha} K) \right]. \end{aligned} \tag{3.30}$$

This result shows how, in the conformal thin-sandwich decomposition, the evolution of the spatial metric is dependent on the choices of the freely specifiable data (K, $\tilde{u}_{ij}$ and $\tilde{\alpha}$) and on the constrained data (ψ and β^i).

The ECTS decomposition, on the other hand, uses the result in constructing the trace of the dynamical 3+1 equation for the extrinsic curvature, Eq. (2.58), and after considerable algebra and assuming vacuum conditions, arrives at the result:

$$\partial_t K = -\psi^5 \tilde{\nabla}^2 \tilde{\alpha} + \frac{1}{8}\psi^2 \tilde{\alpha}\tilde{R} + \frac{5}{12}\psi^6 \tilde{\alpha} K^2 + \frac{7}{8}\psi^{-6}\tilde{\alpha}\tilde{A}_{ij}\tilde{A}^{ij} + \beta^k \tilde{\nabla}_k K. \tag{3.31}$$

This is advantageous because it allows us to move from a decision for freely specifiable data from one of the conformal lapse $\tilde{\alpha}$ to one of the evolution of the trace of the extrinsic curvature $\partial_t K$. Since K can be treated as a gauge choice, it is fair then to treat $\partial_t K$ as a gauge choice (just extending one's choice into future slices of constant time).

Written all together, the vacuum extended conformal thin-sandwich (ECTS) decomposition can be summarized in Eqs. (3.21-3.25) and

$$\tilde{\nabla}^2 \tilde{\alpha} = -\psi^{-5}\partial_t K + \frac{1}{8}\psi^{-3}\tilde{\alpha}\tilde{R} + \frac{5}{12}\psi\tilde{\alpha}K^2 + \frac{7}{8}\psi^{-11}\tilde{\alpha}\tilde{A}_{ij}\tilde{A}^{ij} + \psi^{-5}\beta^k\tilde{\nabla}_k K. \tag{3.32}$$

K, $\partial_t K$, $\tilde{\gamma}^{ij}$ and $\tilde{u}^{ij} \equiv -\partial_t \tilde{\gamma}^{ij}$ are all freely specifiable in the ECTS equations. The variables ψ, β^i and $\tilde{\alpha}$ are then the constrained degrees of freedom. So far, these equations have been developed for any gauge and without regard to topology. The only limitation presented here is that I have set the matter terms to zero. In general, the ECTS equations can be written with matter terms. The next task is to define the domain on which to use these equations and proper boundary conditions to be applied on the boundaries.

As mentioned above, the study of binary black-hole initial data leads to a practical problem with the black holes themselves: a black hole contains a singularity in the space-time which is difficult to model numerically. There are two techniques in common use today to deal with the singularities in numerical relativity. Puncture methods rewrite the conformal factor as two pieces, one analytically written to contain the singular parts of the

metric and the other part solved for numerically with a modified Hamiltonian constraint. This means the infinite quantities associated with the singularity itself do not have to be stored or computed numerically. The other method avoids the singularity entirely by excising it from the domain. This creates, in the domain of calculation, an extra boundary for every black hole in the system being studied in addition to a general outer boundary. The boundary conditions used for this work , known as quasiequilibrium boundary conditions, were developed by Cook and Pfeiffer [30, 33], and an overview will be presented below.

The outer-boundary conditions are determined by the assumption that the space-time is asymptotically flat. If one takes r as the distance from the center of mass, then as $r \to \infty$, one imposes the following conditions:

$$\begin{aligned} \psi|_{r\to\infty} &= 1, \\ \beta^i|_{r\to\infty} &= (\mathbf{\Omega}_0 \times \mathbf{r})^i, \\ \alpha|_{r\to\infty} &= \tilde{\alpha}|_{r\to\infty} = 1. \end{aligned} \tag{3.33}$$

Here $\mathbf{\Omega}_0$ parametrizes the rotation of the system being studied. The choice of the condition on β^i is so the time vector $t^\mu = \alpha n^\mu + \beta^\mu$ helically follows this rotation of the system. Practically speaking, the condition on the shift is hard to implement on the outer boundary so this dominant term is subtracted from the shift throughout the domain and on any inner boundaries.

While the outer boundary conditions are quite general, the inner excision boundary conditions need to be much more carefully constructed. Previously, excision boundary conditions used in conjunction with topological arguments [56, 53, 16, 50] about wormholes have been used to find Dirchelet, Neumann and mixed-type conditions for the constrained variables. These methods have been successfully used for binary black holes with other decompositions [78, 23, 27, 32] but have been found to yield an ill-posed system of equations when used with the ECTS decomposition [43, 44].

As these topological arguments are only partially successful, one needs to look at

other ideas for boundary conditions on the excision. If one applies the idea of quasi-equilibrium, which in this context means that an approximate Killing vector exists, one can find boundary conditions for the excision surfaces. One might naturally think to set conditions which treat that excision as an event horizon. It is, however, impossible to know with certainty where an event horizon is located without complete knowledge of a space-time. Fortunately, one can identify an apparent horizon of a black hole simply by examining the geometry of the spatial slice and finding a marginally outer trapped surface (MOTS). A MOTS is defined as a surface S where the expansion θ of outgoing null rays k^μ is zero. It has been shown in Hawking and Ellis [48] that so long as a space-time is *future asymptotically predictable* from a asymptotically flat Cauchy spatial slice, any apparent horizon in that spatial slice is inside or coincident with an event horizon. In consideration of an apparent horizon, quasi-equilibrium would have us assume that a Killing vector exists at least on the apparent horizon. In practice, one would treat the apparent horizon as an isolated horizon [3, 38, 4, 61]. Together we demand the excision be a MOTS,

$$\theta|_S = 0, \tag{3.34}$$

and require the shear $\sigma_{\mu\nu}$ of the outgoing null rays to be zero on the surface:

$$\sigma_{\mu\nu}|_S = 0. \tag{3.35}$$

Examining the Raychaudhuri equation (note that the Ricci tensor here is the four-dimensional Ricci tensor),

$$\mathcal{L}_k\theta = -\frac{1}{2}\theta^2 - \sigma_{\mu\nu}\sigma^{\mu\nu} + \omega_{\mu\nu}\omega^{\mu\nu} - R_{\mu\nu}k^\mu k^\nu, \tag{3.36}$$

and noting that, since the null rays are surface forming, the twist $\omega_{\mu\nu}$ of those null rays must be zero, and the Ricci tensor must be zero since there is no matter, we find that $\mathcal{L}_k\theta|_S = 0$. This implies that the apparent horizon will initially evolve along k^μ, the outward pointing null vectors. Finally, we will impose a coordinate condition by demanding that the apparent horizon of the black holes at least initially does not move with respect to the coordinates. These assumptions will turn out to be enough to define boundary conditions on the excision

surface for the conformal factor ψ and the shift β^i. Originally, in [30], similar conditions regarding the expansion of ingoing null rays were used to devise a specific Robin-type condition on the lapse $\tilde{\alpha}$. However, it was shown in [33] that when put together, these quasiequilibrium conditions of the conformal factor, shift and lapse yielded a degenerate set of boundary conditions and thus led to an ill-posed elliptic system of equations. A non-quasiequilibrium boundary condition was needed on one of the variables. Applying an arbitrary Dirchelet, Neumann or Robin condition on the lapse was found to yield a well-posed elliptic system.

To examine these conditions in detail, the geometrical properties of the two-surface must be established. We will define a spatial normal to the two surface $s^\mu = [0, s^i]$ which is also orthogonal to the normal of the three surface, $s^\mu n_\mu = 0$. We then define a metric on the excision boundary as

$$h_{ij} \equiv \gamma_{ij} - s_i s_j. \tag{3.37}$$

These conformal weightings follow naturally:

$$h_{ij} = \psi^4 \tilde{h}_{ij}, \qquad h^{ij} = \psi^{-4} \tilde{h}^{ij}, \tag{3.38}$$

$$s_i = \psi^2 \tilde{s}_i, \qquad s^i = \psi^{-2} \tilde{s}^i. \tag{3.39}$$

We can then define an extrinsic curvature of the two-surface embedded in the three-space:

$$H_{ij} \equiv h_i^k h_j^l \nabla_{(k} s_{l)} = \frac{1}{2} h_i^k h_j^l \mathcal{L}_s h_{kl}. \tag{3.40}$$

Now let us define the outgoing null rays $k^\mu \equiv \frac{1}{\sqrt{2}}(n^\mu + s^\mu)$ and ingoing null rays $k'^\mu \equiv \frac{1}{\sqrt{2}}(n^\mu - s^\mu)$. From which, we create two sets of fully four-dimensional extrinsic curvatures. One is associated with the outgoing null rays $\Sigma_{\mu\nu} \equiv \frac{1}{2} h_\mu^\alpha h_\nu^\beta \mathcal{L}_k g_{\alpha\beta}$ and the second is associated with the ingoing null rays $\Sigma'_{\mu\nu} \equiv \frac{1}{2} h_\mu^\alpha h_\nu^\beta \mathcal{L}_{k'} g_{\alpha\beta}$. The first will be used in finding the expansion and shear of outgoing null rays, which we need for applying the quasiequilibrium

boundary conditions. Let us also define the following projections of K_{ij}:

$$\begin{aligned} J_{ij} &\equiv h_i^k h_j^l K_{kl}, \\ J_i &\equiv h_i^k s^l K_{kl}, \\ J &\equiv h^{ij} J_{ij} = h^{ij} K_{ij}. \end{aligned} \tag{3.41}$$

With these projections, we greatly simply the two extrinsic curvatures defined in terms of ingoing and outgoing null rays:

$$\Sigma_{ij} = -\frac{1}{\sqrt{2}}(J_{ij} - H_{ij}) \tag{3.42}$$

and

$$\Sigma'_{ij} = -\frac{1}{\sqrt{2}}(J_{ij} + H_{ij}). \tag{3.43}$$

One can then get the expansions of null rays (outgoing and ingoing respectively):

$$\begin{aligned} \theta = h^{ij}\Sigma_{ij} &= -\frac{1}{\sqrt{2}}(J - H), \\ \theta' = h^{ij}\Sigma'_{ij} &= -\frac{1}{\sqrt{2}}(J + H). \end{aligned} \tag{3.44}$$

One can also define the shears:

$$\begin{aligned} \sigma_{ij} &\equiv \Sigma_{ij} - \frac{1}{2} h_{ij}\theta, \\ \sigma'_{ij} &\equiv \Sigma'_{ij} - \frac{1}{2} h_{ij}\theta'. \end{aligned} \tag{3.45}$$

Just having the expansion and shear of the outgoing null-rays (θ and σ_{ij}) provides enough of an understanding of the geometric properties of the excision to apply the quasi-equilibrium boundary conditions. This is the next step.

Recall the time vector is written $t^\mu = \alpha n^\mu + \beta^\mu$. Requiring the apparent horizon to not move with respects to the coordinates means the coordinates must track this null surface (the apparent horizon):

$$t^\mu k_\mu|_S = 0. \tag{3.46}$$

By inserting the definitions of these vectors, one can show

$$\alpha|_S = \beta^i s_i|_S. \tag{3.47}$$

At this point it will be useful to define the shift in terms of its part parallel to the surface, $\beta_\parallel \equiv h^i_j \beta^j$, and its part perpendicular to the surface, $\beta_\perp \equiv \beta^i s_i$. We rewrite our previous result as

$$\alpha|_S = \beta_\perp|_S. \tag{3.48}$$

This provides both a boundary condition on the part of the shift perpendicular to the excision surface and will be used to simplify further conditions. Here I will write out the shear of the outgoing null rays using the definition of K_{ij} in Eqs. (3.17), (3.22), and (3.23) and the definition of Σ_{ij} found in Eq. (3.42):

$$\begin{aligned} \sigma^{ij} &= \frac{1}{\sqrt{2}}\left(H^{ij} - \frac{1}{2}h^{ij}H\right)\left(1 - \frac{\beta_\perp}{\alpha}\right) \\ &\quad -\frac{1}{\sqrt{2}}\frac{\psi^{-4}}{\alpha}\left[\tilde{D}^{(i}\beta_\parallel^{j)} - \frac{1}{2}\tilde{h}^{ij}\tilde{D}_k\beta^k_\parallel - \frac{1}{2}\left(\tilde{h}^i_k\tilde{h}^j_l\tilde{u}^{kl} - \frac{1}{2}\tilde{h}^{ij}\tilde{h}_{kl}\tilde{u}^{kl}\right)\right]. \end{aligned} \tag{3.49}$$

Here, $\tilde{D}_i$ is the covariant derivative compatible with the conformal two-metric induced on the excision surface $\tilde{h}_{ij}$. By setting all the components of the shear to zero on the apparent horizon and recalling the value of the perpendicular part of the shift, one can simplify Eq. (3.49) to

$$\left[\tilde{D}^{(i}\beta_\parallel^{j)} - \frac{1}{2}\tilde{h}_{ij}\tilde{D}_k\beta^k_\parallel - \frac{1}{2}\left(\tilde{h}^i_k\tilde{h}^j_l\tilde{u}^{kl} - \frac{1}{2}\tilde{h}^{ij}\tilde{h}_{kl}\tilde{u}^{kl}\right)\right]_S = 0. \tag{3.50}$$

One can then treat the time derivative of the conformal metric $\tilde{u}^{ij}$ as a source function for the parallel part of the shift on the boundary. Consistent with the idea of quasiequilibrium, it is common practice to set $\tilde{u}^{ij}$ to zero, as we expect little change in the conformal metric in a system approximating equilibrium. This simplifies the equation to $\left[\tilde{D}^{(i}\beta_\parallel^{j)} - \frac{1}{2}\tilde{h}_{ij}\tilde{D}_k\beta^k_\parallel\right]_S = 0$, which implies that the parallel components of the shift on the horizon, which are associated with the black hole's spin, must be proportional to a conformal Killing vector. This enables one to simply define the shift parallel to the boundary

with an arbitrary parameter Ω_r that determines the rotation on the horizon:

$$\beta_{\parallel} = \Omega_r \xi^i. \tag{3.51}$$

Here ξ^i, which is a conformal Killing vector of the excision surface, determines the orientation of the spin. The actual choice of Ω_r and ξ^i is reserved for a discussion of the physics one desires to model.

Still, we have not taken advantage of the expansion of the outgoing null rays. Rewriting θ in terms of conformally-weighted quantities yields

$$\theta = \frac{\psi^{-2}}{\sqrt{2}}(\tilde{h}^{ij}\tilde{\nabla}_i \tilde{s}_j + 4\tilde{s}^k \tilde{\nabla}_k \ln\psi - \psi^2 J). \tag{3.52}$$

Taking the expansion to be zero, we find

$$\tilde{s}^k \tilde{\nabla}_k \ln\psi|_S = -\frac{1}{4}(\tilde{h}^{ij}\tilde{\nabla}_i \tilde{s}_j - \psi^2 J)|_S. \tag{3.53}$$

This derivative condition on the conformal factor can be directly applied on the excision boundary to ensure it is a MOTS, or an apparent horizon. Taken together, Eqs. (3.47), (3.51), and (3.53) provide a complete set of quasi-equilibrium excision boundary conditions for the conformal factor ψ and the shift β^i. As described in [33], it was found that arbitrary Dirichlet, Neumann or Robin type conditions on the lapse actually fulfill any quasiequilibrium condition on the lapse and allow for a solvable boundary-value problem.

The extended conformal thin-sandwich equations, so long as the conformal metric is specified to be positive-definite, poses a set of five coupled elliptic operators to determine the values for the following primary variables: the conformal factor ψ, the conformal lapse $\tilde{\alpha}$ and the shift β^i. The excision boundary conditions and the outer boundary conditions presented here complete the task of making a well-posed boundary-value problem when one chooses to excise the black holes from the domain of calculation. They leave choices for $\mathbf{\Omega}_0$ on the outer boundary and for Ω_r and ξ^i on each excision which parametrizes the spin magnitude and direction respectively. Still left is the choice of the freely specifiable data over the whole domain: the trace of the extrinsic curvature K and its time derivative $\partial_t K$,

and the conformal metric $\tilde{\gamma}_{ij}$ and its time derivative $\tilde{u}_{ij} = \partial_t \tilde{\gamma}_{ij}$. The next chapter will delve into the particular physics of the binary black-hole problem: both what physics are desired and what measurements we have to use in finding the desired physics.

Chapter 4

The physics of binary black holes

A central goal of studying the binary black-hole (BBH) problem is to develop theoretical templates for some of the gravitational waves that may soon be detected by either LIGO or LISA. To that end, BBH initial data needs to be made to accurately model astrophysically likely scenarios. For BBH's, LIGO, in particular, will likely be able to detect gravitational waves emitted by BBH's only for a short time-frame before and after merger. A post-Newtonian study [60] has shown that radiation tends to circularize the motion long before this coalescence. From this study, one can conclude that binary black holes should be modeled in an adiabatic inspiral, where the radial motion is small compared to the period of the orbit until the black holes get quite close. This is often called a quasicircular orbit because gravitational radiation does not allow for truly circular orbits. We can neither directly measure the radial motion nor the period of orbit using just initial data, so instead, most researchers have worked on methods that predict these quasicircular orbits using other measures.

Two such methods, based on different applications of physical measurements, have been commonly used for the binary black-hole problem. One is the effective-potential (EP) method [28], where quasi-circular orbits are predicted by minimizing a binding energy. The other is based on the Komar-mass ansatz [43], which compares two definitions of total energy to find quasicircular orbits. It should be noted that not all initial-data formulations

require these methods for finding quasicircular orbits. Methods that allow for the direct specification of the linear momenta of the black holes such as [32, 18] can determine those values from post-Newtonian results [20, 35] as well. This chapter will discuss what physical quantities can be defined using only initial data. We will then discuss the effective potential method and the Komar-mass ansatz in more detail before concluding with some finishing remarks.

4.1 Physical measurements

In the context of the ADM decomposition, if a given hyper-surface Σ in the foliation of the space-time $\{\Sigma\}$, is asymptotically flat, one can apply rigorous definitions of energy and momentum (both linear and angular) to that hyper-surface. The ADM energy is

$$E_{\mathrm{ADM}} = \frac{1}{16\pi} \oint_{\infty} \nabla_j \left(\mathcal{G}_i^j - \delta_i^j \mathcal{G} \right) d^2 S^i, \tag{4.1}$$

and the ADM angular momentum is

$$J_{(\xi)} = \frac{1}{8\pi} \oint_{\infty} \left(K_{ij} - \gamma_{ij} K \right) \xi^j \, d^2 S^i, \tag{4.2}$$

where $\mathcal{G}_{ij} \equiv \gamma_{ij} - f_{ij}$, f_{ij} is the flat metric, and ∇_j is the covariant derivative compatible with γ_{ij}. In Eq. (4.2), ξ^i is a rotational Killing vector of the spatial slice. This is for an asymptotically flat space-time, and the integral is performed at infinity, so the ξ^i's can be taken to be the flat-space rotational Killing vectors. This can allow the measurement of total angular momentum in three directions. It should be noted that Eq. (4.2) would measure the linear momentum if ξ^i were taken as a translational Killing vector.

The Komar mass is a rigorous definition of total mass so long as the geometry is stationary, meaning that the geometry possesses a time-like Killing vector:

$$M_{\mathrm{K}} = \frac{1}{4\pi} \oint_{\infty} \left(\nabla_i \alpha - \beta^j K_{ij} \right) d^2 S^i. \tag{4.3}$$

An arbitrary binary configuration is not necessarily stationary, so this definition cannot

be taken to represent the total mass of the system. However, it will be applied in the Komar-mass ansatz to identify quasi-stationary orbits.

While the definitions provided so far allow for the measurement of global quantities, similar definitions cannot be given rigorously when attempting to measure say the mass of a single black hole in a binary system. When studying initial data for binary black holes, it is impossible to make such a measurement at infinity. However, we can make use of quasi-local definitions which are often integrated over some closed two-surface in the spatial slice. The mass and spin of the individual black holes would provide very useful ways to characterize BBH initial data.

Christodoulou [24] provides a relation (the Christodoulou formula) between the total mass of a Kerr black hole and its irreducible mass and spin:

$$M^2 = M_{\text{irr}}^2 + \frac{S^2}{4M_{\text{irr}}^2}. \tag{4.4}$$

The irreducible mass is defined in terms of the surface area of the event horizon A_{EH}:

$$M_{\text{irr}} = \sqrt{\frac{A_{EH}}{16\pi}}. \tag{4.5}$$

Applying these results to BBH initial data requires we do these things: decide whether and how these results for a Kerr black hole apply to a binary system, identify an event horizon, and find a way to measure spin. Under the assumption of quasiequilibrium, one would expect the distortion of the geometry around one black hole due to the other to be small. Thus we would expect the Christodoulou formula to apply. We would also expect the definition of the irreducible mass to be meaningful. Unfortunately, we are unable to identify the event horizon in initial data.

We have already defined in the excision boundary conditions the existence and position of a the apparent horizon of each black hole. In stationary systems such as a Kerr black hole, the apparent and event horizons coincide. Again, applying quasiequilibrium, in the case of binary black holes, the distortion from where the two horizons coincide should be

small. Thus we apply a new definition of the irreducible mass by making use of the surface area of apparent horizon A_{AH}:

$$M_{\rm irr} = \sqrt{\frac{A_{AH}}{16\pi}}. \tag{4.6}$$

We now have the apparent horizon mass (4.6) and, if the spin of an individual black hole is defined, we are able to use the Christodoulou formula (4.4) to estimate a black hole's total mass. There exist many quasi-local definitions of spin [69] which are motivated in different ways. A quasi-local definition derived originally by Brown and York [19] and later re-derived for isolated and dynamical horizons by Ashtekar and Krishnan [4, 5] provides such an approximation:

$$S_{(\xi)} = \frac{1}{8\pi} \oint_{\mathcal{S}} (K_{ij} - \gamma_{ij} K)\, \xi^j \, d^2 S^i. \tag{4.7}$$

Here ξ^i is a Killing vector of the metric induced on the excision surface h_{ij}, and $\mathcal{S}$ is the excision surface. In terms of conformal variables, this can be rewritten as

$$S_{(\xi)} = \frac{1}{16\pi} \oint_{\mathcal{S}} \frac{1}{\tilde{\alpha}} \left[(\tilde{L}\beta)_{ij} - \tilde{u}_{ij} \right] \xi^j \tilde{s}^i \sqrt{\tilde{h}}\, d^2 x. \tag{4.8}$$

In general, however, there is not a Killing vector available on the horizon. An additional advantage to taking the conformal geometry to be flat, and requiring the excision surface to be a sphere in that flat conformal geometry, is that we can approximate a Killing vector ξ^i using the conformal rotational Killing vectors:

$$\xi^i_{(x)} = x^j_S \epsilon^{ixj}, \tag{4.9a}$$

$$\xi^i_{(y)} = x^j_S \epsilon^{iyj}, \tag{4.9b}$$

$$\xi^i_{(z)} = x^j_S \epsilon^{izj}. \tag{4.9c}$$

Here I have assumed Cartesian coordinates, and $\mathbf{x}_S$ is measured relative to the center of the excision sphere.

Since these are, at best, only approximations of Killing vectors, one should have an alternate method for comparison. Dreyer *et al.* [38] have provided an alternate method

that attempts to solve the Killing equation. This method effectively transforms the Killing equation into a set of *Killing Transport Equations* that are then solved on a closed two-surface to find something approximating a Killing vector. Details of the method are given in Dreyer, and the particular implementation that has been used in our work along with comparisons between definitions (implemented by others than myself) is provided in [22]. I will use the following to denote the spins calculated using the flat-space Killing vectors and the spins calculated using the Killing Transport Equations respectively:

$$\begin{array}{rcl} S_x & : & \text{computed using Eq. (4.9a),} \\ S_y & : & \text{computed using Eq. (4.9b),} \\ S_z & : & \text{computed using Eq. (4.9c),} \\ S_K & : & \left\{ \begin{array}{l} \text{computed using an approximate} \\ \text{solution of Killing's equation.} \end{array} \right. \end{array} \tag{4.10}$$

The goal of this chapter is to show how to find initial data accurately modelling the expected quasicircular orbits. The definitions here provide the basic tools neccesary for this task. Next I will describe the two methods I have used to do so: the effective potential method, and the Komar-mass ansatz.

4.2 Effective Potentials

In the Newtonian effective one-body problem, an effective potential (EP) can nicely capture the necessary information to fully define orbits. For a classical non-radiative reducible two-body problem, by keeping orbital angular momentum constant, an EP can be used to find the turning points of an orbit with a given energy or the energy and separation of a circular orbit. For relativistic binaries, the creation of gravitational waves, and other phenomena such as the precession of orbits means that an effective potential can, at best, be only an approximation, where it is assumed that dissipative effects occur on a time frame much larger than the period of orbit. This assumption fails at smaller separations.

For numerical relativity, an effective-potential method was originally developed and used [28] to predict circular orbits with the conformal imaging approach(the conformal imaging approach is detailed in [76, 14, 16, 15, 51, 27]) for constructing black-hole initial

data. It was later used with puncture methods [10] and eventually with the extended conformal thin-sandwish decomposition [33]. It has also been used with a puncture/conformal thin-sandwich hybrid method [47] to predict quasicircular orbits [46] and found agreement with [33].

For the purposes of this work, I will define an effective potential as a binding energy measured in a system while varying some general coordinate and keeping other quantities held constant. Further, I will require the time-derivative of that general coordinate to be held to zero to ensure we are taking data at turning-points in the effective potential. In the case of binary black holes, the varied coordinate is radial separation. Black-hole irreducible masses, black-hole spins and orbital angular momentum are to be held constant. The radial velocity is to be zero. Lastly, any changes due to radiation must be small over the period of an orbit. If these conditions are all true, at least to a good approximation, the effective potential can be used to find initial data at turning points and also provide a good method for finding quasicircular orbits at a minimum of binding energy.

In practical terms, this ideal definition can be difficult to attain in initial data. For one, so far, we have no definition of a binding energy E_b so one needs to be provided:

$$E_b \equiv E_{\rm ADM} - m. \tag{4.11}$$

The m in this equation represents the sum of the individual total masses of the black holes:

$$m = m_1 + m_2. \tag{4.12}$$

Here m_1 and m_2 are found using the Christodoulou formula. This immediately allows for error. The irreducible mass (4.6) is measured as the apparent-horizon mass under the assumption that the event horizon is at least close to coincident with the apparent horizon. Another difficulty is that the quasi-local definition of spin in use (4.8) assumes the presence of a Killing vector on the surface. At best we only have an approximate Killing vector. The apparent-horizon mass, the Christodoulou formula and the Killing-vector approximations

all become less reliable as the separation between the black holes decreases. Further, in the extended conformal thin-sandwich decomposition with excision, there is no way to explicitly set the radial velocity to zero, though we believe choices in the free data and boundary conditions will lead to zero radial velocity. Still, under the assumption of quasiequilibrium, the definitions used in creating effective potentals should be a good approximation.

4.3 The Komar-mass ansatz

While effective potentials can provide useful information about a variety of configurations, they are computationally expensive to produce and create a lot of data sets that are not in quasicircular orbit. The Komar-mass ansatz [43] provides an alternative method for locating quasicircular orbits directly. One can describe a circular Keplerian orbit as a stationary system. In relativity, we can only expect quasicircular orbits because the existence of dissipative radiation does not allow for truly stationary systems. This means that the Komar mass (4.3) is not generally robust for a binary black-hole system. However, the ADM energy (4.1) is robust, as the system is modeled as asymptotically flat. While, admittedly, no stationary solution exists for binary black holes, the Komar-mass ansatz suggests that since the Komar mass is valid for stationary systems, if the Komar mass were measured, and was found to be equal to the ADM energy, the system would be in quasistationary orbit. Then if stationary systems imply circular orbits for non-radiative binaries, quasiequilibrium would imply quasicircular orbits for radiative binaries. A stronger mathematical justification for the ansatz is provided in [43], but is beyond the scope of this work.

Physical quantities derived from numerical results for black-hole binaries found using the Komar-mass ansatz have been compared to post-Newtonian (PN) predictions of circular orbits, suggesting good agreement [33, 34]. Further, arguments have been developed (see [43, 40]) to show that a system in quasiequilibrium must satisfy the Komar-mass ansatz, though this does not necessarily mean satisfying the Komar-mass ansatz implies quasiequilibrium. For the purposes of this work, it will be useful to define a Komar-mass difference ΔM_{K} as

the difference between the ADM energy and Komar mass:

$$\Delta M_{\rm K} \equiv M_{\rm K} - E_{\rm ADM}. \tag{4.13}$$

Thus finding initial data in which $\Delta M_{\rm K} = 0$ is equivalent to satisfying the Komar-mass ansatz.

4.4 Discussion

This chapter has focused on the physics of binary black holes, both in how physical quantities are measured, and how those measurements can be used to find models of astrophysical black-hole pairs. Definitions of total energy and angular momentum have been presented that will hold throughout this work. Definitions of irreducible mass, total mass and spin of individual black holes are all based on approximations (in most cases assuming the system is close to some kind of equilibrium). Measurements of these quantities are necessary for finding the desired conditions for astrophysical binary black holes. Two methods have been described here for finding quasicircular orbits. effective potentials provide a tool for identifying turning points in orbits and circular orbits at a local minimum (or maximum); however, the application of the definition of an effective potential is suspect both for uncertainties in the measurement of physical quantities and a lingering uncertainty about the radial motion. The Komar-mass ansatz provides an alternative, but unproven, method for identifying circular orbits. It does compare well with post-Newtonian results, and as I will argue later, the Komar-mass difference is useful for parametrizing the eccentricity of binary black-hole orbits.

Chapter 5

Computational Tools

A great deal of my work as a graduate student has been done using a numerical code called Eric. Eric is a pseudo-spectral solver designed to solve sets of elliptic equations (methods described in [62]) and we apply it to the study of binary black-hole initial data. While many conformal decompositions have been implemented in Eric, I used the code in conjunction with the ECTS equations with excision. The code has many levels of operation, including: a core which solves equations numerically given a set of parameters, a domain creating device which defines the space the equations are being solved on, a mechanism to iteratively improve resolution, and sequencers developed to find initial data that conforms to ideas of the Komar-mass ansatz or effective potentials. This chapter will first discuss the parameters, domain choices and freely specifiable data. This will be followed by discussions of the core solver, the domain creating device, and the sequencers.

5.1 Parameters and freely specifiable data of the ECTS equations with excision

The ECTS equations allow for the free specification of four objects: the trace of the extrinsic curvature K, its time-derivative $\partial_t K$, the conformal metric $\tilde{\gamma}_{ij}$, and its time-derivative $\tilde{u}_{ij} \equiv \partial_t \tilde{\gamma}_{ij}$. The solution domain must be specified along with the size, shape and locations of the black-hole excision surfaces. Before the initial data can be determined, the parameters Ω_r and ξ^i on the excision surfaces (Eq. (3.51)) and $\mathbf{\Omega}_0$ on the outer boundary (Eq. (3.33))

must be defined. Ω_r and ξ^i parametrize the magnitude and direction of the spin of individual black holes, while $\mathbf{\Omega}_0$ parametrizes the orbital motion of the black holes. In order to find a unique solution to the ECTS equations, all these parameters, choices for the domain and the freely specified data must not only be defined, but must also be defined in a way that still yields a well-posed boundary-value problem.

The easiest freely specifiable data to handle is the trace of the extrinsic curvature K and its time-derivative $\partial_t K$. This is because the trace of the extrinsic curvature is taken to be a gauge choice. A very simplifying choice is that of maximal slicing, or setting $K = 0$. This has the benefit of simplifying the resultant equations. As K is a gauge choice, setting $\partial_t K$ is making a choice about how the gauge can change. Again, to simplify the equations, we take $\partial_t K = 0$. This choice is also consistent with the notion of quasiequilibrium.

Specifying the conformal metric and its time-derivative has physical consequences. The full spatial metric is a second-rank three-dimensional symmetric tensor and thus has six degrees of freedom. When conformally decomposed, it has been shown that the conformal factor can be conveniently taken as a constrained degree of freedom. The remaining five degrees of freedom are contained in the conformal metric. Of those five, two are the dynamical degrees of freedom and three are gauge degrees of freedom. Thus specifying the conformal metric both determines the initial spatial gauge of the initial data and has an impact on the gravitational wave content of the ID. The simplest choice is conformal flatness, or setting the conformal metric equal to the flat metric ($\tilde{\gamma}_{ij} = f_{ij}$). As the flat metric is positive definite, this choice has the advantage of insuring the ECTS equations are elliptic. It is also known to be a source of error in calculation. It has been shown that the Kerr solution for a single spinning black hole is not conformally flat [41] . Further, we know from post-Newtonian results [65] that binary systems are not conformally flat. The result of using conformal flatness, which has been seen in many numerical evolutions [17, 54] of initial data, is the existence of undesired "junk radiation" in the initial conditions. Still, for capturing the dominant physics of binary black holes, conformal flatness is very effective

and the problems it presents are relatively minor.

Setting the time derivative of the conformal metric has consequences on the initial movement of the black holes. Again with the notion of quasiequilibrium, we set $\tilde{u}_{ij}$ to zero everywhere. This implies that the conformal geometry is, at least temporarily, stationary with respects to the time vector t^μ. While the outer boundary condition, Eq. (3.33), on the shift has the coordinates follow the rotation of the system, we believe setting the time derivative of the spatial metric to zero effectively sets the radial motion to zero.

This now leaves the choices for the domain and boundary conditions. Let's start by choosing the size and shape of the excision surfaces for each black hole. We set the shape to be that of a coordinate sphere in the domain. This limits any discussion of the size of the excisions to one of radius. The size of the black holes is parameterized by the radii of the excision surfaces, r_1 and r_2. The coordinate separation of the black holes then parametrizes separation of the two black holes.

Next let's examine the outer boundary conditions. Eq. (3.33) requires the specification of a vector quantity $\mathbf{\Omega}_0$ which parametrizes the system's rotation. We are completely free to pick the orientation of $\mathbf{\Omega}_0$. We set its direction along the z-axis leaving only the magnitude of rotation, Ω_0, to be chosen.

Lastly we have to deal with the parameters Ω_r and ξ^i on the excision boundary. ξ^i is a conformal Killing vector determining the direction of the spin. To simplify the physics to be studied, we will choose the spins to be in the same direction as the system's rotation. This means that for either black hole we set $\xi^i = (\hat{z} \times \hat{r})^i$ where $\hat{r}$ is measured from the center of the excision in question. Thus we are left with Ω_{r1} and Ω_{r2} applied to the excisions parameterizing their spin magnitudes. By setting $r_1 = r_2 = r$, and $\Omega_{r1} = \Omega_{r2} = \Omega_r$, we effectively set the spins, and masses of the black holes equal to each other. Note that setting just the radii equal does not mean equal mass, as the spin contributes to the mass, and setting just the Ω_r's equal does not mean equal spin, as the mass contributes to the spin.

With the freely specifiable data chosen and these simplifications on the parameters, the remaining parameters to manipulate are the coordinate separation of the black holes, Ω_0 defined on the outer boundary and parameterizing the rotation of the system, and the parameter on the excisions, Ω_r. While Eric was written to handle other possible choices (such as unequal-mass black holes) for initial data, all the work here is concerned with these limiting cases.

5.2 The core solver of Eric

To describe the numerical code Eric, I will first present the fundamentals of the numerical solver and discuss what choices of freely specifiable data and parameters are handled in the core solver. The core of the code is a pseudo-spectral solver which treats the solution to the ECTS equations as a truncated sum of known functions with their respective coefficients:

$$\mathbf{f}(\mathbf{x}) = \sum_{i=1}^{i=n} c_i \mathbf{f}_i(\mathbf{x}). \tag{5.1}$$

Here $\mathbf{f}(\mathbf{x})$ represents a solution over the domain, $\mathbf{x}$ is the position in the domain of computation, $\mathbf{f}_i(\mathbf{x})$ are a truncated series of functions and c_i are coefficients corresponding to those functions. One can then completely define a solution by the set of coefficients $\{c_i\}$. For every function $\mathbf{f}_i(\mathbf{x})$ in the truncated series, the domain of computation must contain a collocation point $\mathbf{x}_i$, where the constraints are to be analyzed. This means the set of collocation points $\{\mathbf{x}_i\}$ has the same number of elements as the set of functions $\{\mathbf{f}_i(\mathbf{x})\}$. In practice, when a domain is created for computation, the total number of collation points is determined and the series of functions is truncated to the same number. In this scheme, one defines the resolution of the computation by counting the number of elements in $\{\mathbf{x}_i\}$.

This takes the problem of finding a solution to the ECTS equations and fashions it as an algebraic inversion problem:

$$\mathbf{A}(\mathbf{q}) = \mathbf{b}. \tag{5.2}$$

In this representation, the elements of the vector $\mathbf{q}$ are the coefficients $\{c_i\}$. $\mathbf{A}$ is an operator

defined by the ECTS equations (the constraints on the variables ψ, β^i and $\tilde{\alpha}$). The resultant vector $\mathbf{b}$ is the residual which Eric seeks to eliminate. If Eric finds a $\mathbf{q}$ that when acted on by $\mathbf{A}$ results in $\mathbf{b} = 0$, the ECTS equations have been fulfilled. It should be noted that the vector $\mathbf{q}$ (or, equivalently, the set of coefficients $\{c_i\}$) cover all the variables being solved for, not just one. The advantage of this inversion view of the problem is that there exists a computational library called PETSc [8, 9, 7] developed to handle large scale algebraic inversion efficiently.

PETSc stands for Portable, Extensible Toolkit for Scientific Computation. It is designed to work on parallel or serial computer systems to solve both linear and nonlinear partial differential equations numerically, and it is designed to interface with Fortran, C, and C++ codes. The code makes use of the BLAS, LAPACK and MPI libraries. The ECTS equations are nonlinear, and so PETSc was chosen because it has a nonlinear solver: the SNES library.

SNES essentially makes steps by employing Newton's Method:

$$\mathbf{q}_{k+1} = \mathbf{q}_k - [\mathbf{A}'(\mathbf{q}_k)]^{-1} \cdot \mathbf{A}(\mathbf{q}_k), \quad k = 0, 1, 2... \tag{5.3}$$

Here $\mathbf{q}_0$ is an initial guess at a solution and $\mathbf{A}'$ is the Jacobian of $\mathbf{A}$. In practice, there is a two step method:

$$1. \qquad \text{Approximately solve} \quad [\mathbf{A}'(\mathbf{q}_k)] \cdot \Delta\mathbf{q}_k = -\mathbf{A}(\mathbf{q}_k) \tag{5.4}$$

$$2. \qquad \text{update} \quad \mathbf{q}_{k+1} = \mathbf{q}_k + \Delta\mathbf{q}_k \tag{5.5}$$

Step one is handled through a linear solver for the linearized $\mathbf{A}'$. Our particular implementation uses a Krylov subspace method for the linear solver, and preconditioning is used to speed up the linear solver (typically a preconditioner of a Laplacian for the domain and an identity operator for the boundaries). While Newton's method is not guaranteed to work for nonlinear sets of equations, we have found the method works well with finding solutions to the ECTS equations given a reasonable choice for an initial guess.

PETSc requires the researcher to implement code that numerically calculates $\mathbf{A}(\mathbf{q})$ and $[\mathbf{A}'(\mathbf{q}_k)] \cdot \Delta\mathbf{q}_k$ and the same for the boundary conditions. It also needs an initial guess $\mathbf{q}_0$ along with a number of parameters for various termination criteria. $\mathbf{A}(\mathbf{q})$ and $[\mathbf{A}'(\mathbf{q}_k)] \cdot \Delta\mathbf{q}_k$ are hard coded in the core solver of Eric (along with boundary conditions) as the ECTS equations and their linearized form. The core solver is provided a domain for calculation including the boundaries and location of all collocation points $\{\mathbf{x}_i\}$. It is also provided the set of basis functions $\{\mathbf{f}_i(\mathbf{x})\}$, the parameters Ω_r and Ω_0 and an initial guess for the variables ψ, $\tilde{\alpha}$ and β^i. The solver then uses PETSc to search for a solution for ψ, $\tilde{\alpha}$ and β^i fitting the domain and parameters making use of the hard-coded ECTS equations and quasiequilibrium boundary conditions.

5.3 Domain choice

For the definitions of $\mathbf{A}(\mathbf{q})$ and $[\mathbf{A}'(\mathbf{q}_k)] \cdot \Delta\mathbf{q}_k$ to have any meaning, there needs to be a domain, possibly broken into subdomains, with a set of collocation points over that domain. For the equal-mass binaries we calculate, Eric posseses an automated domain design. The setup of subdomains and the boundaries between subdomains along with the placement of colocation points (which all is handled in Eric's domain builder) is beyond the scope of this work. Of primary concern is the placement of the excision surfaces and the treatment of the overall resolution.

While Eric could handle other possibilities, this work is concerned with equal-mass black holes, and thus it is most sensible to set the coordinate origin at the center of the computational domain and place the excisions equal-distant from the origin along some axis. In other words, with consideration to some flat background metric, the black holes are placed at $d/2$ and $-d/2$ along the x-axis (being perpendicular to the z-axis). The excisions are made in the domain builder to the set value r. Thus coordinate separation and the radii of the excisions is handled entirely by the creation of the computational domain.

Recall that numerical resolution for a spectral scheme is found in the number of collocation points in the computational domain. To achieve higher resolution, one simply increases the number of collocation points (and thus basis functions). Eric is designed, however, to achieve higher resolutions even faster by using a multistep solving process. It defines levels of resolution. Level 0 corresponds to a base number of collocation points. Level 1 has more collocation points. Level 2 has even more points. In calculating a higher level of resolution, Eric will first run a calculation at level 0 resolution. It will then run at level 1 resolution using the results from the level 0 run as an initial guess for the current run. This process continues until the desired resolution is achieved.

5.4 Applying EP and Komar methods in Eric

The domain designer and the core solver of Eric thus have the capability to achieve high resolution solutions to the ECTS equations with excision for equal-mass and equal-spin binary black holes given the specification of the three parameters d, Ω_r and Ω_0. While the radii, r, needs to be chosen, this can effectively be treated as a scale factor. When this is done, the ADM energy, total angular momentum, Komar mass, black-hole irreducible masses, black-hole spins and black-hole total mass (as per the Christodoulou formula) are available as per the definitions in Chapter 4. All that is left then is to create effective potentials and initial data satisfying the Komar-mass ansatz. To do this, Eric is equipped with sequencers designed for each job. In practice this is done with either root-finding or minimization.

A root finder or minimizer generally needs a function which is given a set of input parameters and outputs a set of measurements that one desires to find either roots or minima of. The dimension of the function is the number of parameters to be adjusted. It is important that for every parameter to be adjusted, there is a condition to be met. For instance, if one wanted to make an effective potential at a given angular momentum J_0 with a given spin magnitude S_0 (still assuming equal spins in the direction of the system's

rotation), that would have two measurable quantities to find roots in. The conditions would be

$$S - S_0 = 0$$

$$J - J_0 = 0.$$

The input parameters would be Ω_0 and Ω_r. The effective potential sequencer would then create a series of initial-data sets at different separations from d_0 to d_1. At each separation the root-finder would be used to adjust Ω_0 and Ω_r to find the correct spin and angular momentum. Numerical Recipes [63] describes many kinds of root-finders and minimization techniques in one dimension or multiple dimensions with different advantages and disadvantages. I personally implemented Broyden's method, described in Numerical Recipes, so we could run searches in multiple dimensions.

Chapter 6

Testing methods for finding quasicircular orbits and testing notions of spin

The Komar-mass ansatz and the effective-potential method provide two independent ways to create binary black-hole initial data in quasi-circular orbits. To fully test these methods, they should be compared both against each other and against an independent measure. Two choices of spin are often used as limiting cases: the nonspinning case and the corotating case. Corotation implies that the black-holes spin synchronously with the orbit. An analog of this could be seen in how the moon always rotates along its orbit so that the same side of the moon always faces the Earth. Not an astrophysically likely condition, corotation is still studied because there is a clear notion of how to create corotating data: simply setting $\Omega_r = 0$. The nonspinning case, while equally astrophysically unlikely, is studied because there is a clear physical notion of what this means. The measured spin should be zero. Previously, it has been assumed that this is achieved by setting $\Omega_r = \Omega_0$ [33]. Doing this was thought to effectively "un-spin" the black holes. In this chapter, I will present how our measures of spin for initial data disagree with that hypothesis and describe the way we found to construct initial data with zero measured spin.

This chapter will also discuss two tests of the methods for finding quasicircular orbits. First, the two methods can be compared directly. The minima of a set of effective potentials

would be expected to compare well with data conforming to the Komar-mass ansatz. We find this to hold for corotating data. For nonspinning data, when simply assuming $\Omega_r = \Omega_0$ implies $S = 0$, the two methods are found to disagree. When initial data is chosen so that measures of spin are zero, the effective-potential method and the Komar-mass ansatz are found to agree well on quasicircular orbits. The other test of these methods will be applied directly to Komar data. In the corotating case, there is a thermodynamic identity that can be applied. We found that not only does the corotating initial data that fulfills the Komar-mass ansatz agree with the thermodynamic identity, but so does nonspinning data found with our new nonspinning method. This work was originally presented in [22].

6.1 Comparing effective potentials to Komar-mass ansatz data

Before delving into results, it is helpful to explain what kinds of data will be compared. A Komar sequence is a series of initial data taken over a range of separations that conform to the Komar-mass ansatz. This is done using root finding. At each coordinate separation, a root-finder adjusts Ω_0 until the initial data returned has zero Komar-mass difference $\Delta M_{\rm K} = 0$. In the corotating case, Ω_r is always taken to equal zero, and with the original hypothesis of nonspinning initial data, Ω_r is taken equal to Ω_0. Thus both cases can be handled with one-dimensional root finding. When finding data that measures zero spin, Ω_r is taken to be equal to $f_r\Omega_0$, and f_r is another parameter in addition to Ω_0. This leads to a two-dimensional root finding algorithm where the other quantity measured is spin. That measured spin is set to zero. Making an effective potential is similar. Instead of measuring $\Delta M_{\rm K}$ and setting that to zero, an effective potential is made by measuring angular momentum and for each separation d picks Ω such that $J - J_0 = 0$. Here J_0 is the desired angular momentum for the effective potential. Again, corotation and the old notion of nonspinning data require only one-dimensional root finding, while the new method of finding nonspinning data requires two-dimensional root finding.

It makes no sense, though, to directly compare an effective potential to a Komar sequence. Rather, one wants to compare the minima of a series of effective potentials to a Komar sequence. To isolate these minima in significant quantity, we make an effective-potential sequence out of the minima of effective potentials. To accomplish this, a series of data is created along some range of values for angular momentum. At each value of the angular momentum, a minimization procedure is called that uses separation as the varied quantity, and binding energy as the minimizable quantity. The function that is to be minimized is then the result of a root-finder which finds data with the correct angular momentum and with the separation specified. The minimization is done one-dimensionally and the root-finding is handled as discussed above depending on the spin condition we wish to employ.

6.1.1 Comparison between methods in the corotating case

The corotating condition ($\Omega_r = 0$) fundamentally breaks a key requirement of creating an effective potential. If the black holes are spinning synchronously, binaries at small separation at a given angular momentum will have higher spins than binaries at large separation. Thus, while the total angular momentum is held constant, neither the orbital nor spin angular momentum is held constant. However, near the minimum of the effective potential, the spins differ only slightly. This means that while a whole sequence does not satisfy the notion of an effective potential, the spins should differ only slightly near the minimum of the effective potential and thus circular orbit predictions should still be valid.

Figure 6.1 shows effective potentials ranging in values of total angular momentum from $J/\mu m = 4.50$ to $J/\mu m = 3.30$ in the thin solid lines. Here, m is the sum of the irreducible masses of the black holes and μ is the reduced mass $\mu = (m_{\mathrm{irr},1} m_{\mathrm{irr},2})/m$. There is a thick line passing through the minima which is the effective-potential sequence. Lastly a dashed line represents the Komar sequence. All the data shown here are corotating and measures the binding energy as a function of proper separation. By examination, the

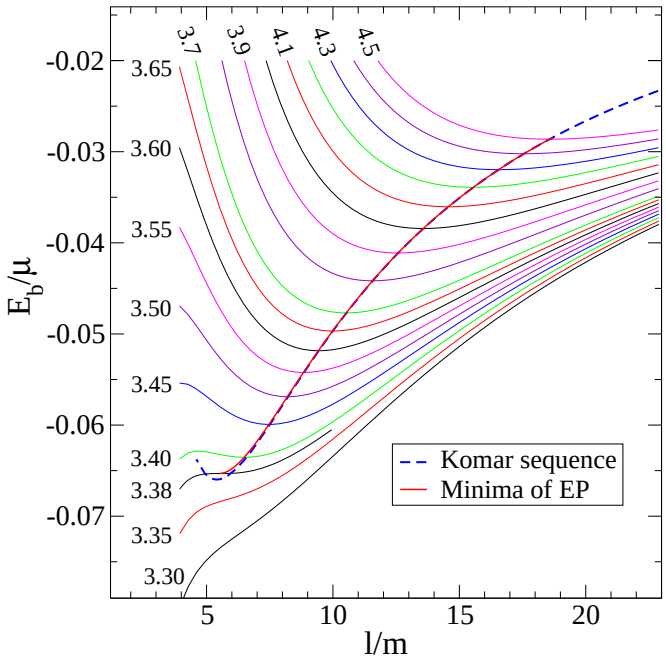

Figure 6.1: effective-potential (EP) curves E_b/μ for corotating black holes vs. separation ℓ/m. These curves are labeled by the orbital angular momentum $J/\mu m$ which is kept constant along each curve. The thick red line connecting the minima of the EP-curves represents circular orbits; it terminates at the the inflection point in the EP-curve at $J/\mu m = 3.38$. Also plotted as a dashed blue line is the sequence of circular orbits determined by the Komar-mass ansatz.

effective-potential sequence and the Komar sequence differ only slightly until very small separations. Qualitatively, the two methods seem to agree.

An interesting feature that can be seen in some of the effective potentials is the existence of a local maximum at smaller separation than the local minimum. If these sequences can be taken as true effective potentials, that would imply the existence of configurations with unstable circular orbits such as for the effective potential of a particle circling a Schwarzschild black hole (see [57] for example). It is noteworthy that the Komar sequence shows an increase in binding energy as the separation decreases below $\ell/m \approx 5$.

Lastly, one can see that as angular momentum decreases, the maximum and minimum in an effective potential occur closer together until the EP at $J/\mu m = 3.38$ where they meet at an inflection point. That inflection point marks the prediction of an innermost stable circular orbit (ISCO). While not a well defined concept in general, if the dissipative effects of radiation could be eliminated, the location of the ISCO, in this case, would represent the onset of secular instability [67, 68]. This inflection point is the ISCO prediction for the effective-potential method. The ISCO for the Komar-sequence is found by locating the lowest energy configuration in the Komar-sequence.

We can examine quantitatively the difference between the Komar-mass ansatz and the effective-potential method by examining the Komar-mass difference $\Delta M_{\rm K}$. Figure 6.2 plots $\Delta M_{\rm K}/E_{\rm ADM}$ for the effective-potential sequence as a function of the unitless $(m\Omega_0)^{5/2}$. The error appears linear in $(m\Omega_0)^{5/2}$, reaching a maximum at the ISCO ($(m\Omega_0)^{5/2} \approx 0.0032$) of $\Delta M_{\rm K}/E_{\rm ADM} \approx 0.017\%$. There is jaggedness at large separation that comes from truncation errors in measuring energy. However the measured Komar-mass difference is clearly physical rather than numerical. While predictions of circular orbits between the Komar-mass ansatz and the effective-potential method do differ, this clearly shows that difference is quite small.

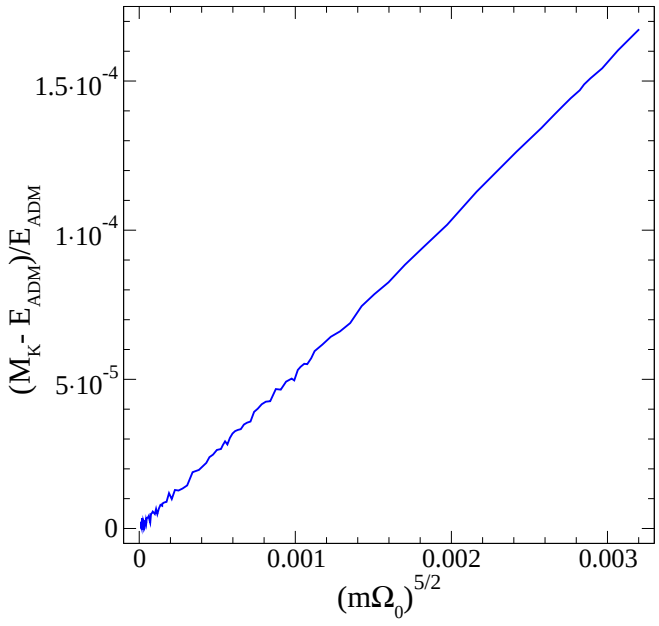

Figure 6.2: Violation of the Komar-mass condition when the effective-potential method is used to determine the sequence of circular orbits. Here, corotating equal-mass binaries are considered. $m\Omega_0$ denotes the orbital angular frequency, so that large separations correspond to small values of $m\Omega_0$.

6.1.2 Comparison between methods in the nonspinning case

As mentioned above, there are two ways we used to create initial data for nonspinning black holes. The first made the assumption that $\Omega_r = \Omega_0$. The second assumed $\Omega_r = f_r\Omega_0$ and the fractional quantity f_r was used as a search parameter.

An examination of the effective-potential lines in Fig. 6.3, where $\Omega_r = \Omega_0$, qualitatively suggests this is not the correct technique to create nonspinning data. In this figure, the effective potentials, the effective-potential sequence and the Komar sequence are plotted in the same manner as Fig. 6.1. The effective potentials themselves do not look like what we might expect. Particularly, there are no inner maximum binding energies, and thus no prediction of an ISCO from the effective potentials. Further, the Komar sequence differs greatly from the effective-potential sequence in this data.

To examine the cause of these results, it helps to examine our quasi-local measures of

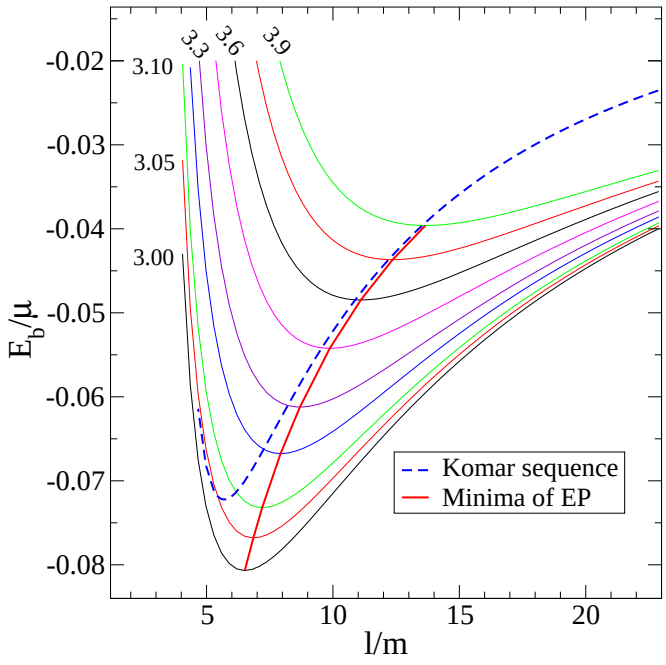

Figure 6.3: EP curves E_b/μ for equal-mass "leading-order" non-spinning binaries ($\Omega_r = \Omega_0$) plotted vs. separation ℓ/m. These curves are labeled by the value of $J/\mu m$ along each curve. Also plotted are the line connecting the minima of the EP-curves, as well as the sequence of circular orbits as determined by the Komar-mass ansatz. The Komar-mass ansatz and the effective-potential method clearly disagree.

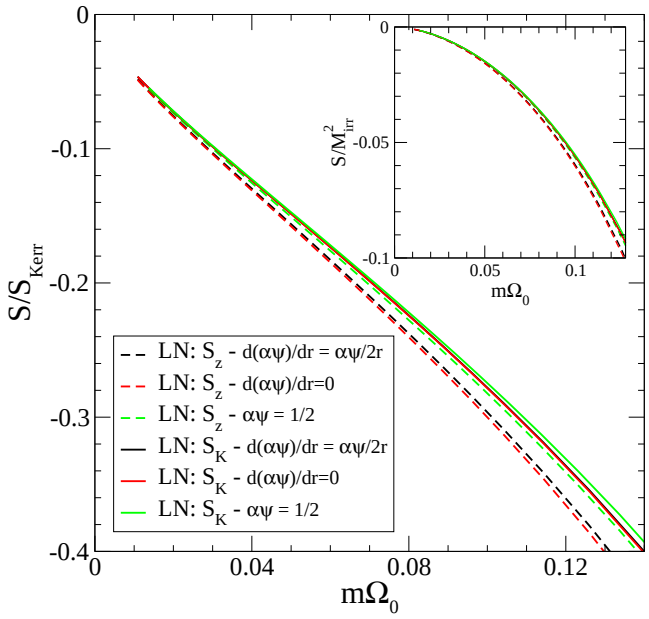

Figure 6.4: Quasi-local spin of the "leading order" non-spinning (LN) binaries (as shown in Fig. 6.3) plotted vs. orbital angular velocity. The inset displays the dimensionless spin value $S/M_{\rm irr}^2$. The main figure displays the magnitude of the spin relative to the spin of a Kerr black hole with $\Omega_B = \Omega_0$. The residual spin is quite large.

spin (4.10). Fig. 6.4 has an inset which measures the spin of one of the black holes in a binary as a function of $m\Omega_0$. The graph actually shows the spins for a variety of Komar sequences with different excision boundary conditions for the lapse. The x and y components of the spin vanish to round-off error. The z component and the spin measured with the Killing transport equations increasingly differs from zero as the separation decreases. Figure 6.4 also graphs the magnitude of these spins divided by the spin a Kerr black hole would have with a rotational angular velocity equal to Ω_0. This measure of the magnitude of the spin as a ratio of what it would approximately be in the corotating case shows that the measured spins are significant. In fact, at what the Komar-mass ansatz predicts as the ISCO, there is as much as 30% of the spin as expected in the corotating case. Clearly, this assumption about finding nonspinning black holes is incorrect.

When applying the new method for creating nonspinning initial data, the use of the factor f_r in $\Omega_r = f_r\Omega_0$ allows us to set the spin to zero. In particular, we demand the

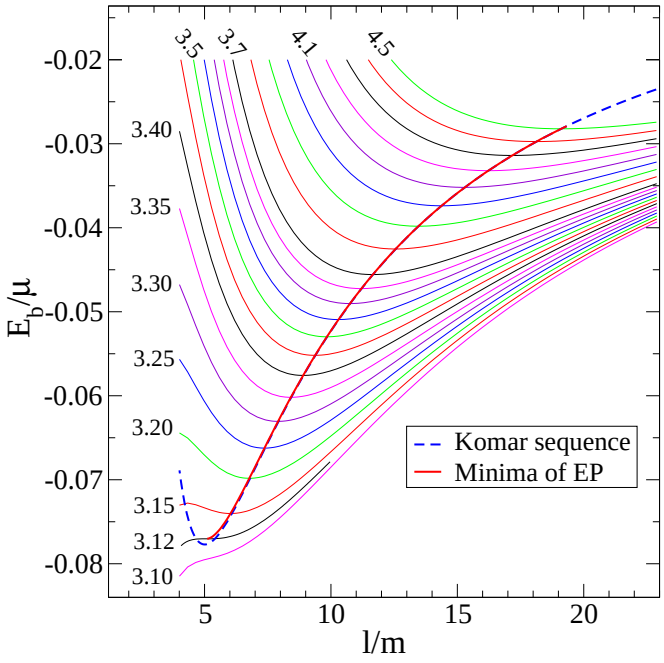

Figure 6.5: EP curves E_b/μ for "true" non-spinning black holes vs. separation ℓ/m. The curves are labeled by the orbital angular momentum $J/\mu m$ which is kept constant along each curve. The thick red line connecting the minima of the EP-curves represents circular orbits, and terminates at the innermost stable circular orbit at the inflection point in the EP-curve at $J/\mu m = 3.12$. Also plotted as a dashed blue line is the sequence of circular orbits as determined by the Komar-mass ansatz.

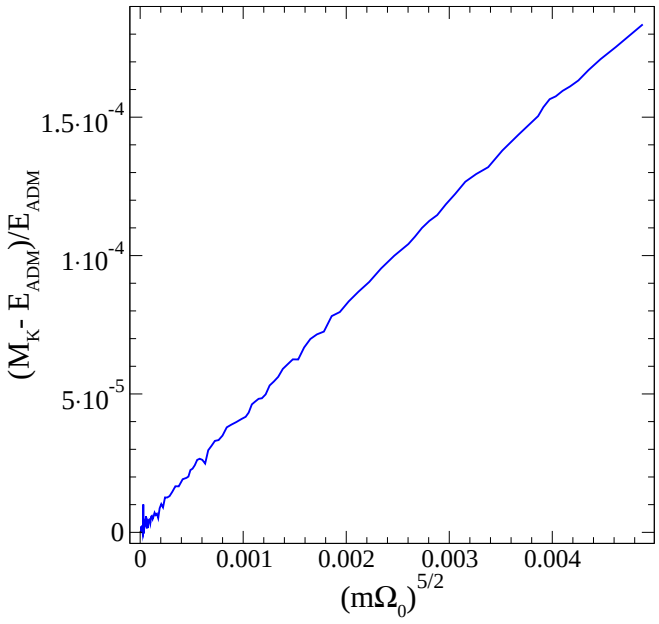

Figure 6.6: Violation of the Komar-mass condition when the effective-potential method is used to determine the sequence of circular orbits. Here, *non-spinning* (NS) equal-mass binaries are considered, and the sequence is parametrized by the orbital angular momentum.

spin measured using the Killing transport equations vanishes. Figure 6.5 shows the results for effective potentials, the effective-potential sequence, and the Komar sequence in the same manner as Figs. 6.1 and 6.3. Examining Fig. 6.5, one finds the effective potentials in the more familiar form. They posses both a local minimum and an inner local maximum which come together as angular momentum decreases finally to an ISCO at $J/\mu m = 3.12$. Further, the Komar sequence once again agrees well up to small separation with the effective-potential sequence.

Again, to have a more quantifiable measure, we look at the violation of the Komar-mass ansatz $\Delta M_{\rm K}/E_{\rm ADM}$ as a function of $(m\Omega_0)^{5/2}$ in Fig. 6.6 for the nonspinning case using $\Omega_r = f_r\Omega_0$. As before, we see the violation increasing linearly in $(m\Omega_0)^{5/2}$ with truncation noise appearing in the bottom left of the graph. Again, while the difference is definitely physical, it remains quite small.

A question remains as to what is the interpretation of the factor f_r. To examine this,

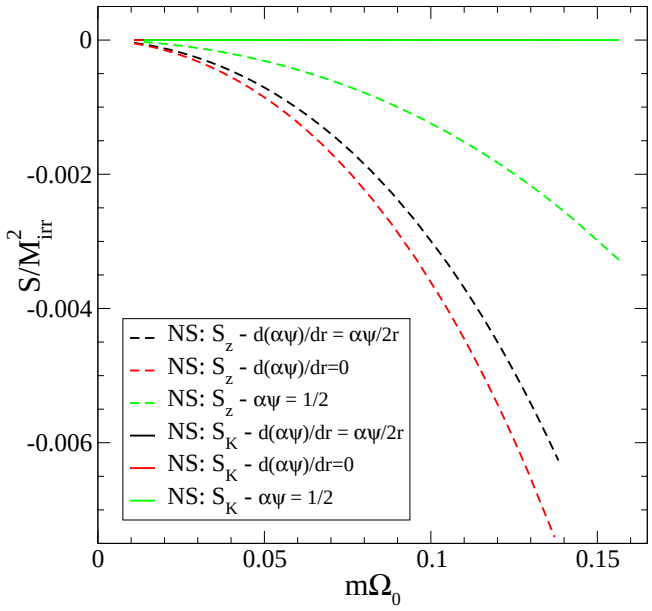

Figure 6.7: Quasi-local spin for a "true" non-spinning (NS) black hole in an equal-mass binary along the sequence of circular orbits, parametrized by the orbital angular velocity. The same six cases are plotted as in the inset of Fig. (6.4). Note that here $S_K = 0$ by construction.

first we look at Fig. 6.7, which shows the different measures of spin for a single black hole in the binary as a function of $m\Omega_0$. These sequences are for the circular orbits predicted with the Komar-mass ansatz and are plotted for different excision boundary conditions on the lapse. By construction, S_K is zero. As before, the x and y components of the spin are zero to within truncation error. The z component of the spin as measured using the flat-space Killing vector is not zero. It does however, remain below 1% of the maximal rotation.

Finally we can look at Fig. 6.8 to try to find if there is a form to f_r that has physical motivation. Here f_r is plotted for the Komar sequence against $(m\Omega_0)^{2/3}$. Shown in the dotted line is a simple fit from which the numerical data diverges. In [22] a function was found that fit f_r based on arguments made examining corotating data,

$$f_r = 1 - 0.925(m\Omega_0)^{2/3} + 0.36(m\Omega_0) - 1.4(m\Omega_0)^{4/3}, \tag{6.1}$$

but it was determined that this fit was not unique.

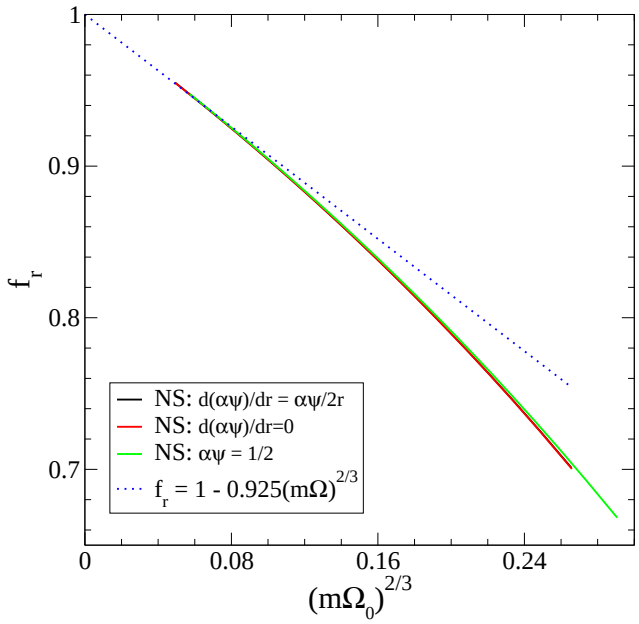

Figure 6.8: Rotation parameter $f_r = \Omega_r/\Omega_0$ along the sequence of non-spinning (NS) black holes, parametrized by the 2/3-power of the orbital angular velocity. The dotted line plots the fit to f_r through the term of order $(m\Omega_0)^{2/3}$.

6.2 Testing against the thermodynamic identity

Corotating equal-mass binary initial-data sets are not only easy to create, but have another advantage. Corotation is the only case where equal-mass binary black holes admit a true helical Killing vector [12, 36, 40]. To do this, however, one must instill the system with an infinite wave-train of incoming gravitational radiation to balance the effects of outgoing gravitational radiation emitted by the binary. For our initial-data formulations, we only have an approximate helical Killing vector.

Friedmann *et al.* [40] derived a thermodynamic identity which is applicable when there is a true helical Killing vector present:

$$\delta E_{\rm ADM} = \Omega_0 \delta J_{\rm ADM} + \sum \kappa_i \delta \mathcal{A}_i. \tag{6.2}$$

In Eq. (6.2), $J_{\rm ADM}$ is the magnitude of the total ADM angular momentum of the system, and κ_i and $\mathcal{A}_i$ are respectively the surface gravity and area of the Killing horizon of each

black hole. Eq. (6.2) has three variations in the relationship. To simplify the equation, we can apply a fundamental length rescaling $\chi(s)$ to enforce

$$\delta E_{\rm ADM} = \Omega_0 \, \delta J_{\rm ADM}. \tag{6.3}$$

This approach has been used before in [44, 33] and I will give the outline found in [22] for the rescaling method.

The length scale $\chi(s)$ will be applied, using an affine parameterization s, as follows:

$$E_{\rm ADM}(s) \equiv \chi(s) e(s), \tag{6.4}$$

$$J_{\rm ADM}(s) \equiv \chi^2(s) j(s), \tag{6.5}$$

$$\Omega_0(s) \equiv \chi^{-1}(s) \omega(s). \tag{6.6}$$

These are *definitions* for the total ADM energy $E_{\rm ADM}(s)$, the total ADM angular momentum $J_{\rm ADM}(s)$ and the orbital angular velocity $\Omega_0(s)$ at some point s along a sequence of circular orbit configurations. Then $e(s)$, $j(s)$ and $\omega(s)$ represent dimensionless versions of the same quantities.

We can then find the following length scaling

$$\chi(s_2) = \chi(s_1) \exp\left\{ - \int_{s_1}^{s_2} \frac{e'(s) - \omega(s) j'(s)}{e(s) - 2\omega(s) j(s)} ds \right\} \tag{6.7}$$

between two points s_1 and s_2 along a sequence. Here, a prime denotes differentiation along that sequence. Applying this effectively enforces Eq. 6.3, leaving us with

$$\sum \kappa_i \delta \mathcal{A}_i = 0. \tag{6.8}$$

To leading order, $\kappa = 1/4M_{\rm irr}$ for each hole, and the Killing horizon can be approximated by the apparent horizon of the black hole. For corotating data, the initial data is set up so the apparent horizon is a Killing horizon, at least locally in time. Effectively, this means that, so long as the length scaling above is applied, the irreducible masses of the black holes should not vary along a sequence of corotating equal-mass binary black holes in circular orbit.

Table 6.1: The irreducible mass $M_{\rm irr}$ of a single black hole in a corotating, non-spinning, and leading-order (LO) non-spinning binary as we vary the coordinate separation d. The length scale is set so that the ADM mass of the binary at very large separation is 1. $\left.\frac{d\alpha\psi}{dr}\right|_S = \left.\frac{\alpha\psi}{2r}\right|_S$ was used as the lapse boundary condition for all data.

	$M_{\rm irr}$		
d	Corotation	Non-spinning	"LO" non-spinning
40	0.5000000	0.5000000	0.5000000
35	0.5000001	0.5000001	0.4999988
30	0.5000002	0.5000002	0.4999966
25	0.5000005	0.5000005	0.4999902
20	0.5000010	0.5000011	0.4999727
19	0.5000013	0.5000014	0.4999659
18	0.5000016	0.5000017	0.4999568
17	0.5000020	0.5000021	0.4999446
16	0.5000025	0.5000026	0.4999281
15	0.5000032	0.5000033	0.4999050
14.5	0.5000037	0.5000037	0.4998901
14	0.5000042	0.5000042	0.4998721
13.5	0.5000048	0.5000048	0.4998504
13	0.5000056	0.5000055	0.4998238
12.5	0.5000065	0.5000064	0.4997911
12	0.5000076	0.5000074	0.4997504
11.5	0.5000090	0.5000086	0.4996992
11	0.5000107	0.5000102	0.4996340
10.5	0.5000129	0.5000120	0.4995498
10	0.5000157	0.5000144	0.4994393
9.5	0.5000193	0.5000173	0.4992918
9	0.5000240	0.5000211	0.4990908
8.5	0.5000308	0.5000259	0.4988091
8	0.5000401	0.5000330	0.4984008
7.5	0.5000529	0.5000423	0.4977815
7	0.5000702	0.5000546	0.4967842

The second column of Table 6.1 shows the irreducible mass, given the rescaling, for one black hole along a corotating Komar sequence of equal-mass binary black holes. For corotation with the excision boundary conditions applied, the excisions in each set of initial data should be Killing horizons meaning that if the orbits are quasicircular, the masses should not vary. The mass differs only about one part in ten-thousand along the sequence. This difference is above the various computational errors, suggesting there is some physical reason for this. Particularly, while corotation admits configurations with true helical Killing vectors, as mentioned above these initial data sets only have approximate helical Killing vectors, and while the apparent horizon is a Killing horizon on the spatial slice, it is not a global Killing horizon. Despite the error, which seems to stem from only having an approximate helical Killing vector, the variation in the mass is still quite small, suggesting the Komar-mass ansatz is correctly finding quasicircular orbits.

Column four of Table 6.1 shows the rescaled variation in irreducible masses of a black hole for nonspinning black hole binaries created with the assumption that $\Omega_r = \Omega_0$ along a Komar sequence. As can be seen, the variation of the mass along the whole sequence is as much as a few parts in a hundred. Column three shows the variation in mass along a nonspinning Komar-mass sequence when using the fractional quantity f_r. As can be seen, this sequence varies on the same scale as the corotating sequence. That the nonspinning data conforms to this thermodynamic identity as well as the corotating data implies there may be some more general application of the identity in an approximate form.

6.3 Discussion

In this Chapter, I described investigations to test how well the effective-potential method and Komar-mass ansatz finds quasicircular orbits, by testing them against each other and against an independent measure in the thermodynamic identity. In the process, I also described how we found that nonspinning binary black holes cannot be simply parametrized by setting $\Omega_r = \Omega_0$, but that nonspinning initial data should be found using root-finding to

set the measured spin to zero. This does not represent all the work described in [22] but only those parts to which my own efforts directly pertained. Primarily, I implemented the method for finding truly nonspinning binary black holes and ran Eric to create all of the data studied in [22]. I also wrote sequencers to create nonspinning Komar-sequences and effective potentials as well as the sequencer for creating EP sequences of either spin type.

As detailed above, quasicircular orbits found with the Komar-mass ansatz and the effective-potential method strongly agree until small separations. This held for corotating initial data and for nonspinning data once the fractional value f_r was used to set S_K to zero. Further, Komar sequences made of corotating binaries and "true" nonspinning binaries were found to differ only slightly, though definitely physically with the thermodynamic identity. The variation is attributable to the fact that in either case we only have an approximate helical Killing vector rather than a true helical Killing vector. This suggests the Komar-mass ansatz is successfully predicting quasicircular orbits. It was also noted in [22] that the effective-potential sequences, a series of minima of effective potentials, in fact agreed slightly better with the thermodynamic identity.

One may ask, which is better for finding circular orbits: the effective-potential method or the Komar-mass ansatz? While the effective-potential method was found to compare better with the thermodynamic identity, the difference was likely not enough to justify the immense computational expense required for finding circular orbits using the effective-potential method. Details of the resultant physics of the Komar-sequences for both the corotating case and for the "true" nonspinning case are provided in Appendix A.

A key result found in [22] that has not yet been reported here is about the assumed spin-angular velocity for black holes in corotation. It has typically been assumed that for corotating binary black holes, the actual spin angular velocity was equal to the orbital angular velocity. When the Kerr formula relating spin and angular velocity for a black hole,

$$S_{\rm Kerr}(M_{\rm irr}, \Omega_B) = \frac{4M_{\rm irr}^3 \Omega_B}{\sqrt{1 - 4(M_{\rm irr}\Omega_B)^2}}, \tag{6.9}$$

was applied, it was found this assumption led to a disagreement with the numerical results using the quasilocal definitions of spin in Eq. (4.10). To correct this difference, [22] made use of a leading order correction to the rotation rate Ω_T of the tidal field due to a companion star as measured in the local asymptotic rest frame (LARF) [70] of a black hole

$$\Omega_T = \Omega_0 \left[1 - \eta \frac{m}{b} + \mathcal{O}\left(\frac{m}{b}\right)^{3/2}\right], \tag{6.10}$$

where $\eta \equiv \mu/m$, and b is the separation of the black holes in harmonic coordinates. This correction term was computed by Alvi [1]. This was expressed in a gauge independent way using a post-Newtonian expansion for b/m obtained for circular orbits [49]

$$\frac{m}{b} = (m\Omega_0)^{2/3}\left[1 + (1 - \tfrac{1}{3}\eta)(m\Omega_0)^{2/3} + \mathcal{O}(m\Omega_0)\right]. \tag{6.11}$$

Substituting, one finds

$$\begin{aligned}\frac{\Omega_T}{\Omega_0} &= 1 - \eta(m\Omega_0)^{2/3} + \Lambda(m\Omega_0) \\ &\quad - \left[\eta(1 - \tfrac{1}{3}\eta) - \Gamma\right](m\Omega_0)^{4/3} + \mathcal{O}(m\Omega_0)^{\frac{5}{3}},\end{aligned} \tag{6.12}$$

where Λ and Γ are functions of η coming from the unknown terms of order $(m/b)^{3/2}$ and $(m/b)^2$ respectively in Eq. (6.10). The leading order error term in Eq. (6.11), which includes spin-orbit coupling terms, contributes to the term of order $(m\Omega_0)^2$ in Eq. (6.12). When Ω_T was taken to represent the spin angular velocity, the Kerr formula spin agreed much better with the other quasilocal measures of spin. This result is important for analyzing numerical initial data with post-Newtonian results. It suggests we should at least take the first correction term,

$$\frac{\Omega_T}{\Omega_0} = 1 - \eta(m\Omega_0)^{2/3} + \mathcal{O}(m\Omega_0), \tag{6.13}$$

for comparison.

Lastly, it was hypothesized in [22] that the quasiequilibrium condition of setting $\tilde{u}^{ij} \equiv -\partial_t \tilde{\gamma}^{ij} = 0$ effectively sets the radial motion of the binary black holes very close to zero. While this is not directly testable in initial data, this study found qualitative evidence that

supports the notion. That the numerical effective potentials for BBH's appear similar to the analytical effective potentials for a particle orbiting a black hole could be coincidental. Simply having an "inner local maximum" in the numerical data does not necessarily mean that "maximum" has real physical meaning. However, that the Komar sequences, based on an independent method, also show an increase in binding energy at small separations supports the notion that such maximums represent unstable circular orbits.

Chapter 7

Measuring eccentricity in binary black-hole initial data

While binary black-hole initial-data studies often only seek to model quasicircular orbits, it is not impossible that gravitational waves from binary black holes in eccentric orbits will one day be detected. Further, the two-body problem is perhaps the most fundamental unsolved problem in classical General Relativity and the study of eccentric orbits has great theoretical value. For any study of initial data representing BBH's in eccentric orbit to be complete, one would have to evolve such initial-data sets forward in time. Still, the numerical effective potentials may provide a way to estimate the eccentricity of BBH initial data. This chapter presents our efforts to understand eccentricity in initial data, both by looking at independent measures of eccentricity and by using direct "two-point methods" for defining eccentricity in an effective potential. A portion of the results presented here have been published in [45].

7.1 The 3PN equations

To better understand eccentricity in numerical initial data, we found an independent method to both make effective potentials for binary black holes and measure the eccentricity of numerical initial data. To do this, we made use of a pair of third order conservative post-Newtonian equations derived by Mora and Will [58, 59]. These equations measure the total

energy and angular momentum for the relativistic two body problem given the eccentricity, semilatus rectum, and spin angular velocities of the two objects. These equations ignore any dissipation due to gravitational radiation. For the study of the binary black-hole problem, the equations can be written as

$$\begin{aligned} E(\epsilon,\zeta,\omega) &= E_{\rm ADM}(\epsilon,\zeta) + E_{\rm self}(\epsilon,\zeta,\omega) \\ &\quad + E_{\rm N,Corr}(\epsilon,\zeta,\omega) + E_{\rm Spin}(\epsilon,\zeta,\omega) \end{aligned} \tag{7.1}$$

$$\begin{aligned} J(\epsilon,\zeta,\omega) &= J_{\rm ADM}(\epsilon,\zeta) + S(\epsilon,\zeta,\omega) \\ &\quad + J_{\rm N,Corr}(\epsilon,\zeta,\omega) + J_{\rm Spin}(\epsilon,\zeta,\omega) \end{aligned} \tag{7.2}$$

where ϵ is the eccentricity, ζ is the inverse of the semilatus rectum, and ω represents the spin angular velocities of the black holes[1]. In Eqs. (7.1) and (7.2), $E_{\rm ADM}$ and $J_{\rm ADM}$ are the ADM energy and angular momentum for point particles with zero spin. The self energy and spin terms ($E_{\rm self}$ and S) are derived as expansions of the Kerr formulas relating mass, spin, and rotational angular velocity. The Newtonian correction terms ($E_{\rm N,Corr}$ and $J_{\rm N,Corr}$) stem from the conversion of total mass to irreducible mass and the "Spin" terms ($E_{\rm Spin}$ and $J_{\rm Spin}$) represent spin-orbit effects. For the full form of these equations, I reprint Mora and Will's equations in Appendix B. The equations also depend implicitly on the masses of the black holes. While there is at least one other approach to finding eccentricity of binaries with post-Newtonian equations (see [55] and references therein), we made use of this one by Mora and Will. We found these equations useful for two tasks: creating third-order post-Newtonian (3PN) effective potentials, which we can compare to our numerical effective potentials, and as two definitions of eccentricity. This section describes how we did both.

The derivation of Eqs. (7.1) and (7.2) made use of the following definitions for eccen-

[1]We use a single parameter ω for simplicity. In general, specifying the spin of two black holes would require six parameters.

tricity ϵ and the inverse semilatus rectum ζ respectively:

$$\epsilon = \frac{\Omega_p - \Omega_a}{\Omega_p + \Omega_a} \tag{7.3}$$

and

$$\zeta \equiv \left(\frac{\sqrt{m\Omega_p} + \sqrt{m\Omega_a}}{2} \right)^{(4/3)} . \tag{7.4}$$

In (7.3) and (7.4), the subscripts a and p stand for apocenter and pericenter respectively, and $m\Omega$ is the unitless orbital angular velocity. Combining (7.3) and (7.4), the inverse semilatus rectum can be written in terms of the eccentricity and the orbital angular velocity at either pericenter or apocenter of an orbit:

$$\zeta = \left(\frac{m\Omega_p}{(1+\epsilon)^2} \right)^{(2/3)} = \left(\frac{m\Omega_a}{(1-\epsilon)^2} \right)^{(2/3)} . \tag{7.5}$$

These are unique definitions in the Newtonian effective one-body problem, but can only be assumed to be an approximation here in the relativistic two-body problem. Generally, for elliptic orbits, eccentricity is measured from zero to one; however, Eq. (7.5) is the only place in any of this work where the sign of the eccentricity matters. Therefore, for the rest of this chapter, we take the eccentricity to be negative at pericenter. This has the advantage of making the results below easier to read.

The first task is to use Eqs. (7.1) and (7.2) to create post-Newtonian effective potentials. To create an effective potential, we want to take series of data sets where the angular momentum is held constant. If we are only concerned with dimensionless quantities such as E/μ and $J/\mu m$, the masses can be kept constant by enforcing the mass-ratio to remain the same through an effective potential. We chose equal-mass black holes through out. A spin condition can be used to determine ω, defined as the orbital angular velocity of a black hole. We created nonspinning binary black-hole effective potentials which are made by setting $\omega = 0$. The only task that remains is to choose combinations of ϵ and ζ that all yield the same value for J along an entire EP. To do this, we simply iterate up from $\epsilon = 0$, using root-finding at each step to find the value for ζ that gives us the correct value for

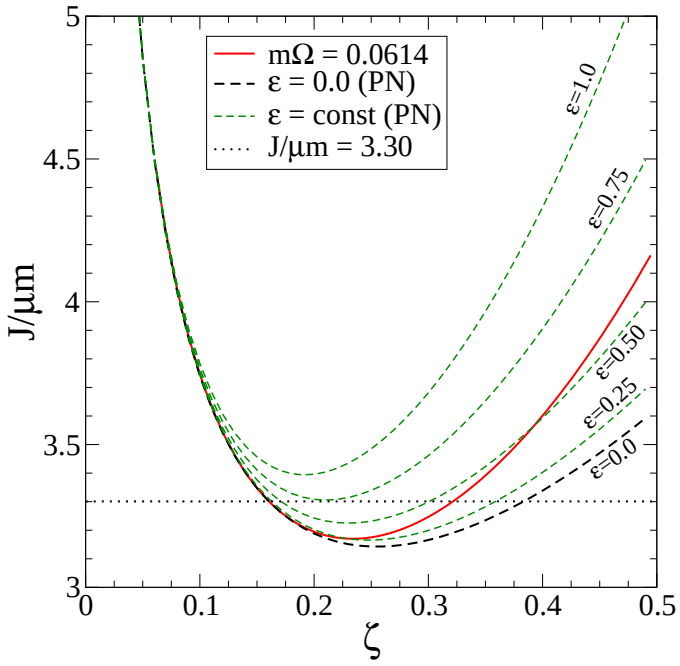

Figure 7.1: Parameter space of $J(\epsilon, \zeta)$ (Eq. (7.2)) for non-spinning equal-mass black holes. Short-dashed (green or black) lines of constant ϵ are constructed using the 3PN equations. The solid (red) line represents all 3PN models with a specific value of $m\Omega = 0.0614$ corresponding to a particular numerical model. The horizontal dotted (black) line represents the corresponding orbital angular momentum of that numerical model.

J. Eq. (7.5) can be used with a given ϵ and ζ to find the orbital angular velocity at both apocenter and pericenter and Eq. (7.1) provides the energy of each configuration.

Our other use for Eqs. (7.1) and (7.2) is to create two definitions ϵ_{E_b} and ϵ_J as the eccentricity found using Eq. (7.1) and the eccentricity found using Eq. (7.2) respectively. These definitions would be applied to our numerical initial data. For a given set of initial data, we have available the following physical measurements: the unitless orbital angular velocity $m\Omega$, the spin angular velocity for the black holes ω, the total energy for the system E and the total angular momentum for the system J. We eliminated ϵ in Eqs. (7.1) and (7.2) in favor of ζ and $m\Omega$ using Eq. (7.5). This effectively makes Eqs. (7.1) and (7.2) functions of ζ, $m\Omega$ and ω (so long as $m\Omega$ is taken at either apocenter or pericenter). One could then determine ζ from a set of initial data using the initial data's (ID's) values for $m\Omega$, ω, and either E or J depending on whether one was using Eqs. (7.1) or (7.2). This is

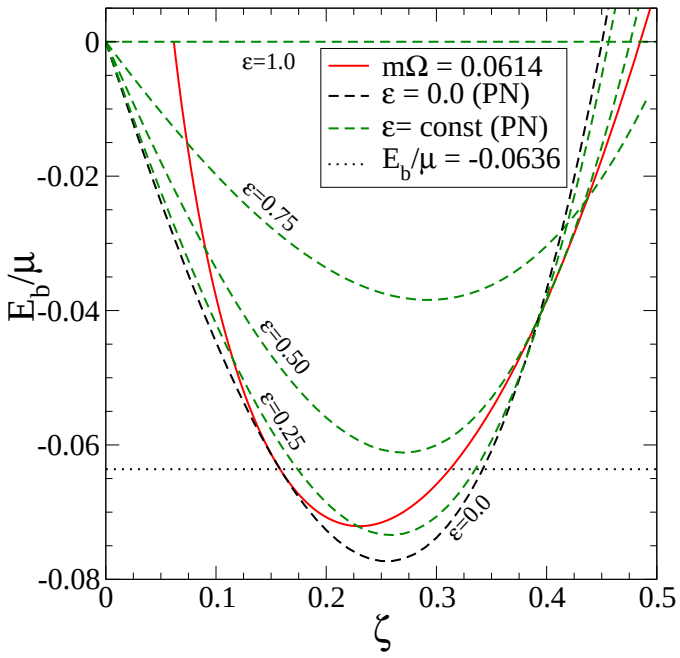

Figure 7.2: Parameter space of $E(\epsilon, \zeta)$ (Eq. (7.1)) for non-spinning equal-mass black holes. Lines as in Fig. 7.1 except the horizontal dotted(black) line represents the corresponding binding energy of the numerical model.

effectively done with one-dimensional root finding, for example finding a root in ζ so that Eq. (7.1) returns a value of $E = E_0$ where E_0 is the energy of the initial data. We recover the value of eccentricity by using Eq. (7.5) again.

In both tasks, the creation of post-Newtonian effective potentials and the estimates of eccentricity, there is a complication in determining a unique root when using either Eqs. (7.1) or (7.2), as both have multiple roots. So we must determine which root to use. Our choice is found by examining Figs. 7.1 and 7.2. In both, a solid red line is shown representing $m\Omega \approx 0.0614$ in the parameter space. This value was chosen because it was found to be at the minimum in binding energy (at an energy $E_b/\mu \approx -0.0636$) of the nonspinning numerical effective potential at angular momentum $J/\mu m = 3.30$. Fig. 7.1 shows two locations where the $m\Omega \approx 0.0614$ intersects the $J/\mu m = 3.30$ line and Fig. 7.2 shows two points where the $m\Omega \approx 0.0614$ intersects the $E_b/\mu \approx -0.0636$ line. These are not the only two roots in the 3PN equations but are enough to find the solution. We do

not expect the post-Newtonian equations to estimate an eccentricity of numerical initial data taken from a minimum of an effective potential to be far from zero. By examination of either figure, picking the second root in ζ implies an eccentricity above $\epsilon = 0.25$. Picking the first root results in an eccentricity much closer to zero. Thus it seems unreasonable to choose the second root and we consistently use the first positive root in ζ when using these equations to estimate eccentricity and to create effective potentials.

7.2 Can numerical effective potentials be used to find eccentric orbits?

In the Newtonian effective one-body problem, an effective potential nicely captures all the information required to define the possible orbits. Since radial motion is zero at every point along such effective potentials, EPs necessarily represent configurations either at apocenter or pericenter. For the fully relativistic two-body problem, numerical effective potentials are, at best, only an approximation. As an approximation, however, they may be the key to understanding eccentric orbits of binary black holes. Definitions of eccentricity found in the Newtonian effective one-body problem require physical measurements from both the apocenter and pericenter of orbit. We have reason to believe our data are at turning points. To test this, we will directly compare our effective potentials against those made with the Eqs. (7.1) and (7.2)

Figure 7.3 shows the binding energy as a function of the dimensionless orbital angular velocity $m\Omega$ for nonspinning equal-mass binary black-hole pairs. Dashed lines show numerical effective potentials. A thick gold line through the minima of the effective potentials shows the effective-potential sequence. The Komar-mass sequence is shown as a dotted-dashed line. All the numerical data presented here was originally created for the work in Chapter 6. The solid black lines show the post-Newtonian (PN) EPs created using Mora and Will's equations. The post-Newtonian EPs were taken at the same values of angular momentum as the numerical EPs. The larger values of angular momentum yield higher

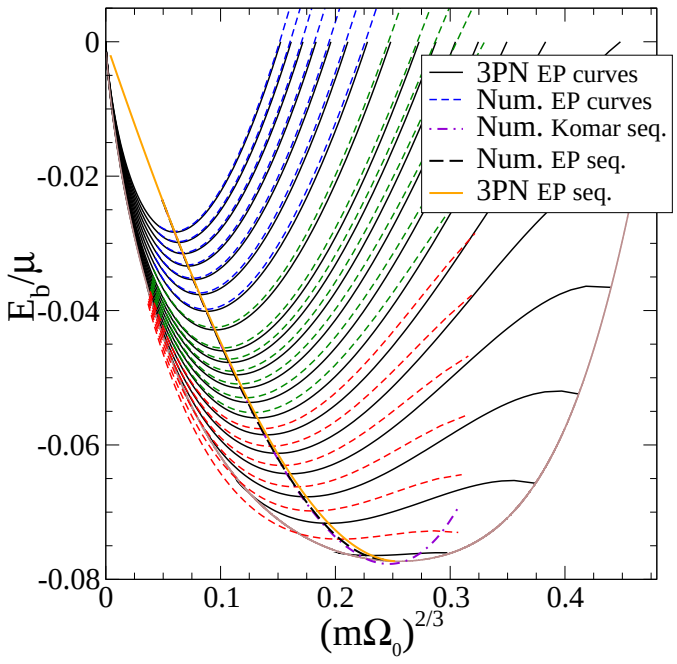

Figure 7.3: EP curves for non-spinning equal-mass black holes from both numerical and 3PN data. Numerical EP curves are plotted as short-dashed (blue, green, and red) lines. 3PN EP curves are plotted as solid (black) lines. The Komar sequence through the numerical data is plotted as a dash-dot (purple) line. The EP sequence through the numerical data is plotted as a long-dash (black) line. The EP sequence through the 3PN data is plotted as a light-solid (orange) line. A boundary of the allowable region for the 3PN equations is shown as a light-solid (brown) line.

binding energies. As can be seen, the numerical EPs match well with the PN EPs at the higher values of angular momentum and less so as the system becomes more relativistic (smaller $J/\mu m$).

The differences at smaller angular momentum can be traced to violations of assumptions made in both the post-Newtonian approximation and the numerical data. Post-Newtonian approximations are series expansions about the slow moving, weak-gravitational field limit. Both assumptions lead to greater error as separation between the black holes decrease. Similarly, as the gravitational fields get stronger, one expects greater dynamics. Thus the assumption of quasiequilibrium, used at many points in the creation of the numerical initial data, becomes less valid. Still, there is noticeable agreement in the less relativistic regime, suggesting that the numerical EPs are at least approximating "true" effective po-

tentials. It thus seems our initial data is created in configurations at least approximating "turning points".

7.3 Measuring eccentricity

We applied four different definitions of eccentricity to our numerical data: two based on the 3PN equations and two direct definitions. The two 3PN definitions, ϵ_{E_b} and ϵ_J require physical measurements from only one set of initial data to estimate an eccentricity. The two direct definitions make use of physical measurements at apocenter and pericenter of an orbit, thus requiring measures from two sets of initial data with the same binding energy.

The direct methods are found by examining equivalent definitions for eccentricity for Keplerian orbits. The first is based on separation, and the second is based on orbital angular velocity. The eccentricity of an ellipse is defined as $\epsilon = f/a$, where f is the focal length and a is the semi-major axis. If one has the separations of two bodies at the apocenter d_a and the pericenter d_p of an elliptical orbit, the focal length is $f = (d_a - d_p)/2$, and the semi-major axis is $a = (d_a + d_p)/2$. The result is our first definition of eccentricity:

$$\epsilon_d = \frac{d_a - d_p}{d_a + d_p}. \tag{7.6}$$

We must keep in mind that proper separation between the black holes is necessarily slicing dependent. Thus the measurement of separation becomes less accurate as the separation itself decreases and the configuration becomes more relativistic.

We can also apply the definition of eccentricity seen in Eq. (7.3). When computed using numerical data, we will label this eccentricity as ϵ_Ω and it is defined as

$$\epsilon_\Omega = \frac{m\Omega_p - m\Omega_a}{m\Omega_p + m\Omega_a}. \tag{7.7}$$

With either ϵ_d or ϵ_Ω, data is needed from pairs of turning points. That is, two sets of initial data with the same spins on the black holes, same total angular momenta and the same binding energies at either side of the local minimum of an effective potential. While

ϵ_d depends on separation, which is slicing dependent, ϵ_Ω depends on $m\Omega$, which is gauge independent. Clearly, by definition, both ϵ_d and ϵ_Ω are zero at the minimum of an effective potential. While the definitions ϵ_{E_b} and ϵ_J can be applied to any initial-data set, the definitions ϵ_Ω and ϵ_d require effective potentials.

In what follows, we will first examine the application of ϵ_{E_b} and ϵ_J to numerical data estimated to be in quasicircular orbit by both the effective-potential and Komar methods. This is done in comparison to a similar study by Berti *et al.* [11] for the Komar sequence data. I will then present the eccentricities approximated by all four definitions when used on numerical effective potentials. The different definitions will also be compared with each other. This will be done for both the nonspinning and corotating case.

7.3.1 Measuring eccentricity on quasicircular orbit predictions

Berti *et al.* [11] were first to apply ϵ_{E_b} and ϵ_J to different sets of initial data thought to be in quasicircular orbit. Among the various sets of data they examined were the Komar-mass sequences described in Chapter 6 and detailed in Appendix A for both the corotating and nonspinning cases. While they only applied the definitions to the Komar-mass sequences, we applied the definitions also to the EP sequences (the minima of the effective potentials). They consistently found that ϵ_{E_b} returned lower values for eccentricity. This section reports our findings for applying the definitions to both Komar and EP predictions of quasicircular initial data.

Figure 7.4 shows ϵ_{E_b} and ϵ_J as a function of orbital angular velocity for the nonspinning Komar-mass sequence and EP sequence. The lines labeled with a J were the eccentricities measured using ϵ_J and the lines labeled with E_b were measured using ϵ_{E_b} for the same sets of initial data. The solid lines are the minima of effective potentials while the dotted-dashed lines are the Komar-sequence. Just as Berti *et al.* found, the estimates of eccentricity using the equation for energy is consistently lower than the estimates of eccentricity using the angular momentum equation. We see that the EP sequence returns a slightly lower

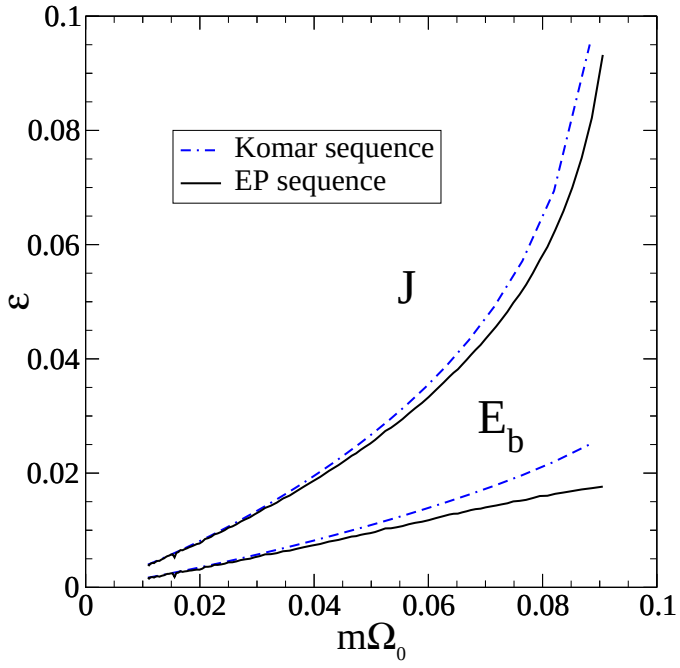

Figure 7.4: The 3PN eccentricity measures ϵ_{E_b} and ϵ_J applied to both Komar and EP sequences of non-spinning equal-mass black holes. Note that the EP minima yield quasi-circular data with a smaller eccentricity than is obtained from the Komar-mass ansatz.

estimate of eccentricity from either ϵ_{E_b} or ϵ_J. In all cases the lines seem to be asymptoting to zero as the separation increases ($m\Omega$ decreases). The higher eccentricities of the more relativistic configurations (higher $m\Omega$) are less meaningful as the orbits do not conform to elliptic orbits. It is encouraging, however, that the measured eccentricities never go above $\epsilon = 0.1$ and for ϵ_{E_b}, never above $\epsilon = 0.025$.

In the corotating case, Berti *et al.* [11] measured eccentricity under the Newtonian assumption that spin angular velocity was equal to the orbital angular velocity $\omega = \Omega_0$. However, as was found in [22], this is the wrong approach and a correction term shown at the end of Chapter 6 provides an estimate of ω that fits a relativistic local notion of corotation of the black holes much better. For this work on eccentricity we took ω to be

$$\omega = \Omega_0(1 - \eta(m\Omega_0)^{2/3}), \tag{7.8}$$

where $\eta = 1/4$ for equal-mass black holes. Figure 7.5 shows the measured eccentricity of

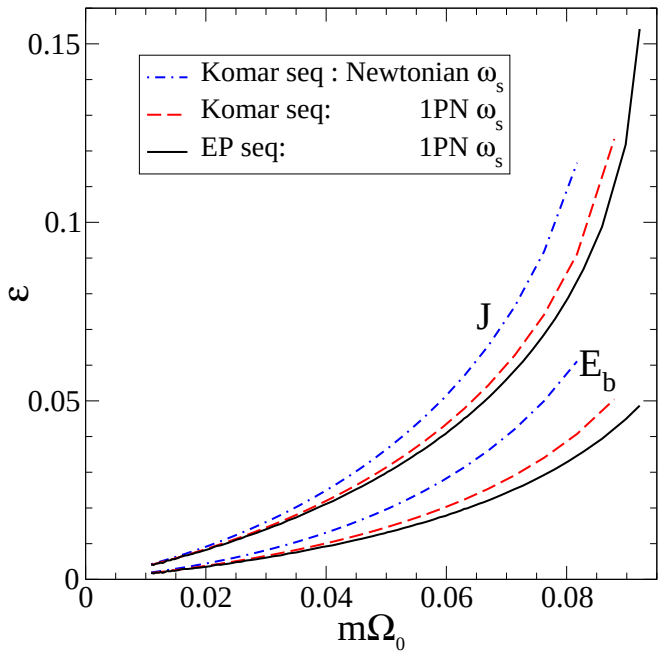

Figure 7.5: The 3PN eccentricity measures ϵ_{E_b} and ϵ_J applied to both Komar and EP sequences of *corotating* equal-mass black holes. The dot-dashed (blue) lines correspond to quasi-circular data defined via the Komar-mass ansatz and where the Newtonian notion of corotation is used in the 3PN equations. The dashed (red) lines show the improvement obtained by including the 1PN correction to the notion of corotation. The solid (black) lines show the added improvement of using quasi-circular data based on the EP method.

the corotating orbits. We recreated Berti *et al.*'s results for the Komar sequence in the dotted-dashed lines. The dashed lines are the Komar sequences using the higher-order approximation for ω and the solid lines are the EP sequences using the higher-order approximation for ω. Again, the lines marked with J were found using ϵ_J and the lines marked with E_b were found using ϵ_{E_b}. As before, the effective-potential sequence consistently yields slightly lower estimates of eccentricity than the Komar sequence. Also, the definition ϵ_J consistently yields higher values than ϵ_{E_b}. Using the higher-order definition for ω consistently yields lower estimates of eccentricity. Again, the estimates of eccentricity asymptote to zero as the separation increases ($m\Omega_0$ decreases). Notable is that at small separations, this corotating data yields noticeably higher measures of eccentricity than the non-spinning case.

7.3.2 Measuring eccentricities along effective potentials

The numerical effective potentials (NEPs) allow us to apply the direct definitions ϵ_d and ϵ_Ω to the initial data as well as the post-Newtonian definitions ϵ_{E_b} and ϵ_J. The nature of the effective potentials means that not all the numerical initial data can be used. ϵ_d and ϵ_Ω require data from pairs of turning points. This is limited in two ways. First, the NEPs are not calculated all the way out to infinite separation, and so there will be some pericenter configurations without a corresponding apocenter configuration. Second, at smaller values of angular momentum, there are local maxima in energy that are beneath $E_b = 0$. This means there can be apocenter configurations for which there is no corresponding pericenter configuration. The first limitation is imposed by computational expense. The latter limit is physical in nature. The post-Newtonian definitions are limited in a different way. While they do not need data at the corresponding turning points, as can be seen in Fig. 7.3, the parameter space of the post-Newtonian equations has limits on eccentricity beneath one. This is due to the parametrization of the post-Newtonian equations in terms of eccentricity and the inverse semilatus rectum. For the application of ϵ_d and ϵ_Ω, it is very unlikely that in the creation of the numerical effective potentials, initial data sets were actually calculated in "pairs of correlated turning points". That is, for a given configuration, say at apocenter, it is unlikely the method of creating effective potentials actually found a corresponding turning point initial-data set, in this case at pericenter, that has the same binding energy. Thus to find pericenter and apocenter data with the same binding energy, interpolation would be used. While the error in this interpolation is generally small, it is noticeable in ϵ_d and ϵ_Ω as noise near the minima of the effective potentials.

Figure 7.6 shows ϵ_d measured against $(m\Omega_0)^{2/3}$ for the nonspinning NEPs. Recall that eccentricities less than zero correspond to pericenter configurations. To simplify identification of individual NEPs, they have been divided into three categories based on the value of the total angular momentum. The blue dashed-dotted effective potentials have the

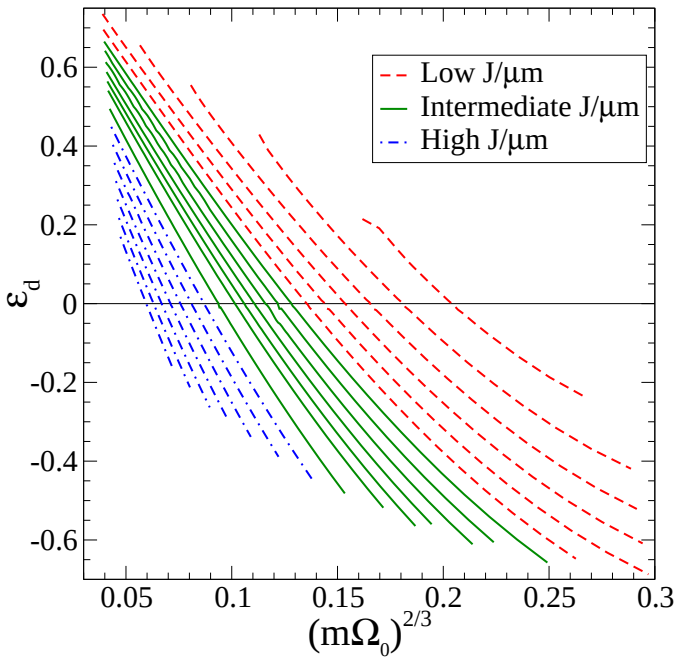

Figure 7.6: Eccentricity of non-spinning numerical effective potentials using ϵ_d plotted against $(m\Omega)^{(2/3)}$. Dashed (red) lines are used to denote the smallest values of angular momentum, solid (green) lines represent medium values of angular momentum and dotted-dashed (blue) lines represent the largest values of angular momentum.

highest values of angular momentum. The solid green lines are a medium range of $J/\mu m$. Lastly, the dashed red lines are the NEPs with the lowest values of angular momentum. By definition, the minima of the effective potentials are along the line marked $\epsilon_d = 0$.

Figure 7.7 shows ϵ_Ω measured against $(m\Omega_0)^{2/3}$ for the same effective potentials. The line and color scheme is the same as used in Fig. 7.6. Again, by definition, the minima of the effective potentials are found at $\epsilon_\Omega = 0$.

At large separation, if ϵ_d and ϵ_Ω are valid, they must agree. Fig. 7.8 plots the relative difference $(\epsilon_d - \epsilon_\Omega)/\epsilon_\Omega$ as a function of $(m\Omega_0)^{2/3}$. Note that the minima of the effective potentials have been removed, as both ϵ_d and ϵ_Ω are defined to report zero eccentricity for those configurations. One can still identify where those minima would be, however, as they are centered in areas with numerical noise. The differences are small at the larger values of angular momentum, but the differences increase as the angular momentum decreases. The

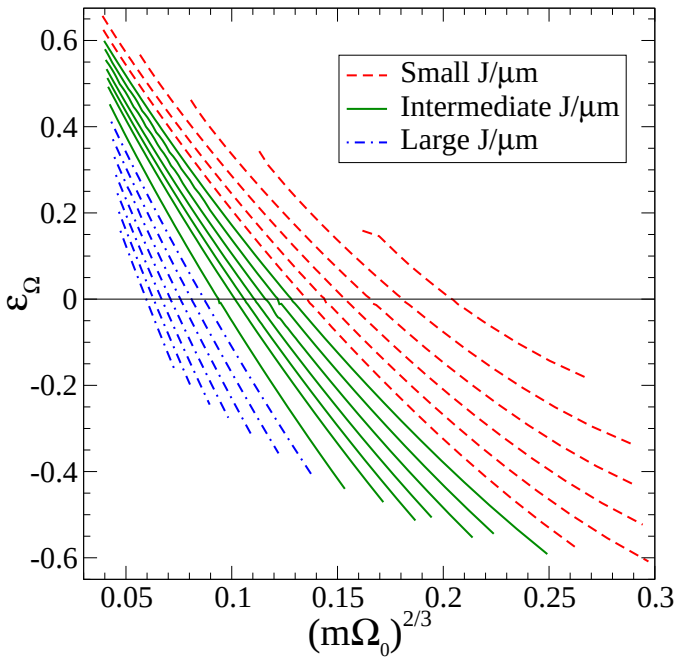

Figure 7.7: Eccentricity of non-spinning numerical effective potentials using ϵ_Ω plotted against $(m\Omega)^{(2/3)}$. Lines as in Fig. 7.6.

deviation seen here indicates the uncertainty in either definition.

Figure 7.9 plots ϵ_{E_b} as a function of $(m\Omega_0)^{2/3}$ for the nonspinning numerical effective potentials. The same color and line schemes are used here as with the direct definitions. As first noticed in [11, 58, 59], the minima of the effective potential curves do not correspond exactly to $\epsilon_{E_b} = 0$. A series of $\times$'s have been provided to mark those minima where $\epsilon_\Omega = 0$. This shows that while the data here is qualitatively similar to ϵ_d and ϵ_Ω, it does not perfectly match. Also, at large $J/\mu m$'s, it should be noted that ϵ_{E_b} is calculated for more of the effective potentials, since ϵ_{E_b} does not require corresponding pairs of initial data.

Figure 7.10 plots ϵ_J against $(m\Omega_0)^{2/3}$. These have the same color and line schemes and the same use of $\times$ symbols as Fig. 7.9. While qualitatively similar, one can again see in the $\times$'s that the minima of the effective potentials measure a higher ϵ_J than ϵ_{E_b}.

Again we wish to see how our different definitions of eccentricity compare to each other. Figure 7.11 plots $\epsilon_\Omega - \epsilon_{E_b}$ against ϵ_Ω and Fig. 7.12 plots $\epsilon_\Omega - \epsilon_J$ against ϵ_Ω. These figures

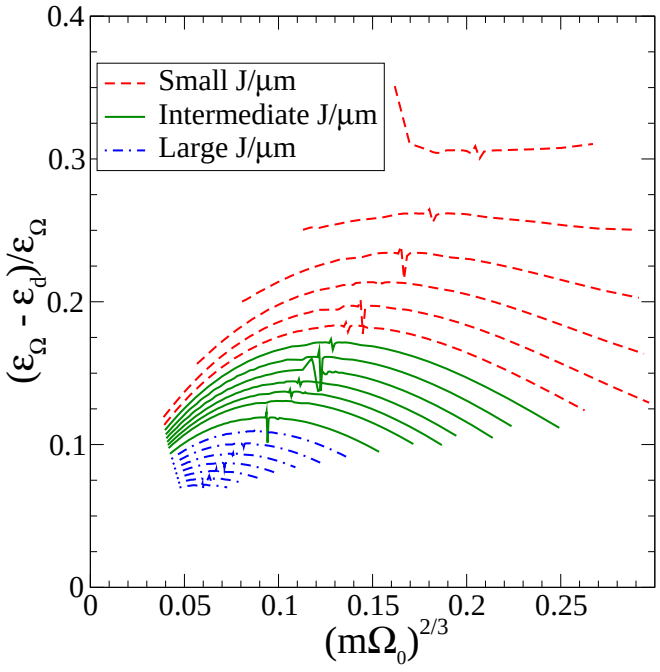

Figure 7.8: The relative difference between the ϵ_Ω and ϵ_d definitions of eccentricity for the non-spinning equal-mass black-hole numerical EP curves. Lines as in Fig. 7.6.

are presented this way as opposed to a relative difference to avoid issues when dividing by zero at $\epsilon_\Omega = 0$ (remember ϵ_Ω does not evaluate to zero at the same place as either ϵ_{E_b} or ϵ_J). This insures the plots are easy to read. Not surprisingly, there are smaller differences for the less relativistic cases (large $J/\mu m$) and the differences increase as $J/\mu m$ decreases. There is a jaggedness found in both plots at $\epsilon_\Omega = 0$ caused by the polynomial fitting used to estimate the minima of the effective potentials. The relative error is necessarily unbounded at $\epsilon_\Omega = 0$. However, for modest values of ϵ_Ω, the error stays at or under 20% when compared to ϵ_{E_b}. When compared to ϵ_J, the error goes well above 50% for the smaller values of angular momentum. This implies that at larger separations and larger angular momenta, the definitions ϵ_Ω, ϵ_{E_b} and ϵ_J are in close agreement. However, as the separation between the two black holes decrease the differences again exhibit the lack of a unique definition of eccentricity in strongly relativistic binaries.

Corotating effective potentials pose a problem for the direct definitions of eccentricity.

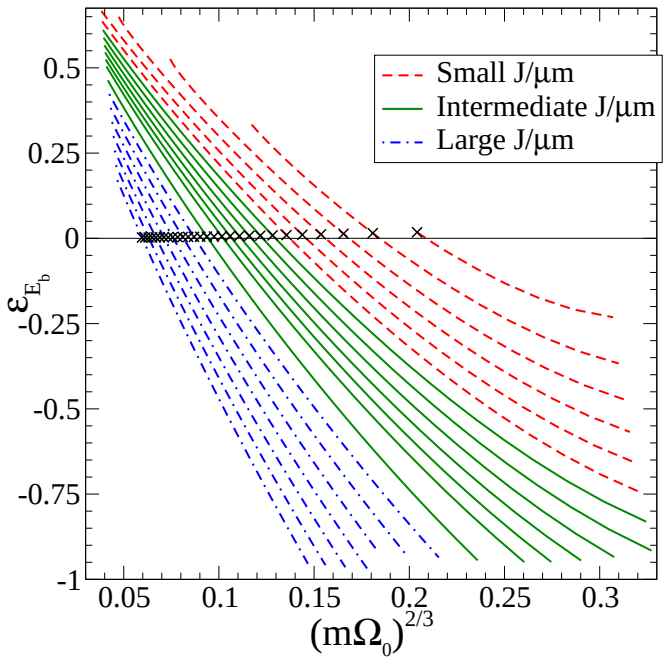

Figure 7.9: Eccentricity of non-spinning equal-mass black holes computed along numerical EP curves. The 3PN ϵ_{E_b} definition of eccentricity is plotted against the orbital angular velocity. Lines are as in Fig. 7.7. The $\times$ symbols mark the minima of each EP curve.

Since apocenter and pericenter data of a corotating EP will have different orbital angular momenta, the two initial-data sets do not represent apocenter and pericenter of the same orbit — even if dissipative radiation is ignored. This makes ϵ_d and ϵ_Ω less valid for corotating effective potentials. However, in the region of the minimum of the EPs, the difference in separation between pericenter and apocenter will be small so the difference in spins will be small. Thus ϵ_d and ϵ_Ω should be valid near quasicircular orbits.

Figures 7.13 and 7.14 plot ϵ_d and ϵ_Ω respectively against $(m\Omega)^{2/3}$. As in the nonspinning case, by definition, both ϵ_d and ϵ_Ω are zero at the minimum. While qualitatively the eccentricities taken along the effective potentials look similar to measures of ϵ_d and ϵ_Ω for the nonspinning case, it is important to remember that the values of eccentricity further from zero are necessarily suspect.

Again we examine the relative difference $(\epsilon_\Omega - \epsilon_d)/\epsilon_\Omega$ in Fig. 7.15 plotted against $(m\Omega)^{2/3}$, this time for the corotating effective potentials. Again the minima of the effective

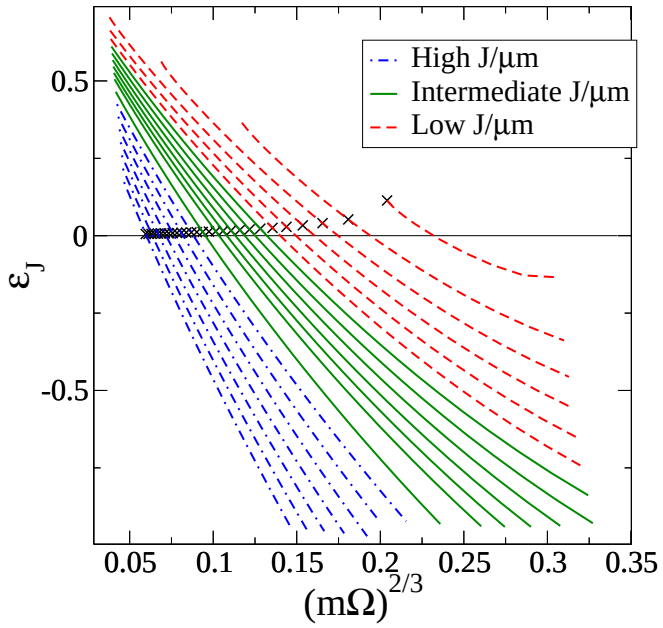

Figure 7.10: Eccentricity of non-spinning equal-mass black holes computed along numerical EP curves. The 3PN ϵ_J definition of eccentricity is plotted against the orbital angular velocity. Lines are as in Fig. 7.7. The $\times$ symbols mark the minima of each EP curve.

potentials have been removed to clean up the graph, but they can be identified by the jaggedness associated with the interpolation of the minima of the EPs. The differences are small for the largest values of angular momentum and increase as the system becomes more relativistic (smaller $J/\mu m$). This comparison can be considered suspect. Neither ϵ_Ω nor ϵ_d should be trusted as one measures eccentricity too far from the minima of the effective potentials, and too close to the minima the differences are often dominated by noise.

While apocenter and pericenter data for the corotating effective potentials may not directly correlate, ϵ_{E_b} and ϵ_J do not explicitly require pairs of turning points, thus these definitions of eccentricity are not suspect when applied further from the minimums of the effective potentials. Figures 7.16 and 7.17 show ϵ_{E_b} and ϵ_J plotted against $(m\Omega)^{2/3}$. Again, $\times$'s mark the minima of the effective potentials. Noticeable in both cases is that the effective potentials with the lowest angular momentum do not even cross the $\epsilon = 0$ line. This does not represent some fundamental flaw of either the numerical data or the post-Newtonian

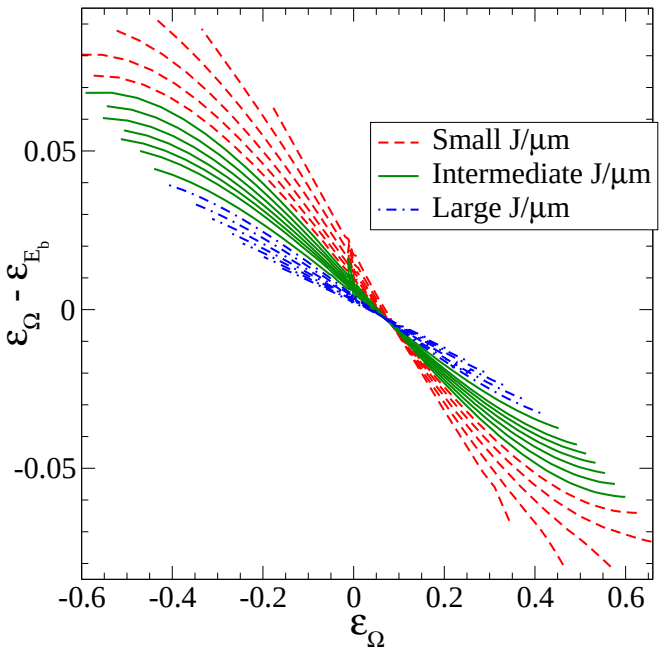

Figure 7.11: Difference between ϵ_Ω and ϵ_{E_b} plotted against ϵ_Ω for non-spinning equal-mass black holes computed along numerical EP curves. Lines are as in Fig. 7.7.

equations but rather exemplifies the level of disagreement between the PN equations and the numerical initial data at such relativistic separations.

Plotted in Figs. 7.18 and 7.19 is the difference between the direct definition of eccentricity ϵ_Ω and the two PN definitions, ϵ_{E_b} and ϵ_J respectively. The differences are plotted against ϵ_Ω. As in the nonspinning case, the relative difference is not plotted as it would be unbounded at $\epsilon_\Omega = 0$. While harder to see here, there is noise around $\epsilon_\Omega = 0$ on each effective potential due to the method used to approximate the minimum. These plots clearly show that for corotating effective potentials, ϵ_Ω does not agree with ϵ_{E_b} or ϵ_J nearly as well as in the nonspinning case. This is, however, an expected result as ϵ_Ω should only be valid near the minima of the effective potentials.

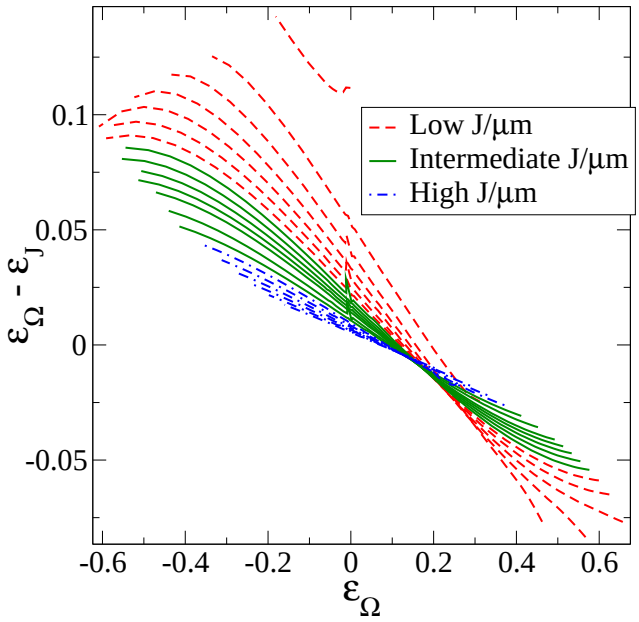

Figure 7.12: Difference between ϵ_Ω and ϵ_J plotted against ϵ_Ω for non-spinning equal-mass black holes computed along numerical EP curves. Lines are as in Fig. 7.7.

7.4 Parameterizing eccentric orbits with the Komar-mass difference

Creating numerical effective potentials is computationally expensive and it would be beneficial if the eccentricity of the initial data could be parametrized somehow without having to construct EPs. Since setting the Komar-mass difference to zero $\Delta M_{\rm K} = 0$ approximates quasicircular orbits, it seems plausible that the Komar-mass difference could be used as a measure that approximates eccentricity.

Figures 7.20, 7.21, 7.22 and 7.23 plot ϵ_d, ϵ_Ω, ϵ_{E_b} and ϵ_J respectively against the Komar-mass difference ΔK for the nonspinning numerical effective potentials. In this case, we weight the Komar-mass difference as

$$\Delta K = (E_{\rm ADM} - M_{\rm K})/\mu. \tag{7.9}$$

In all four case, there is a strong correlation between the Komar-mass difference and the measured eccentricities. However, this correlation does break down as $J/\mu m$ decreases. In

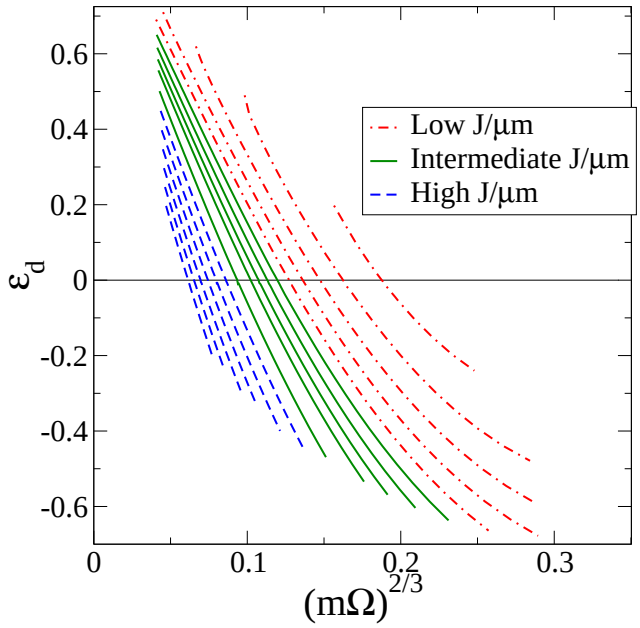

Figure 7.13: Eccentricity of corotating numerical effective potentials using ϵ_d plotted against $(m\Omega)^{(2/3)}$. Lines as in Fig. 7.6.

each graph, as the effective potentials with smaller $J/\mu m$'s decrease into negative eccentricity (pericenter), they curve back towards $\Delta K = 0$. This effect in these plots is consistent with the presence of local maxima in the effective potentials representing unstable quasicircular orbits. It also exemplifies how any hope of defining a reasonable eccentricity breaks down in the highly relativistic regime.

Figures 7.24 and 7.25 show ϵ_d and ϵ_Ω as a function of the Komar-mass difference for the corotating numerical effective potentials. Superficially, these have the same appearance as their nonspinning counterparts (Figs. 7.20 and 7.21) in that the effective potentials with smaller angular momenta do curve back towards zero Komar-mass difference at negative eccentricities. Those eccentricities are not entirely believable though because they came from two sets of initial data that did not have the same spins. Still, at larger angular momenta and eccentricities, there exists a strong correlation between the Komar-mass difference and ϵ_d or ϵ_Ω. Figures 7.26 and 7.27 show ϵ_{E_b} and ϵ_J plotted against the Komar-mass difference

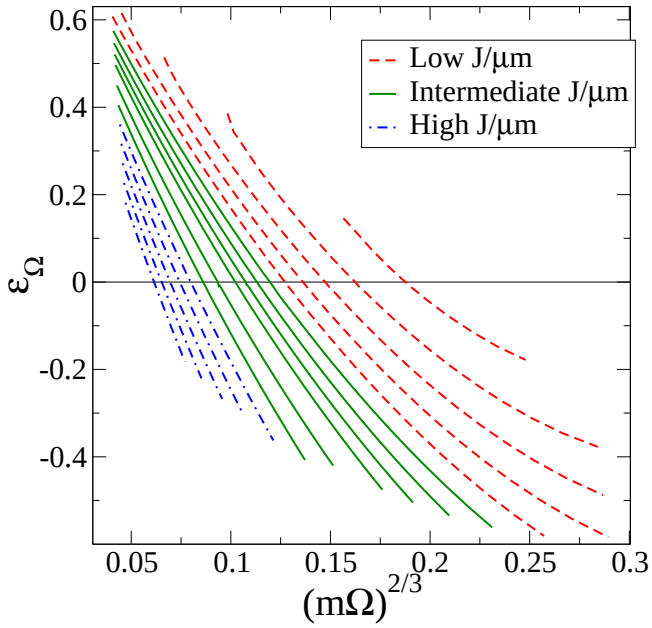

Figure 7.14: Eccentricity of corotating numerical effective potentials using ϵ_Ω plotted against $(m\Omega)^{(2/3)}$. Lines as in Fig. 7.6.

for the same corotating numerical effective potentials. These too show a strong correlation that decreases as angular momentum decreases.

7.5 Discussion

This chapter started with describing Mora and Will's [58, 59] conservative post-Newtonian equations for energy and angular momentum. It was shown both how those equations could be used to create PN effective potentials and to define two estimates of the eccentricity of a set of initial data. Comparing the numerical EPs to the post-Newtonian EPs found strong agreement at the larger values of angular momentum with predictably less agreement as the angular momentum decreased. This agreement suggest the numerical EPs we've created at least approximate true effective potentials for larger $J/\mu m$. This supports the idea that setting $\tilde{u}^{ij} = 0$ is consistent with the radial velocity of the black holes in the initial data being zero. Most importantly, it suggests we are creating numerical initial data at either

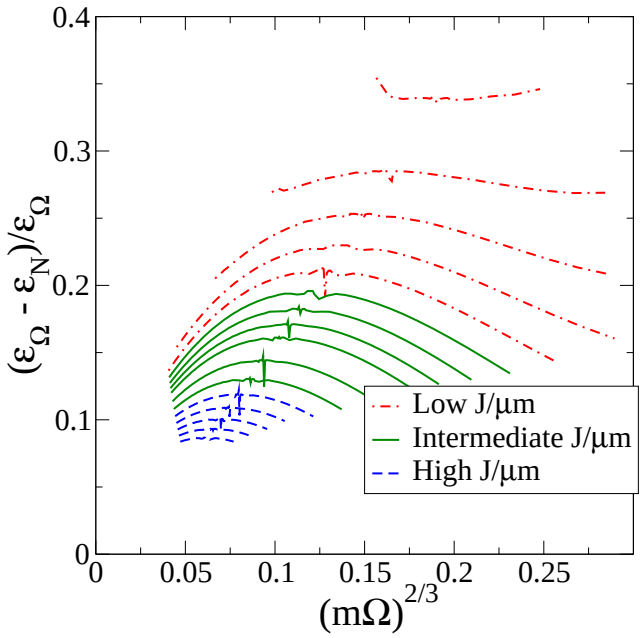

Figure 7.15: The relative difference between the ϵ_Ω and ϵ_d definitions of eccentricity for the corotating equal-mass black-hole numerical EP curves. Lines as in Fig. 7.6.

apocenter or pericenter. This means we can apply definitions of eccentricity dependent on data at turning points.

We applied two direct definitions of eccentricity that make use of data at pairs of turning points and applied the two definitions of eccentricity found in Mora and Will's post-Newtonian equations. When applying ϵ_{E_b} and ϵ_J to the predictions of quasicircular orbits, it was consistently found that the effective-potential sequences (the minima of the effective potentials) yielded lower eccentricities. We further found agreement with [11] that ϵ_{E_b} consistently found lower eccentricities. In the corotating case, we applied a higher-order approximation to define the spin angular velocity for corotation as prescribed in [22] and found this lowered the post-Newtonian estimates of eccentricity. Applying all the definitions of eccentricity to the effective potentials, we found good agreement between all definitions at higher angular momenta but that decreased as angular momentum decreased. This exhibits strongly the fact that there is no unique definition of eccentricity when the gravitational

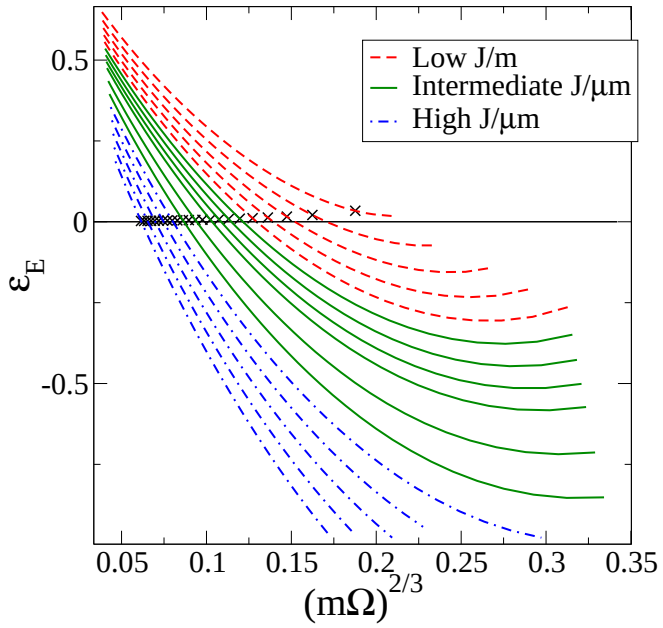

Figure 7.16: Eccentricity of corotating equal-mass black holes computed along numerical EP curves. The 3PN ϵ_{E_b} definition of eccentricity is plotted against the orbital angular velocity. Lines are as in Fig. 7.7. The $\times$ symbols mark the minima of each EP curve.

fields are strong. It should also be noted the application of ϵ_d and ϵ_Ω to the corotating effective potentials was only valid near the minima of the effective potentials where the spins differed only slightly between pericenter and apocenter turning points. A complete study of eccentric orbits for binary black holes in initial data would necessitate evolving that data forward in time. To that end, the use of effective potentials to find particular eccentric orbits would be computationally expensive. To overcome that, we examined using the Komar-mass difference ΔK as an invariant parametrization for eccentricity. We found a strong correlation between all the definitions of eccentricity and the Komar-mass difference.

It became evident to us that the 3PN effective potentials we created do not always allow for data that reaches infinite separation. This can be clearly seen in Fig. 7.3 where a line has been provided to mark the boundary of the parameter space of the 3PN equations. While the numerical effective potentials extend to very small $m\Omega$ (and theoretically can extend to zero $m\Omega$), there are 3PN effective potentials which do not. This limit exists

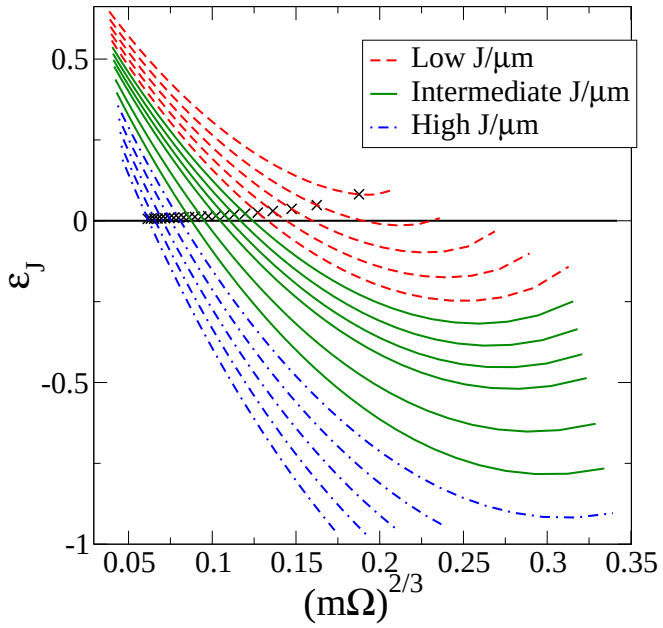

Figure 7.17: Eccentricity of corotating equal-mass black holes computed along numerical EP curves. The 3PN ϵ_J definition of eccentricity is plotted against the orbital angular velocity. Lines are as in Fig. 7.7. The $\times$ symbols mark the minima of each EP curve.

because for sufficiently small values of $J/\mu m$, the effective potentials have a local maximum at tight separations. While ϵ_{E_b} and ϵ_J can be found using data from only one configuration, the 3PN equations themselves are based on an eccentricity and inverse semilatus rectum defined using a two-point method. No method should be able to define an eccentricity for apocenter portions of an effective potential with a binding energy higher than an inner local maximum of binding energy. This raises an interesting question as to what would happen if initial data taken at one of these apocenter configurations where the energy is higher than the local maximum were evolved forward in time. This is a line of research I would like to one day explore.

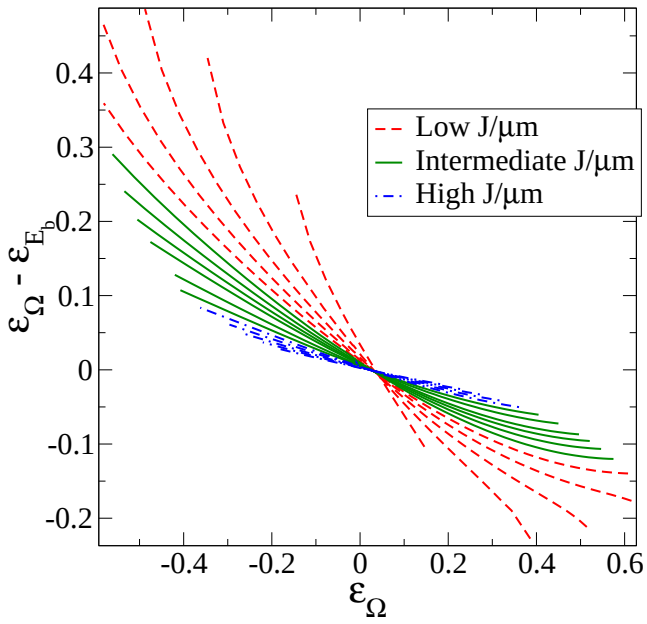

Figure 7.18: Difference between ϵ_Ω and ϵ_{E_b} plotted against ϵ_Ω for corotating equal-mass black holes computed along numerical EP curves. Lines are as in Fig. 7.7.

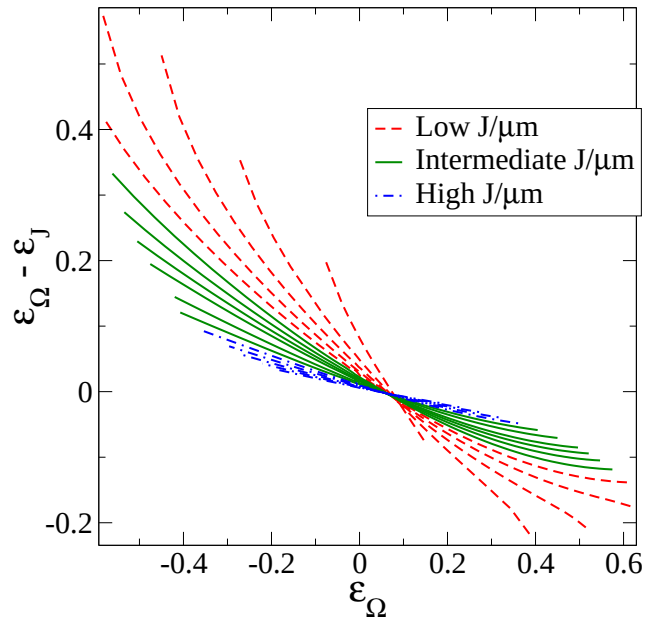

Figure 7.19: Difference between ϵ_Ω and ϵ_J plotted against ϵ_Ω for corotating equal-mass black holes computed along numerical EP curves. Lines are as in Fig. 7.7.

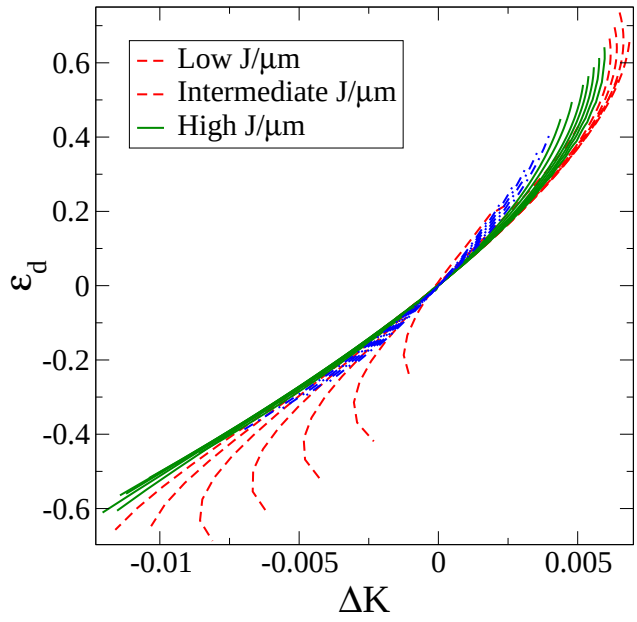

Figure 7.20: The eccentricity measure ϵ_d applied to non-spinning equal-mass black holes computed along numerical EP curves and plotted against the Komar-mass difference ΔK. Lines are as in Fig. 7.7.

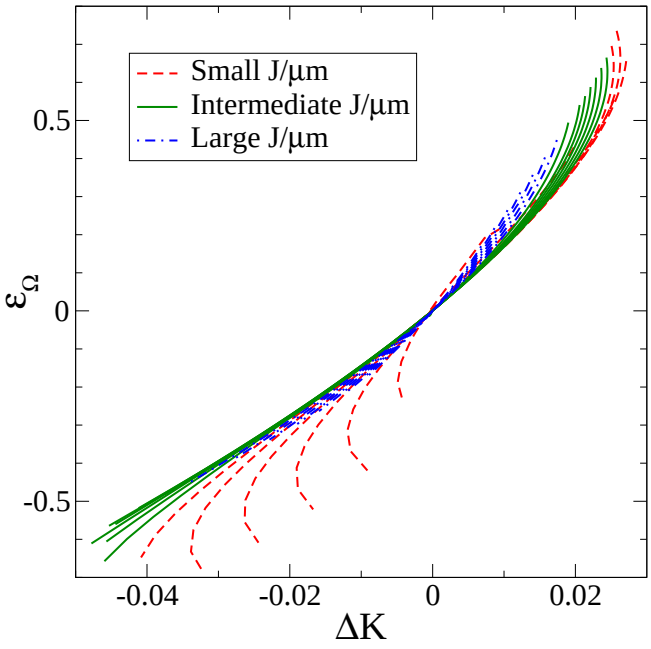

Figure 7.21: The eccentricity measure ϵ_Ω applied to non-spinning equal-mass black holes computed along numerical EP curves and plotted against the Komar-mass difference ΔK. Lines are as in Fig. 7.7.

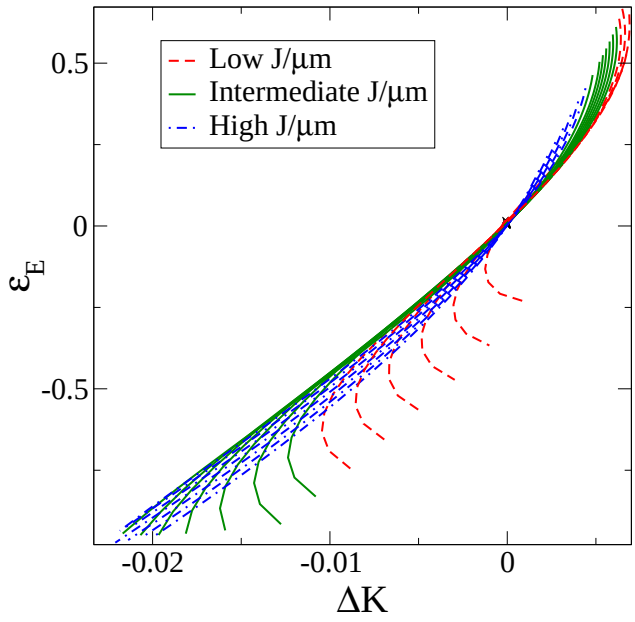

Figure 7.22: The eccentricity measure ϵ_{E_b} applied to non-spinning equal-mass black holes computed along numerical EP curves and plotted against the Komar-mass difference ΔK. Lines are as in Fig. 7.7.

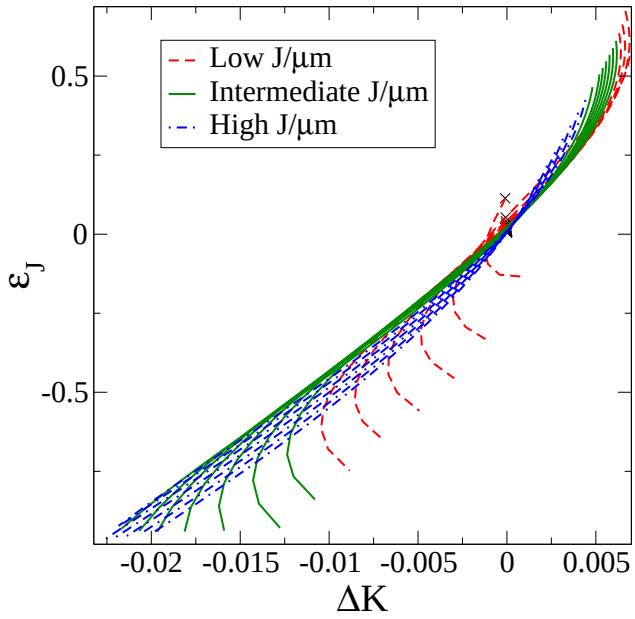

Figure 7.23: The eccentricity measure ϵ_J applied to non-spinning equal-mass black holes computed along numerical EP curves and plotted against the Komar-mass difference ΔK. Lines are as in Fig. 7.7.

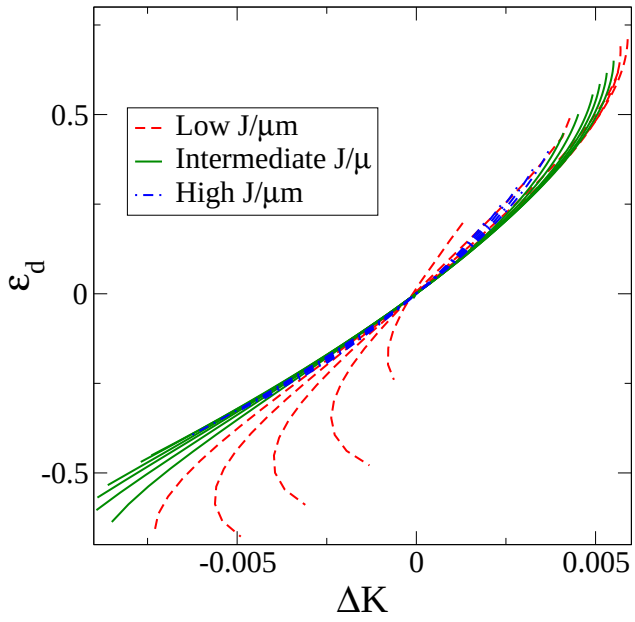

Figure 7.24: The eccentricity measure ϵ_d applied to corotating equal-mass black holes computed along numerical EP curves and plotted against the Komar-mass difference ΔK. Lines are as in Fig. 7.7.

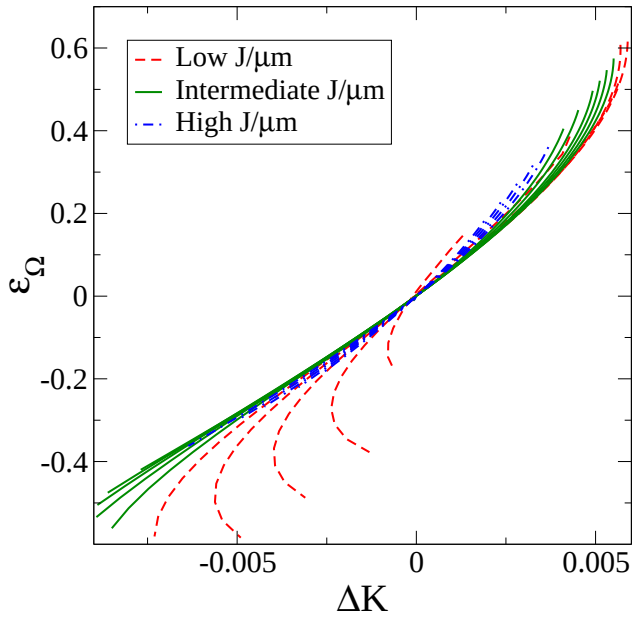

Figure 7.25: The eccentricity measure ϵ_Ω applied to corotating equal-mass black holes computed along numerical EP curves and plotted against the Komar-mass difference ΔK. Lines are as in Fig. 7.7.

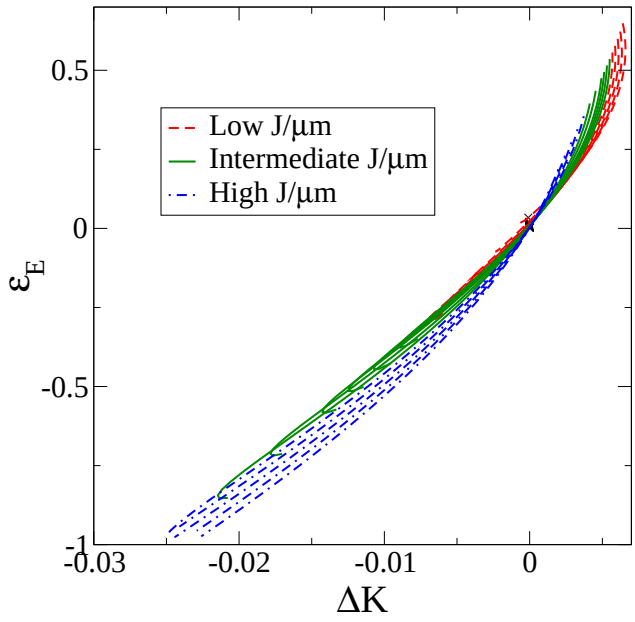

Figure 7.26: The eccentricity measure ϵ_{E_b} applied to corotating equal-mass black holes computed along numerical EP curves and plotted against the Komar-mass difference ΔK. Lines are as in Fig. 7.7.

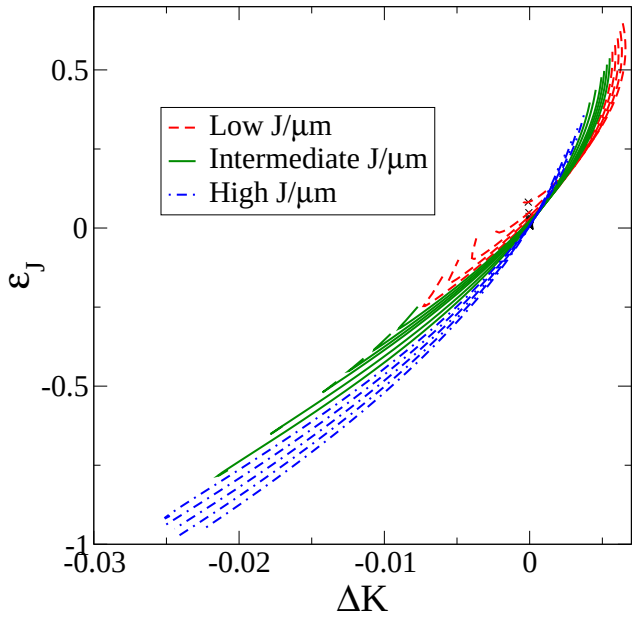

Figure 7.27: The eccentricity measure ϵ_J applied to corotating equal-mass black holes computed along numerical EP curves and plotted against the Komar-mass difference ΔK. Lines are as in Fig. 7.7.

Chapter 8

Conformal Flatness

Up to this point, all the work in binary black-hole initial data described here has been done with the choice of conformal flatness. That is, when the conformal decomposition $\gamma^{ij} = \psi^{-4}\tilde{\gamma}^{ij}$ is made, the conformal metric is chosen to be the flat metric f^{ij}:

$$\tilde{\gamma}^{ij} \equiv f^{ij}. \tag{8.1}$$

This choice actually has a number of advantages. First, it simplifies the constraint equations. Second, such a choice helps ensure the resultant boundary-value problem is well-posed. However, we also know from post-Newtonian results that the actual physical situation of an adiabatically inspiraling binary black-hole system is not conformally flat. The result is that junk radiation is forced into the initial data to account for this unphysical choice. The impact of this junk radiation is not always clear.

A good place to examine junk radiation is in results produced by the evolution of initial data by the Cornell/CalTech collaboration [17]. Their work is so useful due to the very high numerical accuracy they achieve. Cook, an author in [17], kindly provided me with Figs. 8.1 and 8.2 which show the relative difference of the $l = 2$, $m = 2$ and $l = 3$, $m = 2$ waveform amplitudes respectively when comparing their extrapolated numerical results to a 3.5 order post-Newtonian TaylorT4 result. These comparisons are made for a non-spinning equal-mass binary black-hole evolution. For details of the specifics of the numerical and PN methods used to create this see [17] and references there-in. As can be

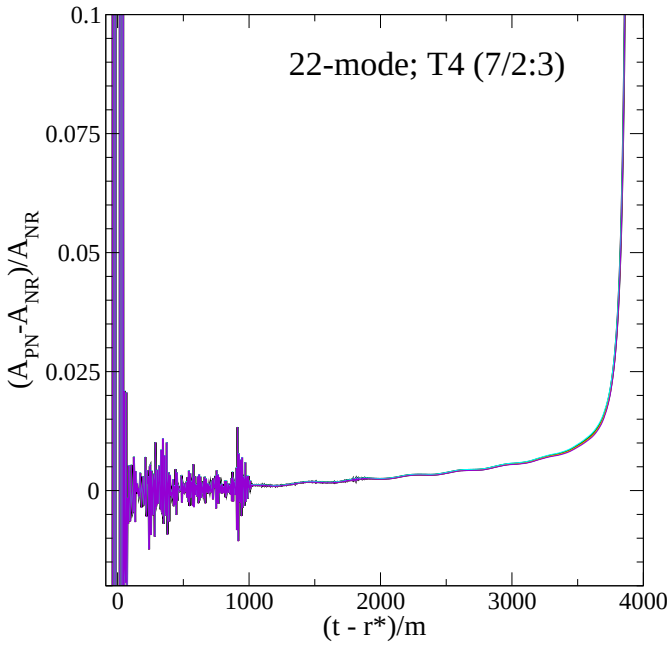

Figure 8.1: Relative difference in amplitude between extrapolated numerical and post-Newtonian models of the two-two mode of radiation. The numerical waveform was found by the Cornell/CalTech collaboration evolutions of binary black holes and the amplitude is compared to a 3.5PN TaylorT4 model.

seen in both figures, the differences are initially dominated by high frequency noise. This is directly related to junk radiation. The end of the simulation also shows a significant deviation between the post-Newtonian and numerical-relativity amplitudes which can be accounted for by the failure of the PN method to model the merger. The two-two mode, being the lowest order allowed mode, tends to dominate the radiation, though recent results [42] show that this is less true as the configurations move away from equal-mass binaries. In terms of the gross-physics seen in the dominant mode, the junk radiation leaves the system in the time it takes radiation to move across the domain, often referred to as the light-crossing time.

This is likely to be accurate enough to aid in the first detections of gravitational waves emitted by binary black holes. However, if we are to understand the physics of sources of gravitational waves in more detail, we will need to better understand the higher order

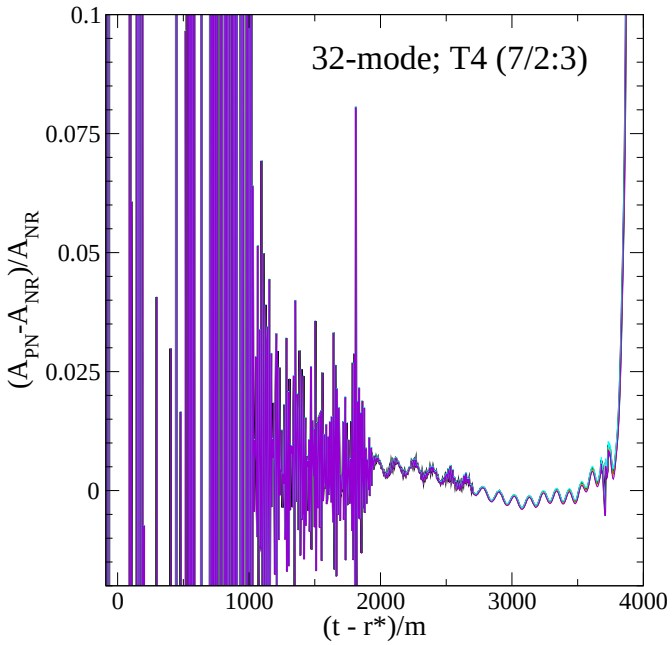

Figure 8.2: Relative difference in amplitude between extrapolated numerical and post-Newtonian models of the three-two mode of radiation. The numerical waveform was found by the Cornell/CalTech collaboration evolutions of binary black holes and the amplitude is compared to a 3.5PN TaylorT4 model.

modes. Figure 8.2 has the same data for the three-two mode and it is clear here that the junk radiation has an impact on the extrapolated wave-form for far longer. So while the issue of junk radiation will not likely inhibit the actual detection of gravitational waves, such a theoretical barrier will likely hinder the development of gravitational wave astronomy as a field. Any method to minimize this junk radiation then would increase the usefulness of numerical relativity simulations.

Cook [31] spent time developing equations to constrain the conformal metric based on ideas first set down by Shibata, Uryu and Friedmann [66] to be used for binary neutron stars which were later implemented in [71]. In applying these ideas to black holes, Cook decided to use excision methods and so he and Baumgarte [31] developed a set of excision boundary conditions. For some time I have been working on implementing these equations and boundary conditions and identifying the numerical and theoretical issues we must ad-

dress in their implementation. This section will have three parts. In the first, I will give an outline of the derivation of the equations to be used on the domain of the problem and on the boundary conditions developed for excision. In the second I will describe the new tools I've used to implement these equations and boundary conditions, particularly a new spectral code called SpEC that we have been allowed to make use of from the Cornell/CalTech collaboration. I will also discuss some details of the implementation itself. Lastly I will report on what results we have found so far and what issues we still face.

8.1 Deriving equations and boundary conditions for the conformal metric

In order to find a constraint for the conformal metric, Cook (following [66]) made use of the trace-free portion of the equation that evolves the extrinsic curvature, Eq. (2.58). Note that the trace of Eq. (2.58) was already used in the ECTS decomposition to create a constraint on the lapse. This enables us to move from choosing the conformal metric to making choices about the dynamics of the extrinsic curvature. There are two parts to this derivation. The first is to rewrite the trace of Eq. (2.58) in terms of the decomposed quantities defined in the extended conformal thin-sandwich approach.

It is helpful to rewrite Eq. (2.58). Here the ∇_i is a spatial derivative, ϵ has been replaced by a minus sign and the matter terms have been dropped:

$$\begin{aligned}\partial_t K_{ij} = &-\nabla_i\nabla_j\alpha + \alpha\left[R_{ij} - 2K_{il}K_j{}^l + KK_{ij}\right] \\ &+ \beta^l\nabla_l K_{ij} + 2K_{l(i}\nabla_{j)}\beta^l. \end{aligned} \tag{8.2}$$

We begin by removing the trace of the equation. Since Eq. 8.2 has two free indices, the following operator can be used:

$$\gamma_i^k\gamma_j^l - \frac{1}{3}\gamma_{ij}\gamma^{kl}. \tag{8.3}$$

The action of this operator on some terms is trivial. When acting on the second derivative

of the lapse, we get

$$-(\nabla_i\nabla_j - \frac{1}{3}\gamma_{ij}\nabla^2)\alpha. \tag{8.4}$$

The spatial Ricci tensor is handled similarly:

$$R_{ij} - \frac{1}{3}\gamma_{ij}R. \tag{8.5}$$

Acting on KK_{ij}, Eq. (8.3) yields KA_{ij}. Similarly $\beta^l\nabla_l K_{ij}$ simply becomes $\beta^l\nabla_l A_{ij}$ as the trace-free operator Eq. (8.3) is made entirely of objects that when acted on by ∇_l return zero. The more difficult terms to deal with are $\partial_t K_{ij}$, $-2K_{il}K_j{}^l$ and $2K_{l(i}\nabla_{j)}\beta^l$. Acting on $\partial_t K_{ij}$, the operator in Eq. (8.3) returns

$$\partial_t A_{ij} + \frac{1}{3}(\gamma_{ij}K_{kl}\partial_t\gamma^{kl} + K\partial_t\gamma_{ij}). \tag{8.6}$$

Recalling the first part of Eq. 3.30 and putting all the pieces together (including the terms $-2K_{il}K_j{}^l$ and $2K_{l(i}\nabla_{j)}\beta^l$ not described here), after considerable algebra, one can arrive at the full trace-free equation:

$$\begin{aligned}\partial_t A_{ij} &= -(\nabla_i\nabla_j - \tfrac{1}{3}\gamma_{ij}\nabla^2)\alpha + \beta^k\nabla_k A_{ij} + 2A_{k(i}\nabla_{j)}\beta^k \\ &\quad + \alpha\left[R_{ij} - \tfrac{1}{3}\gamma_{ij}R - 2A_{ik}A^k_j + \tfrac{1}{3}KA_{ij}\right].\end{aligned} \tag{8.7}$$

Here it is rewritten with the indices up:

$$\begin{aligned}\partial_t A^{ij} &= -(\nabla^i\nabla^j - \tfrac{1}{3}\gamma^{ij}\nabla^2)\alpha + \beta^k\nabla_k A^{ij} - 2A^{k(i}\nabla_k\beta^{j)} \\ &\quad + \alpha\left[R^{ij} - \tfrac{1}{3}\gamma^{ij}R + 2A^i_k A^{jk} + \tfrac{5}{3}KA^{ij}\right].\end{aligned} \tag{8.8}$$

The next step we rewrite Eq. (8.8) in terms of the decompositions used to find the ECTS equations. While this requires considerable algebra, there are no assumptions in this derivation that are any different than those used to derive the ECTS equations as presented in Chapter 3. It will be helpful to write this result alongside the ECTS constraints:

$$\tilde{\nabla}^2\psi - \tfrac{1}{8}\psi\tilde{R} - \tfrac{1}{12}\psi^5K^2 + \tfrac{1}{8}\psi^{-7}\tilde{A}_{ij}\tilde{A}^{ij} = 0, \tag{8.9}$$

$$\tilde{\nabla}_j\tilde{A}^{ij} - \tfrac{2}{3}\psi^6\tilde{\gamma}^{ij}\tilde{\nabla}_j K = 0, \tag{8.10}$$

$$\begin{aligned}\partial_t \tilde{A}^{ij} &= \psi^8\tilde{\alpha}(\tilde{R}^{ij} - \tfrac{1}{3}\tilde{\gamma}^{ij}\tilde{R}) - \left[\tilde{\nabla}^i\tilde{\nabla}^j - \tfrac{1}{3}\tilde{\gamma}^{ij}\tilde{\nabla}^2\right](\psi^8\tilde{\alpha}) \\ &\quad + 8\psi^8\tilde{\alpha}\left[(\tilde{\nabla}^{(i}\ln\psi)\tilde{\nabla}^{j)}\ln(\psi^7\tilde{\alpha}) - \tfrac{1}{3}\tilde{\gamma}^{ij}(\tilde{\nabla}^k\ln\psi)\tilde{\nabla}_k\ln(\psi^7\tilde{\alpha})\right] \\ &\quad + \frac{5}{3}\tilde{A}^{ij}\tilde{\nabla}_k\beta^k + \beta^k\tilde{\nabla}_k\tilde{A}^{ij} - 2\tilde{A}^{k(i}\tilde{\nabla}^{j)}\beta^k + 2\tilde{\alpha}\tilde{A}^i_k\tilde{A}^{jk}, \end{aligned} \tag{8.11}$$

$$\partial_t K = -\psi^{-5}\tilde{\nabla}^2(\psi^7\tilde{\alpha}) + \tfrac{1}{8}\psi^2\tilde{\alpha}\tilde{R} + \tfrac{5}{12}\psi^6\tilde{\alpha}K^2 + \tfrac{7}{8}\psi^{-6}\tilde{\alpha}\tilde{A}_{ij}\tilde{A}^{ij} + \beta^k\tilde{\nabla}_k K. \tag{8.12}$$

Note that all quantities here are defined as in Chapter 3. The second part of the derivation shows how Eq. (8.11) can be treated as a constraint on the inverse conformal metric $\tilde{\gamma}^{ij}$. To do this, Cook applied a reference metric approach.

A reference metric is a non-physical metric, generally chosen because the geometric quantities associated with it (the connection, the Riemann tensor, the Ricci tensor and the Ricci scalar) are known. We then rewrite these geometric quantities for the metric we are studying (in this case the conformal metric) in terms of the difference between them and the reference metric quantities. I will write the reference metric f_{jk} as possessing these properties:

$$f^{ik}f_{jk} = \delta^i_j \tag{8.13}$$

$$\mathring{\nabla}_k f_{ij} \equiv 0. \tag{8.14}$$

Here $\mathring{\nabla}_k$ is defined as the derivative covariant with the reference metric. Immediately, we can find the difference in connections for the conformal metric and the reference metric as

$$\delta\tilde{\Gamma}^k{}_{ij} \equiv \tilde{\Gamma}^k{}_{ij} - \mathring{\Gamma}^k{}_{ij} = \tfrac{1}{2}\tilde{\gamma}^{k\ell}\left[\mathring{\nabla}_i\tilde{\gamma}_{j\ell} + \mathring{\nabla}_j\tilde{\gamma}_{i\ell} - \mathring{\nabla}_\ell\tilde{\gamma}_{ij}\right]. \tag{8.15}$$

Then the following relations are useful:

$$\tilde{\gamma}^{im}\tilde{\gamma}^{jn}\delta\tilde{\Gamma}^k{}_{mn} = -\tfrac{1}{2}\left[\tilde{\gamma}^{i\ell}\mathring{\nabla}_\ell\tilde{\gamma}^{jk} + \tilde{\gamma}^{j\ell}\mathring{\nabla}_\ell\tilde{\gamma}^{ik} - \tilde{\gamma}^{k\ell}\mathring{\nabla}_\ell\tilde{\gamma}^{ij}\right]. \tag{8.16}$$

It is also useful to note the following symmetries and contractions:

$$\mathring{\nabla}_k\tilde{\gamma}_{ij} = 2\delta\tilde{\Gamma}_{(ij)k} \tag{8.17}$$

$$\mathring{\nabla}_k\tilde{\gamma}^{ij} = -2\tilde{\gamma}^{im}\tilde{\gamma}^{jn}\delta\tilde{\Gamma}_{(mn)k} \tag{8.18}$$

$$\delta\tilde{\Gamma}^k{}_{ik} = \tfrac{1}{2}{}_{\mathrm{f}}\nabla_i \ln\tilde{\gamma}. \tag{8.19}$$

As noted previously, the conformal metric has five degrees of freedom: two are dynamical and three are gauge. We have the ability to identify the gauge choice degrees of freedom in the conformal metric via the gauge source functions

$$\begin{aligned} V^k \equiv \tilde{\gamma}^{ij}\delta\tilde{\Gamma}^k{}_{ij} &= \tfrac{1}{2}\tilde{\gamma}^{k\ell}\tilde{\gamma}_{mn}{}_{\mathrm{f}}\nabla_\ell\tilde{\gamma}^{mn} - {}_{\mathrm{f}}\nabla_\ell\tilde{\gamma}^{k\ell} \\ &= -\tfrac{1}{2}\tilde{\gamma}^{k\ell}{}_{\mathrm{f}}\nabla_\ell \ln\tilde{\gamma} - {}_{\mathrm{f}}\nabla_\ell\tilde{\gamma}^{k\ell} \\ &= -\frac{1}{\sqrt{\tilde{\gamma}}}{}_{\mathrm{f}}\nabla_\ell(\sqrt{\tilde{\gamma}}\tilde{\gamma}^{k\ell}). \end{aligned} \tag{8.20}$$

A constant choice of V^k is often referred to as a generalized harmonic gauge.

We are trying to create an elliptic differential equation for the conformal metric which requires second derivatives of the conformal metric. This occurs in two locations: one is when a derivative of the extrinsic curvature is taken and the other is in the Ricci tensor and scalar. The following operator shows up in the Ricci tensor and scalar:

$${}_{\mathrm{f}}\Delta \equiv \tilde{\gamma}^{k\ell}{}_{\mathrm{f}}\nabla_k{}_{\mathrm{f}}\nabla_\ell. \tag{8.21}$$

The following quadratic derivative terms also show up when rewriting the Ricci tensor and scalar:

$$\mathcal{B}^{ij} \equiv \tilde{\gamma}_{mn}\tilde{\gamma}^{k\ell}({}_{\mathrm{f}}\nabla_k\tilde{\gamma}^{im}){}_{\mathrm{f}}\nabla_\ell\tilde{\gamma}^{jn} = \mathcal{B}^{ji} \tag{8.22}$$

$$\mathcal{C}^{ij} \equiv ({}_{\mathrm{f}}\nabla_k\tilde{\gamma}^{i\ell}){}_{\mathrm{f}}\nabla_\ell\tilde{\gamma}^{jk} = \mathcal{C}^{ji} \tag{8.23}$$

$$\begin{aligned} \mathcal{D}^{ij} &\equiv \tilde{\gamma}^{ip}\tilde{\gamma}^{jq}\tilde{\gamma}_{mn}\tilde{\gamma}_{k\ell}({}_{\mathrm{f}}\nabla_p\tilde{\gamma}^{mk}){}_{\mathrm{f}}\nabla_q\tilde{\gamma}^{n\ell} = \mathcal{D}^{ji} \\ &= -\tilde{\gamma}^{ik}\tilde{\gamma}^{j\ell}({}_{\mathrm{f}}\nabla_k\tilde{\gamma}_{mn}){}_{\mathrm{f}}\nabla_\ell\tilde{\gamma}^{mn} \end{aligned} \tag{8.24}$$

$$\mathcal{E}^{ij} \equiv \tilde{\gamma}_{mn}({}_{\mathrm{f}}\nabla_k\tilde{\gamma}^{m(i})\tilde{\gamma}^{j)\ell}{}_{\mathrm{f}}\nabla_\ell\tilde{\gamma}^{kn} = \mathcal{E}^{ji}. \tag{8.25}$$

With these definitions, if we assume a flat reference metric, we can now rewrite the Ricci tensor and scalar respectively as

$$\tilde{R}^{ij} = \tfrac{1}{2}{}_{\mathrm{f}}\Delta\tilde{\gamma}^{ij} + \tilde{\nabla}^{(i}V^{j)} - \tfrac{1}{2}\mathcal{B}^{ij} - \tfrac{1}{2}\mathcal{C}^{ij} + \mathcal{E}^{ij} - \tfrac{1}{4}\mathcal{D}^{ij}, \tag{8.26}$$

and

$$\tilde{R} = -\tfrac{1}{2}{}_{\rm f}\Delta \ln\tilde{\gamma} + \tilde{\nabla}_k V^k + \tfrac{1}{2}\tilde{\gamma}_{k\ell}\left[\mathcal{C}^{k\ell} - \tfrac{1}{2}\mathcal{B}^{k\ell}\right]. \tag{8.27}$$

The above definitions, the result for the difference between connections, and the way the Ricci tensor and scalar have been rewritten provide the necessary tools to rewrite the constraints in Eqs. (8.9) through (8.12). Again, there is considerable algebra in this process. The Hamiltonian constraint becomes

$$\begin{aligned} {}_{\rm f}\Delta\psi - \tfrac{1}{16}\psi\tilde{\gamma}_{ij}(\mathcal{C}^{ij} - \tfrac{1}{2}\mathcal{B}^{ij}) - \tfrac{1}{12}\psi^5 K^2 + \tfrac{1}{8}\psi^{-7}\tilde{\gamma}_{ij}\tilde{\gamma}_{k\ell}\tilde{A}^{ik}\tilde{A}^{j\ell} \\ = V^i{}_{\rm f}\nabla_i\psi + \tfrac{1}{8}\psi\tilde{\nabla}_i V^i - \tfrac{1}{16}\psi_{\rm f}\Delta\ln\tilde{\gamma}, \end{aligned} \tag{8.28}$$

and the momentum constrain is then written as

$$\nabla_j\tilde{A}^{ij} - \tfrac{2}{3}\psi^6\tilde{\gamma}^{ij}{}_{\rm f}\nabla_j K + \tfrac{1}{2}\tilde{A}^{km}\tilde{\gamma}_{k\ell}\tilde{\gamma}_{mn}\tilde{\gamma}^{ij}{}_{\rm f}\nabla_j\tilde{\gamma}^{\ell n} - \tilde{A}^{k\ell}\tilde{\gamma}_{jk}{}_{\rm f}\nabla_\ell\tilde{\gamma}^{ij} = -\tfrac{1}{2}\tilde{A}^{ij}{}_{\rm f}\nabla_j\ln\tilde{\gamma}. \tag{8.29}$$

Eq. (8.12) is rewritten as

$$\begin{aligned} \partial_t K &= -\psi^{-5}{}_{\rm f}\Delta(\psi^7\tilde{\alpha}) + \tfrac{1}{16}\psi^2\tilde{\alpha}\tilde{\gamma}_{ij}(\mathcal{C}^{ij} - \tfrac{1}{2}\mathcal{B}^{ij}) + \tfrac{5}{12}\psi^6\tilde{\alpha}K^2 \\ &\quad + \tfrac{7}{8}\psi^{-6}\tilde{\alpha}\tilde{\gamma}_{ij}\tilde{\gamma}_{k\ell}\tilde{A}^{ik}\tilde{A}^{j\ell} + \beta^i{}_{\rm f}\nabla_i K \\ &\quad + \psi^{-5}V^i{}_{\rm f}\nabla_i(\psi^7\tilde{\alpha}) + \tfrac{1}{8}\psi^2\tilde{\alpha}\tilde{\nabla}_i V^i - \tfrac{1}{16}\psi^2\tilde{\alpha}_{\rm f}\Delta\ln\tilde{\gamma}. \end{aligned} \tag{8.30}$$

Finally, we find Eq. (8.11) is decomposed as

$$\begin{aligned} \partial_t\tilde{A}^{ij} &= \tfrac{1}{2}\psi^8\tilde{\alpha}\left[{}_{\rm f}\Delta\tilde{\gamma}^{ij} - \mathcal{B}^{ij} - \mathcal{C}^{ij} - \tfrac{1}{3}\tilde{\gamma}^{ij}\tilde{\gamma}_{k\ell}\mathcal{C}^{k\ell} + 2\mathcal{E}^{ij} - \tfrac{1}{2}(\mathcal{D}^{ij} - \tfrac{1}{3}\tilde{\gamma}^{ij}\tilde{\gamma}_{k\ell}\mathcal{D}^{k\ell})\right] \\ &\quad - (\tilde{\gamma}^{ik}\tilde{\gamma}^{j\ell} - \tfrac{1}{3}\tilde{\gamma}^{ij}\tilde{\gamma}^{k\ell})\nabla_k{}_{\rm f}\nabla_\ell(\psi^8\tilde{\alpha}) - (\tilde{\gamma}^{\ell(i}{}_{\rm f}\nabla_\ell\tilde{\gamma}^{j)m} - \tfrac{1}{2}\tilde{\gamma}^{\ell m}{}_{\rm f}\nabla_\ell\tilde{\gamma}^{ij})_{\rm f}\nabla_m(\psi^8\tilde{\alpha}) \\ &\quad + 8\psi^8\tilde{\alpha}(\tilde{\gamma}^{k(i}\tilde{\gamma}^{j)\ell} - \tfrac{1}{3}\tilde{\gamma}^{ij}\tilde{\gamma}^{k\ell})(\nabla_k\ln\psi)\nabla_\ell\ln(\psi^7\tilde{\alpha}) \\ &\quad + \tfrac{5}{3}\tilde{A}^{ij}{}_{\rm f}\nabla_k\beta^k + \beta^k{}_{\rm f}\nabla_k\tilde{A}^{ij} - 2\tilde{A}^{k(i}{}_{\rm f}\nabla_k\beta^{j)} + 2\tilde{\alpha}\tilde{A}^i_k\tilde{A}^{jk} \\ &\quad + \tfrac{1}{2}\psi^8\tilde{\alpha}(\tilde{\mathbb{L}}V)^{ij} - \tfrac{1}{3}\tilde{\gamma}^{ij}V^k{}_{\rm f}\nabla_k(\psi^8\tilde{\alpha}) \\ &\quad + \tfrac{1}{6}\psi^8\tilde{\alpha}\tilde{\gamma}^{ij}{}_{\rm f}\Delta\ln\tilde{\gamma} + \tfrac{1}{2}\beta^k\tilde{A}^{ij}{}_{\rm f}\nabla_k\ln\tilde{\gamma}. \end{aligned} \tag{8.31}$$

To complete this decomposition, I must rewrite the definition of the extrinsic curvature:

$$\partial_t\tilde{\gamma}^{ij} = 2\tilde{\alpha}\tilde{A}^{ij} - 2\tilde{\gamma}^{k(i}{}_{\rm f}\nabla_k\beta^{j)} + \tfrac{2}{3}\tilde{\gamma}^{ij}{}_{\rm f}\nabla_k\beta^k + \beta^k{}_{\rm f}\nabla_k\tilde{\gamma}^{ij} + \tfrac{1}{3}\tilde{\gamma}^{ij}\beta^k{}_{\rm f}\nabla_k\ln\tilde{\gamma} = -\tilde{u}^{ij}. \tag{8.32}$$

There are actually two places in Eq. (8.31) where a second derivative is taken of the conformal metric. The first is clearly in the ${}_{\rm f}\Delta\tilde{\gamma}^{ij}$ term while the second shows up when taking a derivative of the conformal traceless extrinsic curvature. It should be noted that the combination of these second derivatives does not necessarily ensure an elliptic operator, rather it depends on the values of $\tilde{\gamma}^{ij}$, β^i and α. In this reference metric decomposition, there are a number of items which are freely specifiable. As before, the quantities $\tilde{u}^{ij} \equiv -\partial_t \tilde{\gamma}^{ij}$, K and $\partial_t K$ are freely specifiable. Since $\tilde{\gamma}^{ij}$ has six elements but only five degrees of freedom, we are free to impose one condition on $\tilde{\gamma}^{ij}$. We take that freedom to be the determinant $\tilde{\gamma}$. We are allowed to impose any condition on the gauge $V^i \equiv \tilde{\gamma}^{ij}\delta\tilde{\Gamma}^k{}_{ij}$ and we must specify $\partial_t \tilde{A}^{ij}$. Lastly, we have already assumed a flat reference metric f_{ij} and continued to use that assumption to arrive at the new constraints. The constrained variables are the conformal factor ψ, the conformal metric $\tilde{\gamma}^{ij}$, the conformal lapse $\tilde{\alpha}$ and the shift β^i.

To do a calculation with these constraints, one needs a set of boundary conditions. As in the past we intend to use these equations with excision to remove the black holes from the domain of computation. For the binary black-holes problem, this means there are two excision boundaries and one outer boundary. Cook and Baumgarte [31] developed a set of excision boundary conditions based on the conformal geometry of the boundary surfaces and on the gauge freedom available in the conformal metric. This discussion is taken directly from that paper.

Three conditions are based on gauge freedom. It's already been mentioned that the vector $V^i \equiv \tilde{\gamma}^{ij}\delta\tilde{\Gamma}^k{}_{ij}$ can be treated as the gauge freedom in the conformal metric. One can then impose

$$V^i = 0 \tag{8.33}$$

on the boundary without changing the physics of the system. This accounts for three degrees of freedom.

While the conformal metric $\tilde{\gamma}_{ij}$ has five degrees of freedom, there are six components

we must specify. Just as we took the determinant of the conformal metric to be a free normalization condition in reference metric equations above, we will apply a determinant condition on the excision boundary here. Let us first write out the form of the conformal spatial metric in a 2+1 decomposition:

$$\tilde{ds} = \Lambda^2 dr^2 + \tilde{h}_{AB}(dx^A + \lambda^A dr)(dx^B + \lambda^B dr). \tag{8.34}$$

Here Λ and λ^A respectively take the role of the lapse and shift in the 3+1 decomposition and $\tilde{h}_{AB}$ is the conformal metric induced on a two-surface. The indices A and B span only 2 and 3. Written this way, the determinant of the conformal spatial metric $\tilde{\gamma}$ can be written in terms of Λ and the determinant of the conformal metric induced on the two surface:

$$\tilde{\gamma} = \Lambda^2 \tilde{h}. \tag{8.35}$$

Now we will demand the determinant of the conformal metric be equal to the determinant of the flat metric $\tilde{\gamma} = f$. Next we can apply the fact that the metric of a two surface is always conformally related to the metric of the surface of a sphere:

$$\tilde{h}_{AB} = \Omega^2 S_{AB}. \tag{8.36}$$

Here Ω is the conformal factor and S_{AB} is the metric of the surface of a sphere. This means

$$\tilde{\gamma} = \Lambda^2 \tilde{h} = \Lambda^2 \Omega^4 S. \tag{8.37}$$

Since $\tilde{\gamma}/f = 1$ and $S = f$, we can conclude

$$\Lambda^2 \Omega^4 = 1 \rightarrow \Omega = \frac{1}{\sqrt{\Lambda}} \tag{8.38}$$

and thus

$$\tilde{h}_{AB} = \frac{1}{\Lambda} S_{AB}. \tag{8.39}$$

Thus we have six conditions on $\tilde{\gamma}_{ij}$ in Eqs. (8.33) and (8.39). It is important to count what conditions have actually been imposed. In Eq. (8.39), three conditions are being imposed. The first is the specification of the determinant of the spatial conformal metric $\tilde{\gamma}$.

This is viewed as a normalization condition. The second and third conditions are choosing the metric of S_{AB} to be that of a sphere. The three gauge choices in Eq. (8.33) then describe how the coordinates move off the sphere. The advantage of these boundary conditions is that they are generally true and do not impose any arbitrary conditions on the physics being modeled.

The boundary conditions on the lapse, shift and conformal factor remain the same quasiequilibrium excision boundary conditions described in Chapter 3. The only changes would be modifications to reflect the non-flat conformal metric.

8.2 Implementation

To implement the new constraints and boundary conditions, I made use of a new pseudo-spectral solver called SpEC. SpEC is a multidomain pseudo-spectral code which is used to solve elliptic and hyperbolic partial differential equations which have smooth solutions on moderately complicated computational geometries. Although primarily developed in order to solve Einstein's equations (the field equations of general relativity), the code can be used to solve a wide range of hyperbolic and elliptic systems. The code is developed by Mark Scheel, Harald Pfeiffer and Larry Kidder who graciously allowed us to make use of it. While SpEC can handle many types of tasks, we were interested in its elliptic solver (described in [62]).

Of immediate value to our work is how easy it is to code equations for SpEC. SpEC was developed so that the user could implement equations to solve without having to understanding the underlying data organization. When implementing a set of equations, the code segment the user would write accesses only a data box which contains the primary variables and their partial derivatives. The user does not have to write code to iterate through the collocation points of the domain but rather only sees tensorial quantities. This means that the code I write very much looks like the equations printed above.

At its heart, the elliptic solver in SpEC is similar to that of Eric. SpEC uses PETSc as its core and the elliptic solver makes uses of the SNES library in SpEC. The solver still treats the solution as a truncated series of functions and the resultant solutions can be completely described by the coefficients of that truncated series. While domain specification is handled with the help of input files, example scripts exist to define a domain and to use a lower resolution solution as the initial guess for a higher resolution solution. SpEC also includes a large set of tools for extracting any measurements we wish from a solution.

In our implementation of the reference metric equations presented above, we decided to artificially decouple the equations for the lapse, shift and conformal factor from the equation for the conformal metric. This allowed us to test the implementation of the constraints for the lapse, shift and conformal factor on their own against previous ECTS implementations. Essentially, we made a two part iterative step. First, the conformal lapse $\tilde{\alpha}$, the shift β^i and the conformal factor ψ would be solved for in what I will call part I. Initially part I would be calculated using a flat conformal metric. Then, the solutions for $\tilde{\alpha}$, β^i and ψ would be used as input data for part II, which would solve for the conformal metric $\tilde{\gamma}^{ij}$. On the next iteration, $\tilde{\gamma}^{ij}$ from the from the previous iteration would be used as input for part I. This would continue until a solution was converged upon.

Lastly, we had to specify the free data. As with the ECTS equations, we took the trace of the extrinsic curvature and its time derivative to be zero $K = \partial_t K = 0$. We chose the reference metric to be flat and we demanded the determinant of the conformal metric be equal to the determinant of the reference metric. This condition eliminates any derivatives of the determinant of the conformal metric present in the reference metric equations. We also chose to set $V^i \equiv \tilde{\gamma}^{ij}\delta\tilde{\Gamma}^k{}_{ij} = 0$ over the whole domain. Initially, in the spirit of quasiequilibrium, we took $\partial_t \tilde{A}^{ij} = 0$ and $\tilde{u}^{ij} \equiv -\partial_t \tilde{\gamma}^{ij} = 0$ in all cases. We later learned that setting $\tilde{u}^{ij}$ to zero means Eq. (8.31) is only elliptic for systems with no rotation.

8.3 Tests and Results

A good starting point for testing these equations to to verify a simple case. The Schwarzschild solution is generally written as

$$ds^2 = -\left(1 - \frac{2M}{r}\right) dt^2 + \frac{dr^2}{1 - 2M/r} + r^2(d\theta^2 + \sin^2\theta d\phi^2). \tag{8.40}$$

However, if one makes the transition to isotropic coordinates $r = \bar{r}(1+M/2\bar{r})$, the Schwarzschild metric can be rewritten as

$$ds^2 = -\left(\frac{1 - M/2\bar{r}}{1 + M/2\bar{r}}\right) dt^2 + \left(1 + \frac{M}{2\bar{r}}\right)^4 [d\bar{r}^2 + \bar{r}^2(d\theta^2 + \sin^2\theta d\phi^2)]. \tag{8.41}$$

It is clear then that the spatial metric can be written to be conformally flat for a single nonspinning black hole. This makes a good trivial test for the constraint on the conformal metric.

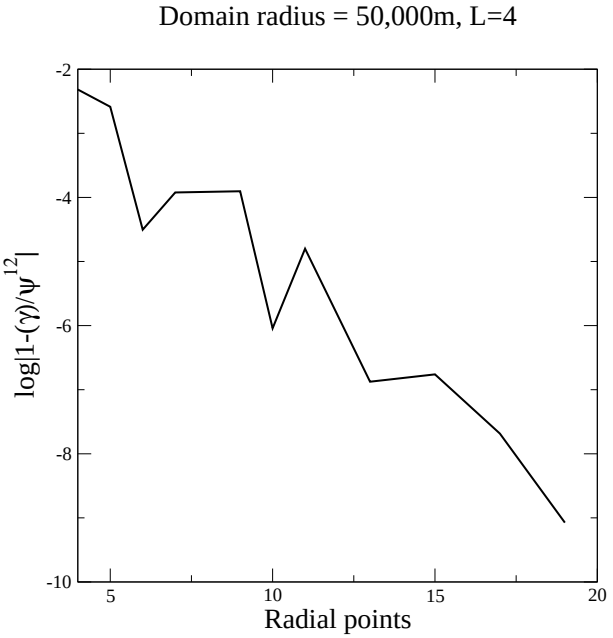

Figure 8.3: Log of the difference between the determinant of the conformal metric and 1 plotted against the number of radial collocation points for a single nonspinning black hole. The outer boundary of the domain for this computation was $r_{outer} \approx 50000 r_{excision}$

We used a single nonspinning black hole as a test case for our condition which normalizes the conformal metric. Since the domain uses topologically Cartesian coordinates,

setting the determinant of the conformal metric equal to the determinant of the flat metric $\tilde{\gamma} = f$ essentially means setting the determinant of the conformal metric to one, $\tilde{\gamma} = 1$. While this condition eliminates terms in the reference metric equations, we do not have the ability to directly impose this condition on a primary variable $\tilde{\gamma}^{ij}$ in SpEC. Figure 8.3 shows the log of the difference of the determinant of the conformal metric from the flat metric. This is plotted against the number of collocation points take radially along a given direction — a partial measure of resolution. These are the results after one iteration of the two part process (one calculation of ψ, β^i and $\tilde{\alpha}$ and one calculation of $\tilde{\gamma}^{ij}$). The outer boundary of the domain was taken at roughly 50,000 times the radius of the excision. The plot is titled with $L = 4$ which parametrizes the angular resolution. The domain decomposition was handled with three concentric spherical shells. Since a single nonspinning black hole is spatially conformally flat, we applied a flat space Dirchelet boundary condition on the excision and outer boundaries. As can be seen, aside from some noise at low resolution, the determinant of the conformal metric seems to be converging to one exponentially with the number of radial collocation points.

The next step for us is to try to model a single spinning black hole, which we know not to be conformally flat. This has proven to be a far harder task. We initially attempted to solve the reference metric equations for a single spinning black hole, using flat Dirchelet boundary conditions on both the excision and on the outer boundary. Though we knew this is not physical, doing this could help identify what issues might arise from the reference metric equations alone. Initially we could not get SpEC to converge on a solution at all. For the first solving of ψ, β^i and $\tilde{\alpha}$ where we assume a flat conformal metric, the reference metric equations reduce to the extended conformal thin-sandwich equations and a solution was arrived at. It was the second part where we had SpEC solve for the conformal metric that would fail. That we had convergence for a Schwarzschild black hole implied there was something about the introduction of rotation to the system that kept it from converging.

The reason for this failure can be found by examining the constraint on the conformal

metric in Eq. (8.31) combined with the definition of the extrinsic curvature Eq. (8.32). There are two terms of interest in Eq. (8.31): one is $\frac{1}{2}\psi^8\tilde{\alpha}_{\rm f}\Delta\tilde{\gamma}^{ij}$ and the other is $\beta^k{}_{\rm f}\nabla_k\tilde{A}^{ij}$. The first term can be rewritten as

$$\frac{1}{2}\psi^8\tilde{\alpha}\tilde{\gamma}^{kl}{}_{\rm f}\nabla_k{}_{\rm f}\nabla_l\tilde{\gamma}^{ij}. \tag{8.42}$$

To understand the second term, one must notice there is a term in the definition of the extrinsic curvature, Eq. (8.32), which is a first derivative of the extrinsic curvature:$-(\beta^k{}_{\rm f}\nabla_k\tilde{\gamma}^{ij})/2\tilde{\alpha}$. When the derivative is taken of the extrinsic curvature and contracted with the shift, we get

$$-\beta^k{}_{\rm f}\nabla_k\beta^l{}_{\rm f}\nabla_l\tilde{\gamma}^{ij} = -\beta^k({}_{\rm f}\nabla_k\frac{\beta^l}{2\tilde{\alpha}}){}_{\rm f}\nabla_l\tilde{\gamma}^{ij} - \frac{\beta^k\beta^l}{2\tilde{\alpha}}{}_{\rm f}\nabla_k{}_{\rm f}\nabla_l\tilde{\gamma}^{ij}. \tag{8.43}$$

The latter of the two terms is a second derivative of the conformal metric, and thus plays a part in determining the elliptic nature of the constraint of the conformal metric, Eq. (8.31). Putting the relevant terms together, we get (with some algebra)

$$\left(\gamma^{kl} - \frac{\beta^k\beta^l}{\alpha^2}\right){}_{\rm f}\nabla_k{}_{\rm f}\nabla_l\tilde{\gamma}^{ij} + ... \tag{8.44}$$

Recall that we impose the $\beta^i = (\mathbf{\Omega}\times\mathbf{r})^i|_{r\to\infty}$ on the outer boundary. Since this is difficult to implement numerically, in practice, we create a change of variables and subtract $(\mathbf{\Omega}\times\mathbf{r})^i$ from the shift over the whole domain. The problem is that this term is negligible at the excision boundary and grows to dominate as one moves away from the axis of rotation. Since, γ^{kl}'s diagonal terms are expected to be positive over the whole domain, this means the diagonal terms of

$$\left(\gamma^{kl} - \frac{\beta^k\beta^l}{\alpha^2}\right) \tag{8.45}$$

will change from positive value to negative value at some distance from the axis of rotation. Thus Eq. (8.45) is not positive definite, meaning the equation constraining the conformal metric, Eq. (8.31), is not generally an elliptic operator over the whole domain.

Indeed, we found that if we shrank the domain such that the outer radius was smaller than the inverse of the magnitude of $\mathbf{\Omega}_0$, SpEC would converge on a solution for the conformal metric. In particular, we created data with $\mathbf{\Omega}_0 = 0.002\hat{z}$ and set an outer radius only

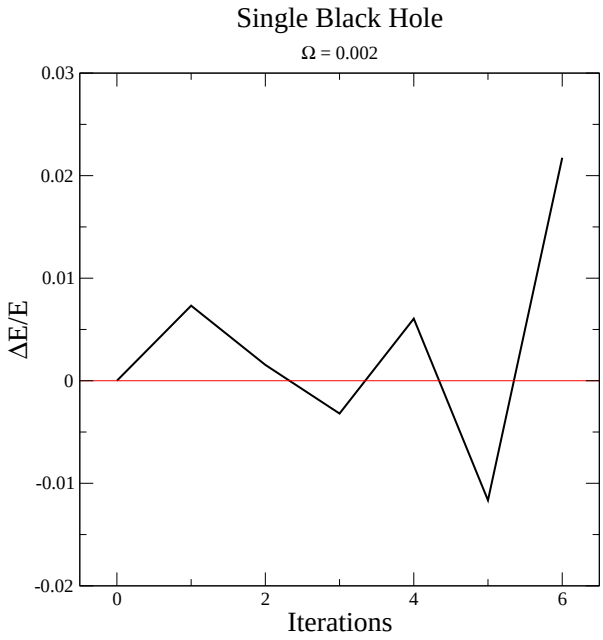

Figure 8.4: Change in the ADM energy for a single spinning black hole over several iterations of solving for the conformal metric. Flat boundary conditions were used and the outer radius was chosen to be less than the inverse of the orbital angular velocity

four-hundred times the excision surface and found the code to converge. As an initial test of results, I ran several iterations of solving for the conformal metric, then solving for the lapse, shift and conformal factor. If doing this would cause the initial data to shed junk radiation, one would expect the ADM energy to decrease over the iterations. Figure 8.4 plots the change in energy at each iteration divided by the ADM energy. This calculation was done with fifteen radial collocation points along an angular direction and we used $L = 14$ to parametrize the angular resolution. As can be seen, the change in energy is less than zero at only two iterations in the process. There are at least two possible reasons for this. One is that an outer boundary at four-hundred times the excision radius is not far enough out. Thus it is necessary to find a way to make Eq. (8.31) generally elliptic. The second reason is that we are still imposing an unrealistic Dirchelet condition on the excision boundary.

To resolve the first issue, we reconsidered the choices we made for some of the freely specifiable data, particularly the dynamic choice for the conformal metric $\tilde{u}^{ij} = -\partial_t \tilde{\gamma}^{ij}$. $\tilde{u}^{ij}$

only appears in the definition of the extrinsic curvature, and the problem arises when we take a derivative of the extrinsic curvature. If we were to set $\tilde{u}^{ij} = -\tilde{\gamma}^{k(i}\tilde{\nabla}_k(\mathbf{\Omega}_0 \times \mathbf{r})^{j)} + \frac{2}{3}\tilde{\gamma}^{ij}\tilde{\nabla}_k(\mathbf{\Omega}_0 \times \mathbf{r})^k$ [66], this would remove any rotational part of the shift from the definition of the extrinsic curvature. When we tried this with an outer boundary many orders of magnitude larger, SpEC was again able to converge on a solution for the conformal metric. This was still using a Dirchelet boundary condition on the excision, which we knew to be incorrect.

The next step then was to implement the boundary conditions for the conformal metric on the excision described in Section 8.1. Doing so again results in SpEC being unable to converge on a solution. This problem currently remains unsolved. There is, though, at least one line of thought I feel is worth further investigation.

Output on failed attempts to find a solution for the conformal metric at this point shows noticeable violation of our gauge choice for the conformal metric $V^i \equiv \tilde{\gamma}^{ij}\delta\tilde{\Gamma}^k{}_{ij}$. As with the determinant of the conformal metric, the gauge choice cannot be directly imposed on $\tilde{\gamma}^{ij}$, but rather used only as an assumption imposed on the constraint equations. In particular, when this vector is measured, it has noticeable magnitude along the axis of rotation of the single black hole. Initially, we had developed an additional set of equations to enact a coordinate transformation on the conformal metric to enforce $V^i = 0$. The equations would act on a vector ξ^i, which defines the change of coordinates via $x^i \to x^i + \xi^i$. ξ^i would be set to zero on the boundary. When this did not work, examination of the raw numerical data showed that V^i differed from zero the most on the excision boundary. Thus, applying an arbitrary choice of ξ^i on the boundary stopped us from finding a coordinate transformation, that would satisfy our gauge choice. It is not surprising that the gauge violation is focused on the excision boundary, and this fits since we could find solutions for $\tilde{\gamma}^{ij}$ when using Dirchelet boundary conditions. In fact, when examining previous data for the conformal metric found using the Dirchelet boundary conditions, I found there was still gauge violation along the axis of rotation. This means that the previous results for the

conformal metric were not solutions to Einstein's equations at all (except in the nonspinning case where this didn't occur).

A possible solution to this may exist in only calculating three elements of the conformal metric, and using the gauge condition $V^i = 0$, to reconstruct the rest of the conformal metric. This route presents a number of difficulties primarily concerned with the choice of which components of the conformal metric to actually impose Eq. 8.31 on. In this case, we would drop the gauge boundary condition, and only use the condition requiring the conformal metric be conformally equivalent to a sphere. At this point, I have not fully considered the difficulties of implementing the equations to do this, however it remains a possibility to finding a way to make these reference metric equations work.

8.4 Discussion

As of yet, we have not found a way to use the reference metric equations and excision boundary conditions described in this chapter to converge on solutions of Einstein's equations for any but the most trivial case: a single nonspinning black hole. However, finding a solution to the difficulties we have found in implementing these equations holds the promise of cutting down the junk radiation found in conformally flat initial data for binary black holes. Thus this research remains a worthy area of study, that I will continue to give my attention to.

Chapter 9

Conclusion

The primary motivation of this work is the analysis and improvement of initial data for the binary black-hole problem. The goal is to allow for a better ability to predict the physics that will show up in numerical evolutions. This in turn better enables researchers to study binary black holes for the purpose of gravitational-wave detection. With this in mind, I will discuss how the work presented in this dissertation fulfills its motivation and recount areas for further research.

LIGO will only be able to detect binary black holes starting near the very end of their inspiral. At this point in the orbit, the black holes are expected to be in an adiabatic inspiral where the orbit's period is small compared to the time required for a noticeable change in separation. To that end, we tested two established methods for predicting quasicircular orbits in initial data with the extended conformal thin-sandwich decomposition. They were found to agree well with each other and to create series of data that conform well to a thermodynamic identity for stationary systems. It has since been found that perhaps these quasicircular orbits we find in ECTS initial data are perhaps a little *too circular*. In Ref. [17] it was found that small eccentricities showed up in evolutions of these kinds of initial data. It was found that adding a small ammount of inward radial velocity would smooth out the inspiral.

We further found that some assumptions we had about spin were not correct. We

implemented a method that would find a given value of spin using root-finding. Perhaps more useful though was what we determined about the spin angular velocities. Using the Kerr formula for spin, we found the lowest order assumption for spin angular velocity of corotating black holes ($\Omega_r = \Omega_0$) did not agree well with our quasilocal measures of spin. Instead, a higher order approximation was found to better fit the numerical data. When I studied eccentricity, the correction to the spin angular velocity was applied in using our post-Newtonian definitions of eccentricity. When measuring the eccentricity of our Komar sequences and minima of effective potentials, using the correction for the spin angular velocity resulted in eccentricities closer to zero.

LISA holds the promise of being able to detect gravitational waves (GWs) emitted by binary black holes well before merger. In such a case, the detection of GWs from binaries that have not radiated away all the eccentricity may be possible. It may also be possible for BBH's to meet without first going through a long circularizing inspiral. Thus we examined eccentricity in all our initial data. We found that at larger separations, the Komar-mass difference could provide a tool for parameterizing eccentric orbits. Examining this led us to a theoretical question about low angular momentum orbits. It would be interesting, and further develop our knowledge of a fundamental problem of general relativity to find out what would happen if we evolve numerical initial data taken from a pericenter configuration for which there were no corresponding apocenter configuration (at the same binding energy) in an effective potential.

Lastly we have worked on solving a common problem for numerical initial data in the binary black-hole problem: that of conformal flatness. The junk radiation in numerical simulations due to conformally flat initial data is not likely to hinder the ability to detect gravitational waves emitted by binary black holes. However, if such detections occur, we will want to be able to move towards using gravitational waves to learn something about the physics of the sources. For binary black holes, that is very limited when only using data with junk radiation. The reference metric equations and the excision boundary conditions

made for them represent a chance at decreasing the junk radiation present in initial data.

The efforts presented in this dissertation represent a small step along the way to a better theoretical understanding of the physics of binary black holes. During my time as a student at Wake Forest University, the first evolutions which follow black holes during the end of their spiral and through the merger were successfully executed [64, 21, 6]. Since then, an enormous amount of work has gone into understanding the late stage of inspiral and merger. Hopefully, my own research will help our understanding of this phenomena and aid in the eventual detection of gravitational waves.

Appendix A

Komar sequences for corotating and nonspinning binaries

In this appendix I present the numerical data for equal-mass corotating and equal-mass nonspinning black holes in circular orbit as defined by the Komar-mass ansatz. The assumptions of conformal flatness and maximal slicing were used in this data as well as the lapse boundary condition on the excisions,

$$\left.\frac{d\alpha\psi}{dr}\right|_{\mathcal{S}} = \left.\frac{\alpha\psi}{2r}\right|_{\mathcal{S}}. \tag{A.1}$$

The data is scaled relative to the total and reduced masses (m and μ) defined with respect to the irreducible mass of the apparent horizons $M_{\rm irr}$.

In table A.1, d and Ω_0 are, respectively, the separation of the centers of the excised regions and the orbital angular velocity measured in "coordinate units". These values for d and Ω, together with the coordinate radius of the excision sphere $r = 0.7857981371$, provide all parameters necessary to reproduce the data in Table A.1. The remaining quantities are dimensionless. $m\Omega_0$ is the orbital angular velocity of the binary system as measured at infinity. E_b/μ is the dimensionless binding energy of the system with E_b defined as $E_b \equiv E_{\rm ADM} - m$. $J/\mu m$ is the dimensionless total ADM angular momentum of the binary system as measured at infinity. ℓ/m is the dimensionless proper separation between the two excision surfaces as measured on the initial-data slice.[1] Finally, $S_z/M_{\rm irr}^2$ and $S_K/M_{\rm irr}^2$

[1]Note that the value of ℓ listed in Tables IV and V of Ref. [33] were in error. The corrected values for

are two measures of the dimensionless spin of one of the black holes. S_z is defined using the flat-space Killing vector and S_K is defined using the approximate Killing vector. For the nonspinning case (table A.2), S_K is not reported as it is zero by construction and f_r is given instead.

the corotating case, and correct values for the "true" non-spinning case, are given in the following tables.

Table A.1: Sequence of corotating equal-mass black holes on circular orbits satisfying the Komar ansatz. The ISCO is at separation $d \sim 8.28$.

d	Ω_0	$m\Omega_0$	E_b/μ	$J/\mu m$	ℓ/m	$S_z/M_{\rm irr}^2$	$S_K/M_{\rm irr}^2$
40	0.0052966	0.01090	-0.0233183	4.9120	22.87	0.02148	0.02150
35	0.0064212	0.01327	-0.0263265	4.6620	20.23	0.02609	0.02612
30	0.0080083	0.01665	-0.0301930	4.4019	17.58	0.03264	0.03267
29	0.0084050	0.01750	-0.0311008	4.3488	17.04	0.03428	0.03431
28	0.0088354	0.01842	-0.0320622	4.2953	16.51	0.03606	0.03610
27	0.0093039	0.01943	-0.0330816	4.2414	15.97	0.03800	0.03804
26	0.0098151	0.02054	-0.0341642	4.1872	15.43	0.04012	0.04017
25	0.010375	0.02175	-0.0353153	4.1328	14.89	0.04245	0.04250
24	0.010990	0.02309	-0.0365409	4.0781	14.35	0.04501	0.04507
23	0.011667	0.02457	-0.0378476	4.0233	13.81	0.04785	0.04791
22	0.012418	0.02622	-0.0392423	3.9684	13.26	0.05099	0.05106
21	0.013252	0.02806	-0.0407325	3.9135	12.72	0.05449	0.05457
20	0.014183	0.03012	-0.0423262	3.8587	12.17	0.05841	0.05850
19	0.015227	0.03245	-0.0440313	3.8043	11.62	0.06282	0.06293
18	0.016406	0.03511	-0.0458555	3.7503	11.06	0.06782	0.06794
17	0.017744	0.03814	-0.0478056	3.6971	10.50	0.07352	0.07366
16	0.019273	0.04164	-0.0498857	3.6450	9.943	0.08007	0.08024
15	0.021031	0.04571	-0.0520956	3.5944	9.377	0.08765	0.08785
14.5	0.022012	0.04800	-0.0532470	3.5699	9.092	0.09190	0.09212
14	0.023070	0.05049	-0.0544267	3.5460	8.807	0.09650	0.09674
13.5	0.024215	0.05320	-0.0556310	3.5229	8.520	0.1015	0.1018
13	0.025456	0.05617	-0.0568549	3.5006	8.231	0.1070	0.1073
12.5	0.026804	0.05942	-0.0580912	3.4793	7.941	0.1129	0.1132
12	0.028273	0.06300	-0.0593298	3.4592	7.649	0.1195	0.1198
11.5	0.029877	0.06696	-0.0605565	3.4405	7.356	0.1266	0.1271
11	0.031634	0.07135	-0.0617523	3.4234	7.060	0.1346	0.1350
10.5	0.033564	0.07625	-0.0628909	3.4082	6.762	0.1434	0.1439
10	0.035689	0.08174	-0.0639364	3.3952	6.462	0.1532	0.1538
9.5	0.038037	0.08792	-0.0648401	3.3848	6.159	0.1642	0.1649
9	0.040638	0.09493	-0.0655348	3.3775	5.853	0.1765	0.1773
8.9	0.041191	0.09644	-0.0656410	3.3765	5.792	0.1792	0.1800
8.8	0.041757	0.09800	-0.0657345	3.3756	5.731	0.1819	0.1828
8.7	0.042334	0.09960	-0.0658142	3.3749	5.669	0.1847	0.1856
8.6	0.042923	0.1012	-0.0658791	3.3744	5.607	0.1876	0.1885
8.5	0.043526	0.1029	-0.0659282	3.3740	5.545	0.1905	0.1915
8.4	0.044141	0.1047	-0.0659603	3.3738	5.483	0.1936	0.1945
8.35	0.044453	0.1055	-0.0659695	3.3737	5.451	0.1951	0.1961
8.3	0.044769	0.1064	-0.0659741	3.3738	5.420	0.1967	0.1977
8.25	0.045089	0.1074	-0.0659738	3.3738	5.389	0.1982	0.1993
8.2	0.045412	0.1083	-0.0659685	3.3739	5.358	0.1998	0.2009
8.1	0.046068	0.1102	-0.0659419	3.3743	5.295	0.2031	0.2042
8	0.046738	0.1121	-0.0658929	3.3748	5.232	0.2065	0.2076

Table A.2: Sequence of non-spinning equal-mass black holes on circular orbits satisfying the Komar ansatz. The ISCO is at separation $d \sim 7.55$.

d	Ω_0	f_r	$m\Omega_0$	E_b/μ	$J/\mu m$	ℓ/m	$S_z/M_{\rm irr}^2$
40	0.0052973	0.9551	0.01090	-0.0235329	4.8717	22.87	-0.00004206
35	0.0064225	0.9485	0.01327	-0.0266396	4.6136	20.24	-0.00005974
30	0.0080108	0.9396	0.01665	-0.0306751	4.3423	17.58	-0.00008963
29	0.0084079	0.9374	0.01750	-0.0316304	4.2864	17.05	-0.00009813
28	0.0088388	0.9351	0.01843	-0.0326458	4.2298	16.51	-0.0001077
27	0.0093079	0.9326	0.01943	-0.0337268	4.1727	15.98	-0.0001187
26	0.0098198	0.9299	0.02054	-0.0348800	4.1150	15.44	-0.0001312
25	0.010380	0.9270	0.02175	-0.0361122	4.0568	14.90	-0.0001458
24	0.010996	0.9238	0.02309	-0.0374317	3.9979	14.36	-0.0001627
23	0.011676	0.9203	0.02457	-0.0388473	3.9386	13.82	-0.0001825
22	0.012428	0.9165	0.02622	-0.0403693	3.8786	13.27	-0.0002058
21	0.013264	0.9123	0.02806	-0.0420092	3.8182	12.73	-0.0002336
20	0.014198	0.9077	0.03013	-0.0437799	3.7574	12.18	-0.0002669
19	0.015247	0.9025	0.03246	-0.0456957	3.6962	11.63	-0.0003072
18	0.016431	0.8967	0.03512	-0.0477726	3.6348	11.07	-0.0003567
17	0.017775	0.8903	0.03816	-0.0500280	3.5732	10.52	-0.0004180
16	0.019313	0.8829	0.04166	-0.0524802	3.5118	9.957	-0.0004952
15	0.021085	0.8745	0.04574	-0.0551473	3.4509	9.393	-0.0005940
14.5	0.022075	0.8698	0.04804	-0.0565665	3.4207	9.110	-0.0006539
14	0.023143	0.8647	0.05053	-0.0580448	3.3907	8.825	-0.0007226
13.5	0.024300	0.8593	0.05326	-0.0595830	3.3612	8.539	-0.0008020
13	0.025556	0.8533	0.05623	-0.0611807	3.3321	8.252	-0.0008942
12.5	0.026923	0.8469	0.05950	-0.0628363	3.3036	7.963	-0.001002
12	0.028415	0.8399	0.06310	-0.0645457	3.2758	7.673	-0.001129
11.5	0.030047	0.8321	0.06709	-0.0663017	3.2490	7.381	-0.001279
11	0.031840	0.8236	0.07151	-0.0680922	3.2233	7.087	-0.001460
10.5	0.033815	0.8142	0.07645	-0.0698984	3.1991	6.791	-0.001678
10	0.035998	0.8036	0.08200	-0.0716907	3.1766	6.493	-0.001946
9.5	0.038420	0.7918	0.08826	-0.0734242	3.1565	6.193	-0.002277
9	0.041118	0.7785	0.09538	-0.0750303	3.1393	5.891	-0.002693
8.5	0.044133	0.7632	0.1035	-0.0764029	3.1258	5.585	-0.003226
8	0.047516	0.7457	0.1129	-0.0773785	3.1172	5.277	-0.003920
7.9	0.048241	0.7419	0.1150	-0.0775054	3.1162	5.215	-0.004084
7.8	0.048984	0.7379	0.1171	-0.0776039	3.1154	5.153	-0.004257
7.7	0.049745	0.7338	0.1193	-0.0776711	3.1149	5.090	-0.004442
7.65	0.050132	0.7318	0.1204	-0.0776920	3.1148	5.059	-0.004538
7.6	0.050524	0.7296	0.1216	-0.0777037	3.1148	5.028	-0.004637
7.55	0.050921	0.7275	0.1227	-0.0777058	3.1148	4.996	-0.004740
7.5	0.051323	0.7253	0.1239	-0.0776980	3.1149	4.965	-0.004846
7.4	0.052140	0.7208	0.1263	-0.0776501	3.1154	4.902	-0.005067
7.3	0.052978	0.7161	0.1288	-0.0775557	3.1163	4.839	-0.005304

Appendix B

Post-Newtonian Equations for Energy and Angular Momentum

The post-Newtonian equations we used for the results in section 7 are described here-in. These are taken directly out of [59]. While these are not the all the forms provided, these are the ones we found most useful. The 3rd order conservative equation for energy is

$$\begin{aligned} E_{\rm ADM}/\mu = -\frac{1}{2}(1-\epsilon^2)\zeta\Big\{1 - \left[\frac{3}{4} + \frac{1}{12}\eta - \left(\frac{1}{12} - \frac{1}{4}\eta\right)\epsilon^2\right]\zeta \\ - \left[\frac{27}{8} - \frac{19}{8}\eta + \frac{1}{24}\eta^2 - \left(\frac{17}{12} + \frac{7}{4}\eta + \frac{1}{4}\eta^2\right)\epsilon^2 \left(\frac{1}{24} + \frac{11}{24}\eta - \frac{1}{8}\eta^2\right)\epsilon^4\right]\zeta^2 \\ - \Big[\frac{675}{64} - \left(\frac{34445}{576} - \frac{205}{96}\pi^2\right)\eta + \frac{155}{96}\eta^2 + \frac{35}{5184}\eta^3 \\ + \left(\frac{7}{64} + \left(\frac{167}{64} - \frac{41}{96}\pi^2\right)\eta + \frac{7595}{864}\eta^2 - \frac{25}{576}\eta^3\right)\epsilon^2 \\ - \left(\frac{815}{576} - \frac{6995}{1728}\eta - \frac{299}{288}\eta^2 - \frac{25}{64}\eta^3\right)\epsilon^4 - \left(\frac{35}{5184} - \frac{31}{192}\eta + \frac{13}{32}\eta^2 - \frac{5}{64}\eta^3\right)\epsilon^6\Big]\zeta^3\Big\} \end{aligned} \tag{B.1}$$

and for angular momentum is

$$\begin{aligned} J_{\rm ADM}/\mu m = \frac{1}{\sqrt{\zeta}}\Big\{1 + \left[\frac{3}{2} + \frac{1}{6}\eta - \left(\frac{1}{6} - \frac{1}{2}\eta\right)\epsilon^2\right]\zeta \\ + \left[\frac{27}{8} - \frac{19}{8}\eta + \frac{1}{24}\eta^2 + \left(\frac{23}{12} - \frac{35}{12}\eta - \frac{1}{4}\eta^2\right)\epsilon^2 + \left(\frac{1}{24} - \frac{17}{24}\eta - \frac{1}{8}\eta^2\right)\epsilon^4\right]\zeta^2 \\ + \Big[\frac{135}{16} - \left(\frac{6889}{144} - \frac{41}{24}\pi^2\right)\eta + \frac{31}{24}\eta^2 + \frac{7}{1296}\eta^3 \\ + \left(\frac{299}{16} - \left(\frac{1025}{16} - \frac{41}{24}\pi^2\right)\eta + \frac{2077}{216}\eta^2 - \frac{5}{144}\eta^3\right)\epsilon^2 \\ + \left(\frac{77}{144} - \frac{1337}{432}\eta + \frac{271}{72}\eta^2 + \frac{5}{16}\eta^3\right)\epsilon^4 - \left(\frac{7}{1296} - \frac{7}{48}\eta + \frac{3}{8}\eta^2 - \frac{1}{16}\eta^3\right)\epsilon^6\Big]\zeta^3\Big\}. \end{aligned} \tag{B.2}$$

Here, ϵ is the eccentricity, ζ is the inverse semilatus rectum and $\eta = \mu/m$ or the reduced mass divided by the sum of the black-hole masses. These equations for energy and angular momentum make use of the conventional definitions of eccentricity and the inverse semilatus rectum respectively.

$$\epsilon \equiv \frac{\sqrt{\Omega_p} - \sqrt{\Omega_a}}{\sqrt{\Omega_p} + \sqrt{\Omega_a}} \tag{B.3}$$

$$\zeta \equiv \left(\frac{\sqrt{m\Omega_p} + \sqrt{m\Omega_a}}{2} \right)^{(4/3)} \tag{B.4}$$

Here, Ω is the orbital angular velocity and the subscripts refer to pericenter and apocenter of an orbit. By combining definitions, it can be shown that the inverse semilatus rectum can be rewritten

$$\zeta = \left(\frac{m\Omega_p}{(1+\epsilon)^2} \right)^{(2/3)} = \left(\frac{m\Omega_a}{(1-\epsilon)^2} \right)^{(2/3)} \tag{B.5}$$

It should be noted these equations are written assuming zero spin. To include spin effects, the following terms are needed for the energy and angular momentum equations respectively.

$$\begin{aligned} E(\epsilon, \zeta, \omega) &= E_{\mathrm{ADM}}(\epsilon, \zeta) + E_{\mathrm{self}}(\epsilon, \zeta, \omega) \\ &\quad + E_{\mathrm{N,Corr}}(\epsilon, \zeta, \omega) + E_{\mathrm{Spin}}(\epsilon, \zeta, \omega) \end{aligned} \tag{B.6}$$

$$\begin{aligned} J(\epsilon, \zeta, \omega) &= J_{\mathrm{ADM}}(\epsilon, \zeta) + S(\epsilon, \zeta, \omega) \\ &\quad + J_{\mathrm{N,Corr}}(\epsilon, \zeta, \omega) + J_{\mathrm{Spin}}(\epsilon, \zeta, \omega) \end{aligned} \tag{B.7}$$

In these equations ω represents the spin angular velocities of the black holes[1]. The self energy and spin terms (E_{self} and S) are derived as expansions of the Kerr formulas relating mass, spin, and rotational angular velocity. The Newtonian correction terms ($E_{\mathrm{N,Corr}}$ and $J_{\mathrm{N,Corr}}$) stem from the conversion of total mass to irreducible mass and the "Spin" terms (E_{Spin} and J_{Spin}) represent spin-orbit effects. These additional terms can be found in [11]

[1]We use a single parameter ω for simplicity. In general, specifying the spin of two black holes would require six parameters.

and I provide them here for completeness.

$$E_{\rm self} = m_{irr}\left[\frac{1}{2}(m_{irr}\omega)^2 + \frac{3}{8}(m_{irr}\omega)^4 + ...\right] \tag{B.8}$$

$$S = m_{irr}^3\omega\left[1 + \frac{1}{2}(m_{irr}\omega)^2 + \frac{3}{8}(m_{irr}\omega)^4 + ...\right] \tag{B.9}$$

$$E_{\rm N,Corr} = -\frac{5}{48}m_{irr}(1-\epsilon^2)(m_{irr}\omega)^2\zeta \tag{B.10}$$

$$J_{\rm N,Corr} = \frac{5}{24}m_{irr}^2(m_{irr}\omega)^2/\sqrt{\zeta} \tag{B.11}$$

$$E_{\rm Spin} = -\frac{1}{12}m_{irr}(1-\epsilon^2)(7-2\epsilon^2)(m_{irr}\omega)\zeta^{(5/2)} \tag{B.12}$$

$$J_{\rm Spin} = -\frac{5}{24}m_{irr}^2(7+\epsilon^2)(m_{irr}\omega)\zeta \tag{B.13}$$

These terms have to be applied for each black hole. In these equations, m_{irr} is the irreducible mass of the black hole in question and ω is the spin angular velocity of the individual black hole.

Bibliography

[1] Kashif Alvi. Approximte binary-black-hole metric. *Phys. Rev. D*, 61:124013, May 2000.

[2] R. Arnowitt, S. Deser, and Charles W. Misner. The dynamics of general relativity. In L. Witten, editor, *Gravitation: An Introduction to Current Research*, pages 227–265. Wiley, New York, 1962.

[3] Abhay Ashtekar, Christopher Beetle, Olaf Dreyer, Stephen Fairhurst, Badri Krishnan, Jerzy Lewandowski, and Jacek Wiśniewski. Generic isolated horizons and their applications. *Phys. Rev. Lett.*, 85:3564–3567, October 2000.

[4] Abhay Ashtekar and Badri Krishnan. Dynamical horizons and their properties. *Phys. Rev. D*, 68:104030, 2003.

[5] Abhay Ashtekar and Badri Krishnan. Isolated and dynamical horizons and their applications. *Living Rev. Relativity*, 7(10), 2004. http://www.livingreviews.org/lrr-2004-10.

[6] John G. Baker, Joan Centrella, Dae Il Choi, Michael Koppitz, and James van Meter. Gravitational-wave extraction from an inspiraling configuration of merging black holes. *Phys. Rev. Lett.*, 96:111102, 2006.

[7] Satish Balay, William D. Gropp, Lois C. McInnes, and Barry F. Smith. Efficienct management of parallelism in object oriented numerical software libraries. In E. Arge, A. M. Bruaset, and H. P. Langtangen, editors, *Modern Software Tools in Scientic Computing*, pages 163–202. Birkhauser Press, 1997.

[8] Satish Balay, William D. Gropp, Lois C. McInnes, and Barry F. Smith. Petsc home page. http://www.mcs.anl.gov/petsc, 2008.

[9] Satish Balay, William D. Gropp, Lois C. McInnes, and Barry F. Smith. Petsc users manual. Technical Report ANL-95/11 - Revision 3.0, Argonne National Laboratory, 2008.

[10] Thomas W. Baumgarte. Innermost stable circular orbit of binary black holes. *Phys. Rev. D*, 62:024018, July 2000.

[11] Emanuele Berte, Sai Iyer, and Clifford M. Will. Eccentricity content of binary black hole initial data. *Phys. Rev. D*, 74:061503(R), 2006.

[12] James Kent Blackburn and Steven Detweiler. Close black-hole binary systems. *Phys. Rev. D*, 46:2318–2333, September 1992.

[13] Jeffery M. Bowen. *Initial Value Problem on Non-Euclidean Topologies.* PhD thesis, University of North Carolina, 1979.

[14] Jeffrey M. Bowen. General form for the longitudinal momentum of a spherically symmetric source. *Gen. Relativ. Gravit.*, 11:227–231, 1979.

[15] Jeffrey M. Bowen. General solution for flat-space longitudinal momentum. *Gen. Relativ. Gravit.*, 14:1183–1191, 1982.

[16] Jeffrey M. Bowen and James W. York, Jr. Time-asymmetric initial data for black holes and black-hole collisions. *Phys. Rev. D*, 21:2047–2056, April 1980.

[17] Michael Boyle, Duncan A. Brown, Lawrence E. Kidder, Abdul H. Mroue, Harald P. Pfeiffer, Mark A. Scheel, Gregory B. Cook, and Saul A. Teukolsky. High-accuracy comparison of numerical relativity simulations with post-newtonian expansions. *Phys. Rev. D*, 76:124038, 2007.

[18] Steven Brandt and Bernd Brügmann. A simple construction of initial data for multiple black holes. *Phys. Rev. Lett.*, 78:3606–3609, May 1997.

[19] J. David Brown and James W. York, Jr. Quasilocal energy and conserved charges derived from the gravitational action. *Phys. Rev. D*, 47:1407–1419, 1993.

[20] Bernd Brügmann, Jose A. Gonzalez, Mark Hannam, Sascha Husa, Ulrich Sperhake, and Wolfgang Tichy. Calibration of moving puncture simulations. 2006. gr-qc/0610128.

[21] Manuela Campanelli, Carlos O. Lousto, Pedro Marronetti, and Yosef Zlochower. Accurate evolutions of orbiting black-hole binaries without excision. *Phys. Rev. Lett.*, 96:111101, 2006.

[22] Matthew Caudill, Gregory B. Cook, Jason D. Grigsby, and Harald P. Pfeiffer. Circular orbits and spin in black-hole initial data. *Phys. Rev. D*, 74:064011, 2006.

[23] Matthew W. Choptuik and William G. Unruh. An introduction to the multi-grid method for numerical relativists. *Gen. Relativ. Gravit.*, 18:813–843, August 1986.

[24] Demetrios Christodoulou. Reversible and irreversible transformations in black-hole physics. *Phys. Rev. Lett.*, 25:1596–1597, November 1970.

[25] Greg Cook. Private Communication.

[26] Gregory B. Cook. *Initial Data for the Two-Body Problem of General Relativity.* PhD thesis, University of North Carolina, 1990.

[27] Gregory B. Cook. Initial data for axisymmetric black-hole collisions. *Phys. Rev. D*, 44:2983–3000, November 1991.

[28] Gregory B. Cook. Three-dimensional initial data for the collision of two black holes II: Quasicircular orbits for equal mass black holes. *Phys. Rev. D*, 50:5025–5032, October 1994.

[29] Gregory B. Cook. Initial data for numerical relativity. Article in online journal Living Reviews in Relativity, 2000. http://www.livingreviews.org/lrr-2000-5.

[30] Gregory B. Cook. Corotating and irrotational binary black holes in quasi-circular orbit. *Phys. Rev. D*, 65:084003, April 2002.

[31] Gregory B. Cook and Thomas W. Baumgarte. Excision boundary conditions for the conformal metric. *Phys. Rev. D*, 77:104016, 2008.

[32] Gregory B. Cook, Matthew W. Choptuik, Mark R. Dubal, Scott Klasky, Richard A. Matzner, and Samuel R. Oliveira. Three-dimensional initial data for the collision of two black holes. *Phys. Rev. D*, 47:1471–1490, February 1993.

[33] Gregory B. Cook and Harald P. Pfeiffer. Excision boundary conditions for black hole initial data. *Phys. Rev. D*, 70:104016, 2004.

[34] Thibault Damour, Eric Gourgoulhon, and Philippe Grandclément. Circular orbits of corotating binary black holes: Comparison between analytical and numerical results. *Phys. Rev. D*, 66:024007, July 2002.

[35] Thibault Damour, Piotr Jaranowski, and Gerhard Schaefer. Dynamical invariants for general relativistic two-body systems at the third post-Newtonian approximation. *Phys. Rev. D*, 62:044024, August 2000.

[36] Steven Detweiler. Periodic solutions of the einstein equations for binary systems. *Phys. Rev. D*, 50:4929–4943, October 1994.

[37] Bryce DeWitt. Quantum theory of gravity 1: The canonical theory. *Phys. Rev.*, 160:1113–1148, 1967.

[38] Olaf Dreyer, Badri Krishnan, Dierdre Shoemaker, and Erik Schnetter. Introduction to isolated horizons in numerical relativity. *Phys. Rev. D*, 67:024018, January 2003.

[39] Charles R. Evans. *A Method for Numerical Relativity: Simulation of Axisymmetric Gravitational Collapse and Gravitational Radiation Generation*. PhD thesis, University of Texas at Austin, 1984.

[40] John L. Friedman, Kōji Uryū, and Masaru Shibata. Thermodynamics of binary black holes and neutron stars. *Phys. Rev. D*, 65:064035, March 2002.

[41] Alcides Garat and Richard H. Price. Nonexistence of conformally flat slices of the Kerr spacetime. *Phys. Rev. D*, 61:124011, June 2000.

[42] Jose A. Gonzalez, Ulrich Sperhake, and Bernd Brügmann. Black-hole binary simulations: the mass ratio 10:1. 2008. gr-qc/0811.3952.

[43] Eric Gourgoulhon, Philippe Grandclément, and Silvano Bonazzola. Binary black holes in circular orbits. I. A global spacetime approach. *Phys. Rev. D*, 65:044020, February 2002.

[44] Philippe Grandclément, Eric Gourgoulhon, and Silvano Bonazzola. Binary black holes in circular orbits. II. Numerical methods and first results. *Phys. Rev. D*, 65:044021, February 2002.

[45] Jason D. Grigsby and Gregory B. Cook. Measuring eccentricity in binary black-hole initial data. *Phys. Rev. D*, 77:044011, 2008.

[46] Mark D. Hannam. Quasi-circular orbits for conformal thin-sandwich puncture binary black holes. *Phys. Rev. D*, 72:044025, August 2005.

[47] Mark D. Hannam and Gregory B. Cook. Conformal thin-sandwich puncture initial data for boosted black holes. *Phys. Rev. D*, 71:084023, April 2005.

[48] Steven W. Hawking and G. F. R. Ellis. *The Large Scale Structure of Spacetime*. Cambridge University Press, Cambridge, England, 1973.

[49] Lawrence E. Kidder. Coalescing binary systems of compact objects to (post)$^{(}5/2)$-newtonian order. V. spin effects. *Phys. Rev. D*, 52:821–847, July 1995.

[50] Anil D. Kulkarni. Time-asymmetric initial data for the N black hole problem in general relativity. *J. Math. Phys.*, 25:1028–1034, April 1984.

[51] Anil D. Kulkarni, Lawrence C. Shepley, and James W. York, Jr. Initial data for N black holes. *Phys. Lett.*, 96A:228–230, July 1983.

[52] A. Lichnerowicz. L'integration des équations de la gravitation relativiste et le problème des n corps. *J. Math. Pures et Appl.*, 23:37–63, 1944.

[53] Richard W. Lindquist. Initial-value problem on Einstein-Rosen manifolds. *J. Math. Phys.*, 4:938–950, July 1963.

[54] Pedro Marronetti, Wolfgang Tichy, Bernd Brugmann, Jose Gonzalez, and Ulrich Sperhake. High-spin binary black hole mergers. *Phys. Rev. D*, 77:064010, March 2008.

[55] Raoul-Martin Memmesheimer, Achamveedu Gopakumar, and Gerhard Schäfer. Third post-newtonian accurate generalized quasi-keplerian parametrization for compact binaries in eccentric orbits. *Phys. Rev. D*, 70:104011, November 2004.

[56] Charles W. Misner. The method of images in geometrostatics. *Ann. Phys.*, 24:102–117, October 1963.

[57] Charles W. Misner, Kip S. Thorne, and John Archibald Wheeler. *Gravitation.* W. H. Freeman and Company, New York, New York, 1973.

[58] Thierry Mora and Clifford M. Will. Numerically generated quasicircular orbits of black holes: Circular or eccentric? *Phys. Rev. D*, 66:101501(R), 2002.

[59] Thierry Mora and Clifford M. Will. Post-Newtonian diagnostic of quasiequilibrium binary configurations of compact objects. *Phys. Rev. D*, 69:104021, 2004.

[60] P. C. Peters. Gravitational radiation and the motion of two point masses. *Phys. Rev.*, 136:B1224, November 1964.

[61] Harald P. Pfeiffer, Gregory B. Cook, and Saul A. Teukolsky. Comparing initial-data sets for binary black holes. *Phys. Rev. D*, 66:024047, July 2002.

[62] Harald P. Pfeiffer, Lawrence E. Kidder, Mark A. Scheel, and Saul A. Teukolsky. A multidomain spectral method for solving elliptic equations. *Comput. Phys. Commun.*, 152:253–273, 2003.

[63] William H. Press, Saul A. Teukolsky, William T. Wetterling, and Brian P. Flannery. *Numerical Recipes in C*. Cambridge University Press, Cambridge, England, second edition, 1992.

[64] Frans Pretorius. Evolution of Binary Black-Hole Spacetimes. *Phys. Rev. Lett.*, 95:121101, 2005.

[65] R. Rieth. On the validity of Wilson's approach to general relativity. In Andrzej Królak, editor, *Mathematics of Gravitation. Part II. Gravitational Wave Detection*, pages 71–74. Polish Academy of Sciences, Institute of Mathematics, Warsaw, 1997. Proceedings of the Workshop on Mathematical Aspects of Theories of Gravitation held in Warsaw, February 29–March 30, 1996.

[66] Masaru Shibata, Kōji Uryū, and John L. Friedman. Deriving formulations for numerical computation of binary neutron stars in quasicircular orbits. *Phys. Rev. D*, 70:044044, 2004.

[67] Rafael Sorkin. A criterion for the onset of instabilities at a turning point. *Astrophys. J.*, 249:254–257, October 1981.

[68] Rafael D. Sorkin. A stability criterion for many-parameter equilibrium families. *Astrophys. J.*, 257:847–854, June 1982.

[69] László B. Szabados. Quasi-local energy-momentum and angular momentum in GR: A review article. *Living Rev. Relativity*, 7(4), 2004. http://www.livingreviews.org/lrr-2004-4.

[70] Kip S. Thorne and James B. Hartle. Laws of motion and precession for black holes and other bodies. *Phys. Rev. D*, 31:1815–1837, 1985.

[71] Kōji Uryū, Francois Limousin, John L. Friedman, Eric Gourgoulhon, and Masaru Shibata. Binary neutron stars: Equilibrium models beyond spatial conformal flatness. *Phys. Rev. Lett.*, 97:171101, October 2006.

[72] James W. York, Jr. Gravitational degrees of freedom and the initial-value problem. *Phys. Rev. Lett.*, 26:1656–1658, June 1971.

[73] James W. York, Jr. Role of conformal three-geometry in the dynamics of gravitation. *Phys. Rev. Lett.*, 28:1082–1085, April 1972.

[74] James W. York, Jr. Conformally invariant orthogonal decomposition of symmetric tensors on Riemannian manifolds and the initial-value problem of general relativity. *J. Math. Phys.*, 14:456–464, April 1973.

[75] James W. York, Jr. Covariant decompositions of symmetric tensors in the theory of gravitation. *Ann. Inst. Henri Poincaré, A*, 21:319–332, 1974.

[76] James W. York, Jr. Kinematics and dynamics of general relativity. In Larry L. Smarr, editor, *Sources of Gravitational Radiation*, pages 83–126. Cambridge University Press, Cambridge, England, 1979.

[77] James W. York, Jr. Conformal 'thin-sandwich' data for the initial-value problem of general relativity. *Phys. Rev. Lett.*, 82:1350–1353, February 1999.

[78] James W. York, Jr. and Tsvi Piran. The initial value problem and beyond. In Richard A. Matzner and Lawrence C. Shepley, editors, *Spacetime and Geometry*, pages 147–176. University of Texas, Austin, 1982.